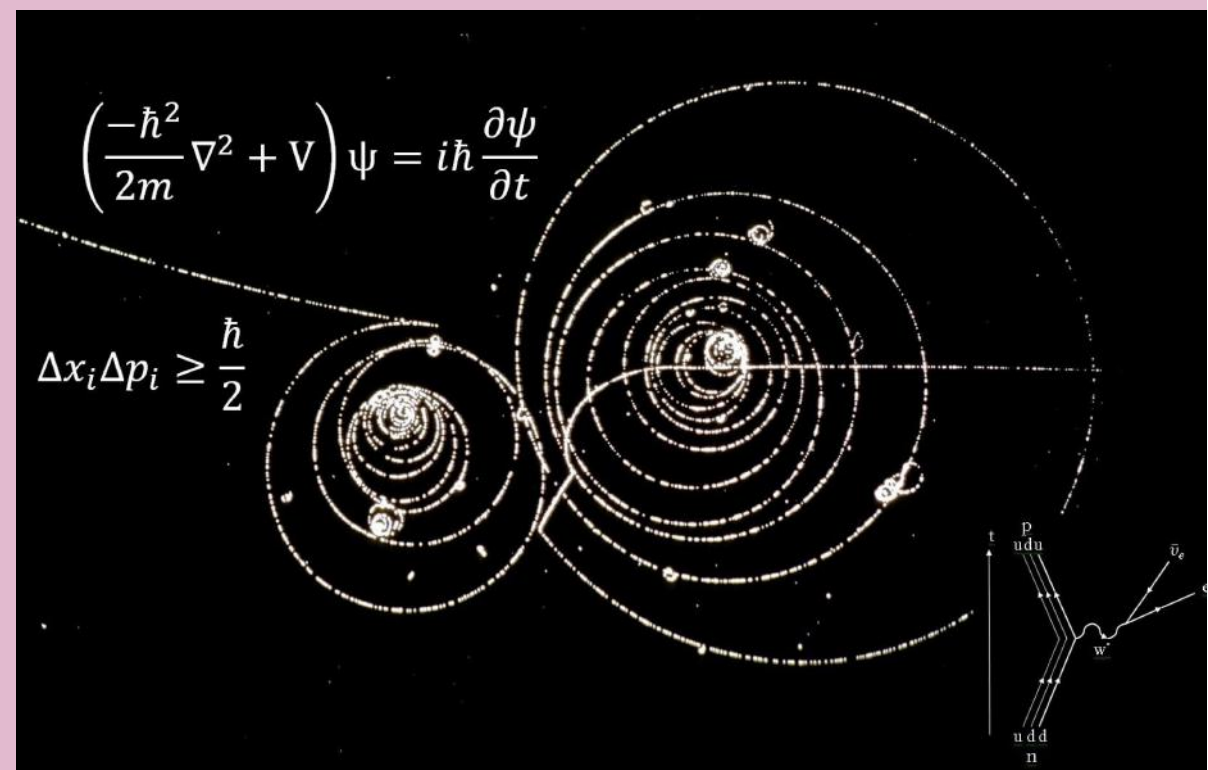


Academic Studies in SCIENCE and MATHEMATICS Sciences

Editors

Prof. Dr. Sema Isisag Ucuncu & Prof. Dr. Tanja V. Soldatovic

Academic Studies in SCIENCE and MATHEMATICS Sciences



ISBN: 978-2-38236-051-4



9 782382 360514



LIVRE DE LYON

- livredelyon.com
- livredelyon
- livredelyon
- livredelyon

Science



LIVRE DE LYON

Lyon 2020

Academic Studies in Science and Mathematics Sciences



Editors

Prof. Dr. Sema Isisag Ucuncu & Prof. Dr. Tanja V. Soldatović



LIVRE DE LYON

Lyon 2020

Editors • Prof. Dr. Sema Isisag Ucuncu  ORCID 0000-0002-2739-4009
Prof. Dr. Tanja V. Soldatović  ORCID 000-0003-3010-6503

Cover Design • Aruull Raja
First Published • December 2020, Lyon

ISBN: 978-2-38236-051-4

© copyright

All rights reserved. No part of this publication may be reproduced, stored in a retrieval system, or transmitted in any form or by any means, electronic, mechanical, photocopying, recording, or otherwise, without the publisher's permission.

The chapters in this book have been checked for plagiarism by  intihal.net

Publisher • Livre de Lyon

Address • 37 rue marietton, 69009, Lyon France

website • <http://www.livredelyon.com>

e-mail • livredelyon@gmail.com



PREFACE

In this technology and informatics era, answers of some questions that we are often facing need great transitions in theoretical and applied sciences. Do we really know the outcomes of pursuing pure sciences? How can pure and applied sciences be differentiated? And moreover, is this differentiation is a *sine qua non* condition?

Every scientist knows that there are no precise boundaries between disciplines.

From this point of start, the purpose of this seven chapters containing book is to confer some new approaches about science and mathematical sciences.

The editors thanks to the authors for their competent work in preparing this book for publication.

CONTENTS

PREFACE.....	I
REFEREES.....	V
Chapter I Serpil Yalçın Kuzu	
UNDERSTANDING OF EARLY UNIVERSE WITH THE MEASUREMENTS OF $K^*(892)^0$ AND $\phi(1020)$ RESONANCES.....	1
Chapter II Ç. E. Demirci Dönmez & A. Dönmez	
MAGNETIC HYPERTHERMIA FOR CANCER TREATMENT.....	13
Chapter III A. Türkhan	
PARTIAL PURIFICATION AND CHARACTERIZATION OF PEROXIDASE FROM ZEFERAN PEACH (<i>Prunuds persica L.</i>).....	33
Chapter IV S. İnan & B. Çetinkaya	
PREPARATION AND CHARACTERIZATION OF URANIUM OXIDE MICROSPHERES BY INTERNAL SOL-GEL PROCESS.....	45
Chapter V B. Yılmaz & G. Uysal	
ON KIROV-TYPE GENERALIZATION OF GAUSS- WEIERSTRASS OPERATORS.....	59
Chapter VI Esmâ Y. Özkan	
APPROXIMATION BY FUZZY BERNSTEIN TYPE RATIONAL FUNCTIONS.....	71
Chapter VII I. Unal	
CURVATURE TENSORS ON NORMAL METRIC CONTACT PAIR MANIFOLDS.....	87

REFEREES

Prof. Dr. Sema İşisag Ucuncu, Ege University, Turkey

Prof. Dr. Serap Seyhan Bozkurt, Dokuz Eylul University, Turkey

Prof. Dr. Tanja Soldatović, Novi Pazar State University, Serbia

Assoc. Prof. Dr. Yakup Kolcuoğlu, Karadeniz Technical University,
Turkey


Asst. Prof. Dr. Sunil K. Sharma, Cluster University of Jammu, Jammu,
India

CHAPTER I

UNDERSTANDING OF EARLY UNIVERSE WITH THE MEASUREMENTS OF $K^*(892)^0$ AND $\phi(1020)$ RESONANCES

Serpil Yalçın Kuzu¹

1(Dr.); Firat University, e-mail: skuzu@firat.edu.tr

 ORCID 0000-0001-8905-8089

INTRODUCTION

Bang! The universe was born. Within a few microseconds after the big bang, the whole universe was composed of quarks and gluons, the smallest known building blocks of matter. This new state of the medium is called quark-gluon plasma (QGP). As the medium expanded and cooled down quarks and gluons, also called partons, were started to form hadrons such as protons (p), pions (π) and kaons (K). In the end, the universe became what we observe today. In order to explore the universe and its physical properties, the first state of matter, the hot and dense quark gluon soup, must be created.

Relativistic hadron colliders are the only tools that provide to investigate the features of hadronic matter interacting via strong force in very high temperature and pressure under laboratory conditions. In these intense conditions, hadronic matter is expected to return to its initial state, so called as *partonic state*. There are two relativistic hadron colliders in the world, namely the Large Hadron Collider (LHC) [1, 2] at European Organization for Nuclear Research (CERN) in Europe and the Relativistic Heavy Ion Collider (RHIC) [3] at Brookhaven National Laboratory (BNL) in USA. At these colliders, various particles have been collided at different energies. In order to study QGP phase formed in high energy collisions, large detector systems are needed. For this purpose, A Large Ion Collider Experiment (ALICE) [4] at the LHC, Solenoidal Tracker (STAR) [5] and Pioneering High Energy Nuclear Interaction eXperiment (PHENIX) [6] at RHIC were designed specifically to understand the medium and its evolution in relativistic heavy ion collisions.

Dynamics of Heavy Ion Collisions:

In heavy ion collisions, two ions look as Lorentz contracted pancakes due to their speed in the direction of their motion shown in Figure 1 [7]. The number of nucleons participating the relativistic

collision depends on overlap region of the nuclei in the transverse plane. This region is defined by the *impact parameter* (b) which is the distance between the centers of two nuclei in transverse plane. The nucleons participating in the collision are named “participants” and the rest of them are named “spectators”.

Geometry and impact parameter of the collisions can be studied by defining *centrality* and *multiplicity classes*. Centrality is defined as percentiles of the nucleus-nucleus *cross section*, which is a probability that a given atomic nucleus will exhibit a specific reaction. Multiplicity is the number of participants in the collision that can be determined by using centrality classes. A collision having the smallest percentile of centrality is called the most central or head on collision. Compared to other centrality classes the number of participants in the most central collisions is the largest whereas the impact parameter is the smallest. A collision having the largest percentile of centrality and largest impact parameter is called peripheral collision.

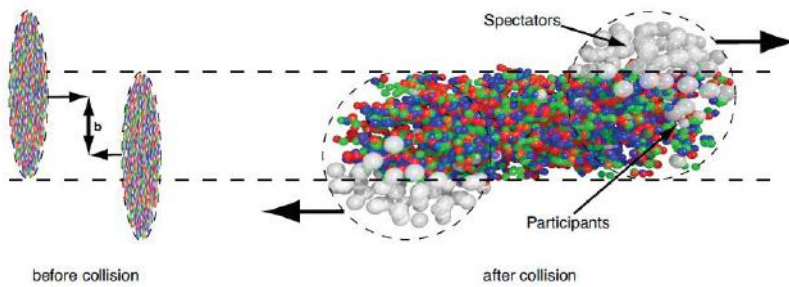


Figure 1: Picture of relativistic heavy ion collisions [7].

The evolution of heavy ion collisions is shown in Figure 2 [8]. When two nuclei collide at relativistic energies, initially nucleons in the overlap region interact and produce high momentum particles which are the significant tool to study the initial state of the collisions. The rest of the particles in the region are thermalized and form hot and dense fireball, QGP. The fireball expands and cools down until it reaches *chemical freeze-out temperature* (T_c), the stage at which the particle species are fixed and inelastic interactions between hadrons stops [9, 10, 11]. At this phase the medium becomes mixture of partons and hadrons and all the partons are confined to form hadron gas. The hadronic medium continues to expand and cool down until it reaches kinetic *freeze-out temperature* (T_k), the stage at which the elastic scattering between particles stops and particle yields are fixed [9, 10, 11]. After the T_k , particles leave the collision area and can be detected by detectors. Each stage of the medium can be explored by studying produced particles and their properties as experimental probes.

There are two types of experimental signs of QGP: soft probes and hard probes. Soft probes such as particle multiplicity, yield and transverse momentum spectra provide information about expansion and thermalization of the medium. Study of hard probes such as partonic energy loss mechanism in the collisions is used to figure out the initial state of the medium.

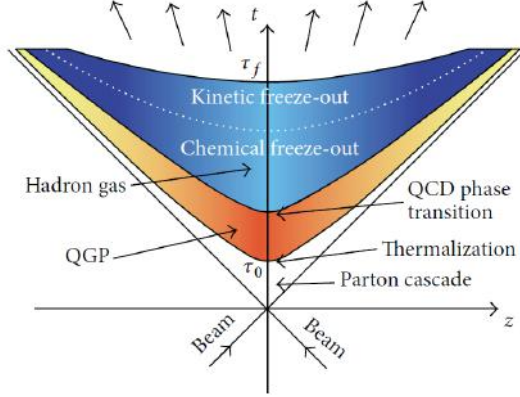


Figure 2: The space-time evolution of a heavy-ion collision. The ions collide when time (t) and space (z) equal to 0 [8].

RESONANCES

Resonances are excited states of the corresponding ground state particles having lifetime (τ) in order of a few fm/c ($\tau \sim 10^{-23}$ s) which is almost the lifetime of the medium formed in heavy ion collisions [9]. Different than other particles the medium may modify their properties such as mass, width and yield. Due to their short survival time resonances cannot be measured directly by the detectors. Therefore, they can be studied by reconstruction of their invariant mass spectrum from their identified decay products with the help of invariant mass formula given as Eq.1

$$m_{\text{inv}} = \sqrt{(E_1 + E_2)^2 + (\vec{p}_1 + \vec{p}_2)^2} \quad (1)$$

where m_{inv} represents invariant mass of the resonance, E_1 and E_2 are the energies and \vec{p}_1 and \vec{p}_2 represent momentum of the decay products respectively. In addition to their decay process, resonances may rescatter and regenerate between chemical freeze-out and kinetic freeze-out temperatures. In regeneration process, resonances are reproduced by pseudo-inelastic interactions between their decay products and hadrons in the medium which results in enhancement of the resonance yield [11, 12]. In rescattering process, elastic or pseudoelastic scattering occurs between their decay products and hadrons in the medium which may cause reduction in the resonance yield [11, 12].

Resonance studies play a significant role to investigate the features of the medium formed in relativistic collisions. Studying resonance properties such as particle ratios, yield and mean transverse momentum ($\langle p_T \rangle$) provides information about in medium effects on resonance productions. Because of their lifetime, they can be used to understand the dynamics of the hadronic phase. In addition, measurement of resonances having different lifetimes may help to explore the role of rescattering and regeneration processes in production mechanism of the resonances. Also comparison of resonances produced in different collision systems allows figuring out in medium effects. List of the resonances is given in Table 1 [13].

Table 1: List of resonances with their lifetimes, decay modes and branching ratios [13].

Resonances	Lifetime $c\tau(\text{fm})$	Decay Modes	Branching Ratio[%]
$\rho(770)^0$	1.3	$\pi^+\pi^-$	100
$K^*(892)^0$	4.2	$K^+\pi^-$	66.6
$\Sigma^*(1385)^+$	5.5	$\Lambda\pi^+ \rightarrow (p\pi^+)\pi^+$	87
$\Lambda^*(1520)$	12.6	$p+K^-$	22.5
$\Xi^*(1530)^0$	21.7	$\Xi^-\pi^+ \rightarrow (\Lambda\pi^+)\pi^+$	66.7
$\phi(1020)^0$	44	K^+K^-	48.9

$K^*(892)^0$ AND $\phi(1020)$ RESONANCES

$K^*(892)^0$ and $\phi(1020)$ resonances can be studied via their hadronic decays to charged pions and kaons: $K^*(892)^0 \rightarrow K^\pm + \pi^\mp$ and $\phi(1020) \rightarrow K^\pm + K^\mp$ [13]. In Table 1 it is given that lifetime of $\phi(1020)$ is approximately ten times longer than that of $K^*(892)^0$ [13]. Therefore measurement of $K^*(892)^0$ and $\phi(1020)$ resonance productions in various collision systems may help to explore medium and its effects on resonance production mechanism. For this reason their properties such as transverse momentum (p_T) spectra, p_T integrated yields (dN/dy) and particle ratios were studied in different collision systems and energies

Transverse Momentum (p_T) Spectra

The p_T spectra of $K^*(892)^0$ and $\phi(1020)$ were measured in various collision systems and energies. As an example in STAR experiment, the spectra of $K^*(892)^0$ and $\phi(1020)$ were studied in gold-gold (Au-Au)

collisions at a centre-of-mass energy ($\sqrt{s_{NN}}$) of 62.4 GeV and 200 GeV respectively for different centrality classes shown in Figure 3 [14, 15]. From the figure it is concluded that for both resonances the spectra shape evolve from low to high centrality classes.

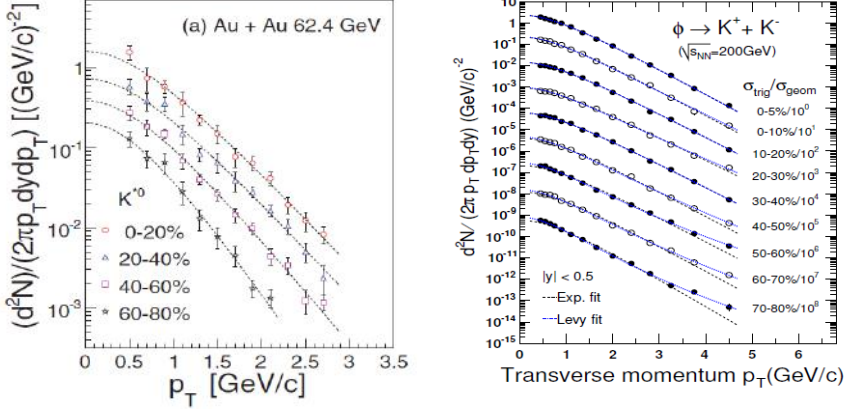


Figure 3: Spectra of $K^*(892)^0$ (left) and $\phi(1020)$ (right) in Au+Au collisions at 62.4 GeV and 200 GeV respectively for different centralities [14, 15]. The dashed lines represent the exponential fit. The errors shown in $K^*(892)^0$ spectra are quadratic sums of statistical and systematic uncertainties. In $\phi(1020)$ spectra the dotted lines are Levy function fits [15] and error bars show statistical errors only.

Spectra of the resonances were also studied in ALICE for various collision systems and energies. Figure 4 shows an example of the spectra study of $K^*(892)^0$ and $\phi(1020)$ in proton-proton (pp) collisions at $\sqrt{s} = 13$ TeV in ALICE [16]. In the figure for both resonances the shape of the spectra evolve from low to high multiplicity classes for p_T less than 5 GeV/c. For higher p_T values the spectra have the similar shape in different multiplicity classes which indicates that the processes that results change in the spectra shape in different multiplicity classes are dominant principally at low p_T [16, 17]. A similar trend was also observed for unidentified charged hadrons such as K_S^0 , Λ and Ξ for the same collision system [16, 17].

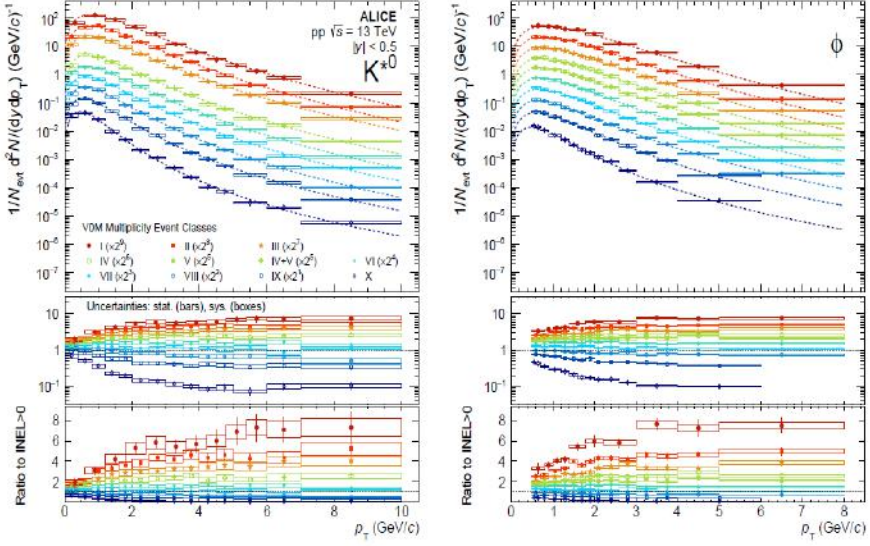


Figure 4: Spectra of $K^*(892)^0$ and $\phi(1020)$ in pp collisions at 13 TeV for different multiplicities, scaled by factors. The lower panels show the ratios of the multiplicity-dependent p_T spectra to the multiplicity-integrated INEL>0 spectra [16].

The p_T Integrated Yields (dN/dy)

Integrated yields (dN/dy) of $K^*(892)^0$ and $\phi(1020)$ for different multiplicity classes are extracted from the spectra explained in previous section and extrapolated for the p_T region where there is no measurement by fitting with a function in the measured p_T interval [18, 19, 20]. In ALICE, integrated yields of $K^*(892)^0$ and $\phi(1020)$ as a function of mean charged particle multiplicity at midrapidity ($\langle dN_{ch}/d\eta \rangle_{|y|<0.5}$) were studied in pp collisions at $\sqrt{s} = 7$ TeV and 13 TeV, and proton-lead (p-Pb) collisions at $\sqrt{s_{NN}} = 5.02$ TeV shown in Figure 5 [16]. It is concluded that dN/dy of the particles increase from low to high multiplicity classes. The experimental $K^*(892)^0$ and $\phi(1020)$ results of pp collisions at $\sqrt{s} = 13$ TeV are compared with different model calculations [16]. From the calculations EPOS-LHC and PYTHIA8 without CR (color reconnection) models defined $K^*(892)^0$ yields well however for $\phi(1020)$ yields EPOS-LHC model overestimated and PYTHIA models underestimated the results.

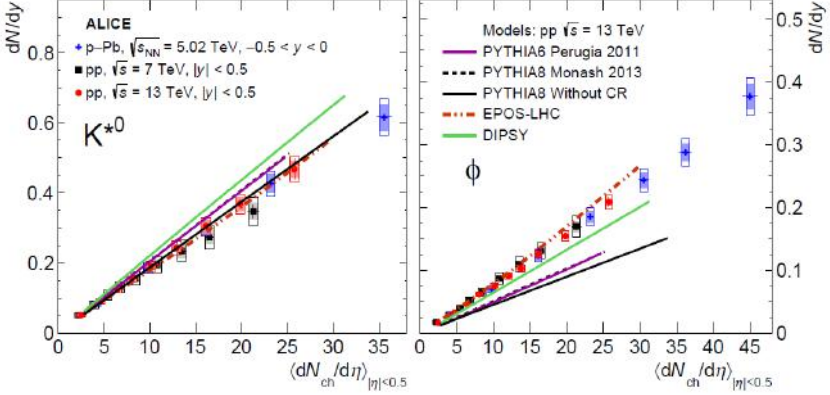


Figure 5: dN/dy of $K^*(892)^0$ (left) and $\phi(1020)$ (right) as a function of $\langle dN_{ch}/d\eta \rangle_{|\eta| < 0.5}$ for various collision systems. The measurements in pp collisions at 13 TeV are compared with results from event generators [21, 22, 23, 24]. Bars show statistical uncertainties, open boxes show total systematic uncertainties, and shaded boxes show the systematic uncertainties [16].

Particle Ratios

The p_T integrated particle yield ratios in different collision systems allows exploring system size effect on resonance production mechanism. In the experiments $K^*(892)^0$ to charged kaon (K) and $\phi(1020)$ to charged kaon (K) particle ratios were studied in different collision systems and energies. Figure 6 shows $K^*(892)^0/K$ and $\phi(1020)/K$ ratios as a function of $dN_{ch}/d\eta$ [25] and average number of participating nucleons, $\langle N_{part} \rangle$, for various collision systems measured in STAR respectively [25, 26]. $K^*(892)^0/K$ ratio decreases with increasing number of participants and decreases from pp, deuteron-gold (d-Au), to central Au-Au collisions. The decrease in the ratio is explained as the rescattering effect in $K^*(892)^0$ production. $\phi(1020)/K$ ratio has flat trend with increasing N_{part} . Ratios of $K^*(892)^0/K$ and $\phi(1020)/K$ were also studied in ALICE for pp collisions at $\sqrt{s} = 7$ TeV [27], p-Pb collisions at $\sqrt{s_{NN}} = 5.02$ TeV [28] and Pb-Pb collisions at $\sqrt{s_{NN}} = 2.76$ TeV [29] as a function of cubic root of charged particle multiplicity density ($\langle dN_{ch}/d\eta \rangle^{1/3}$) that is used as a proxy for the system size at midrapidity [28]. Suppression in $K^*(892)^0/K$ ratio is an evidence of the rescattering effects in high-multiplicity events which indicates a finite lifetime of the hadronic phase in p-Pb and Pb-Pb collisions. The explanation of no suppression in $\phi(1020)/K$ ratio for central collisions is the result of the long lifetime of $\phi(1020)$ resonance.

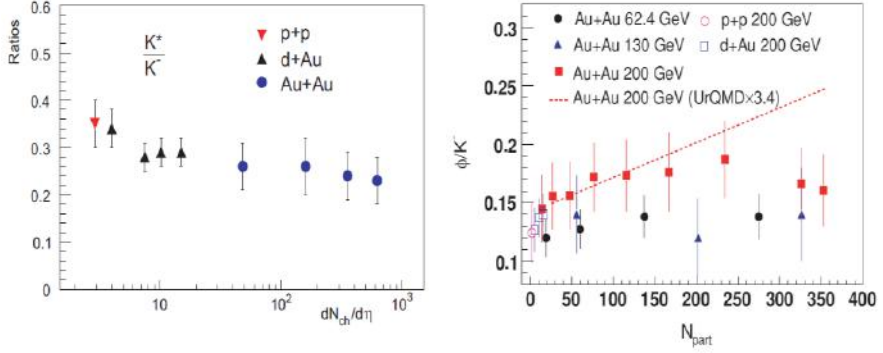


Figure 6: $K^*(892)^0/K$ (left) and $\phi(1020)/K$ (right) ratios in pp and various centralities in d-Au and Au-Au collisions at $\sqrt{s_{NN}} = 200\text{GeV}$ as a function of $dN_{ch}/d\eta$ [25] and N_{part} [26], respectively.

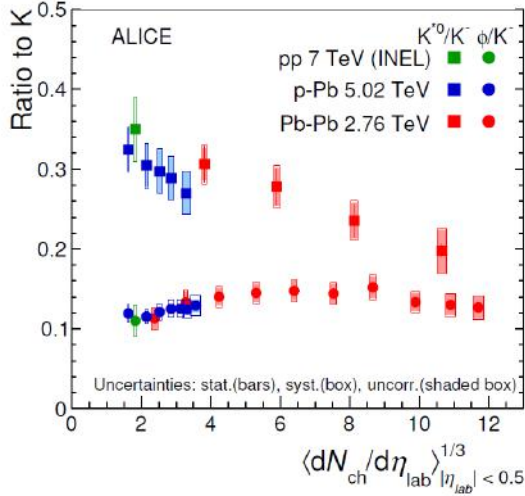


Figure 7: $K^*(892)^0/K$ and $\phi(1020)/K$ ratios in three different collision systems as a function of $\langle dN_{ch}/d\eta \rangle^{1/3}$ measured at midrapidity. Bars show statistical uncertainties with total and multiplicity-uncorrelated systematic uncertainties. Measurements in pp at $\sqrt{s} = 7\text{ TeV}$ and Pb-Pb collisions at $\sqrt{s_{NN}} = 2.76\text{ TeV}$ are taken from [27] and [29], respectively.

CONCLUSIONS

Because of their short lifetime, resonances can be used to probe evolution of the medium created in relativistic heavy ion collisions to explore the early stages of the universe. For this purpose transverse momentum spectra, integrated yield and particle ratios of $K^*(892)^0$ and $\phi(1020)$ resonances have been studied in high energy particle physics experiments to investigate the medium evolution especially between

chemical and kinetic freezeout temperatures and rescattering and regeneration effects in hadronization. Spectra studies of these particles in collisions at high energies on the order of GeV and TeV showed that the spectra get harder for both resonances with increasing multiplicity and centrality. Integrated yields (dN/dy) of $K^*(892)^0$ and $\phi(1020)$ extracted from p_T spectra demonstrated that for both resonances the yield increases towards higher multiplicity classes independent from colliding system and energy. Lastly, the p_T integrated particle yield ratios of $K^*(892)^0$ and $\phi(1020)$ to charged kaons (K) were studied to understand hadronic phase and regeneration and rescattering effects on resonance production mechanism. In central and high multiplicity classes suppression in $K^*(892)^0/K$ is observed in various collision systems and energies since in $K^*(892)^0$ production rescattering is dominant over regeneration. Interestingly no suppression is observed in $\phi(1020)/K$ due to long lifetime of $\phi(1020)$. Resonance results indicate the presence of hadronic phase that causes decrease in yield of short lived resonances.

ACKNOWLEDGMENTS

This work is supported by TAEK under contract of 2019TAEK(CERN)A5.H1.F5-23.

REFERENCES

- [1] LHC Study Group (1995). *The Large Hadron Collider Conceptual Design Report*, CERN/AC 95-05.
- [2] Bryant P., & Evans L. (2008). LHC Machine. *Journal of Instrumentation*, 3, S08001. doi: 10.1088/1748-0221/3/08/S08001.
- [3] Harrison M., Ludlam T., & Ozaki S. (2003). RHIC project overview. *Nuclear Instruments and Methods in Physics Research*, A499, 235–244.
- [4] ALICE Collaboration (2014). Performance of the ALICE Experiment at the CERN LHC. *International Journal of Modern Physics*, A29, 1430044. doi:10.1142/S0217751X14300440
- [5] STAR Collaboration (2003). STAR detector overview. *Nuclear Instruments and Methods in Physics Research*, A499, 624–632. doi: 10.1016/S0168-9002(02)01960-5
- [6] PHENIX Collaboration (2003). PHENIX detector overview. *Nuclear Instruments and Methods in Physics Research*, A499, 469–479.
- [7] Snellings R. (2014). Collective expansion at the LHC: selected ALICE anisotropic flow measurements. *Journal of Physics G: Nuclear and Particle Physics*, 41, 124007.
- [8] Tawfik A., & Shalaby A. G. (2015). Balance Function in High-Energy Collisions. *Advances in High Energy Physics*, 186812.
- [9] Markert C. (2005). *What do we learn from Resonance Production in Heavy Ion Collisions?* Paper presented at the Proceedings of the 20th Winter Workshop on Nuclear Dynamics, Trelawny Beach, Jamaica.
- [10] Torrieri, G., & Rafelski, J. (2001). Strange Hadron Resonances as a Signature of Freeze-Out Dynamics. *Physics Letters*, B509, 239–245.
- [11] Aichelin J., & Bleicher M. (2002). Strange resonance production: probing chemical and thermal freeze-out in relativistic heavy ion collisions. *Physics Letter*, B530, 81-87. doi:10.1016/S0370-2693(02)01334-5
- [12] STAR Collaboration (2008). Hadronic resonance production in d+Au collisions at $\sqrt{s_{NN}} = 200$ GeV at RHIC. *Physics Review*, C78 044906. doi:10.1103/PhysRevC.78.044906
- [13] Particle Data Group Collaboration (2018). Review of particle physics. *Physics. Review*, D98, 030001.

- [14] STAR Collaboration (2011). K^{*0} production in Cu+Cu and Au+Au collisions at $\sqrt{s_{NN}} = 62.4$ GeV and 200 GeV. *Physics Review*, C84, 034909.
- [15] STAR Collaboration (2007). Partonic flow and ϕ meson production in Au+Au collisions at $\sqrt{s_{NN}}=200$ GeV. *Physical Review Letters*, 99 112301.
- [16] ALICE Collaboration (2020). Multiplicity dependence of $K^*(892)^0$ and $\phi(1020)$ production in pp collisions at $\sqrt{s} = 13$ TeV. *Physics Letters*, B807, 135501. doi: 10.1088/1742-6596/1602/1/012008
- [17] ALICE Collaboration (2020). Multiplicity dependence of (multi-) strange hadron production in proton-proton collisions at $\sqrt{s} = 13$ TeV. *European Physical Journal*, C80, 167. doi: 10.1140/epjc/s10052-020-7673-8
- [18] Tsallis C. (1988). Possible generalization of Boltzmann-Gibbs statistics. *Journal of Statistical Physics*, 52(1), 479.
- [19] Wilk G., & Włodarczyk Z. (2000). Interpretation of the nonextensivity parameter q in some applications of Tsallis statistics and Lévy distributions. *Physical Review Letters*, 84, 2770.
- [20] STAR Collaboration (2005). $K(892)^*$ Resonance Production in Au+Au and p+p Collisions at $\sqrt{s_{NN}} = 200$ GeV at RHIC. *Physics Review*, C71, 064902. doi: 10.1103/PhysRevC.71.064902
- [21] Flensburg C., Gustafson G., & Lönnblad L. (2011). Inclusive and exclusive observables from dipoles in high energy collisions. *Journal of High Energy Physics*, 8, 103. doi: 10.1007/JHEP08(2011)103
- [22] Pierog T., Karpenko L., Katzy J. M., Yatsenko E., & Werner K. (2016). EPOS LHC: test of collective hadronization with LHC data. *Physics Review*, C92, 034906.
- [23] Skands P. Z. (2010). Tuning Monte Carlo generators: the Perugia tunes. *Physics Review*, D82, 074018. doi: 10.1103/PhysRevD.82.074018
- [24] Skands P. Z., Carrazza S., & Rojo J. (2014). Tuning PYTHIA 8.1: the Monash 2013 tune. *European Physical Journal*, C74, 3024. doi:10.1140/epjc/s10052-014-3024-y
- [25] STAR Collaboration (2008). Hadronic resonance production in d+Au collisions at $\sqrt{s_{NN}}=200$ GeV measured at the BNL Relativistic Heavy Ion Collider. *Physics Review*, C78, 044906. doi:10.1103/PhysRevC.78.044906


- [26] STAR Collaboration (2009). Measurements of ϕ meson production in relativistic heavy-ion collisions at the BNL Relativistic Heavy Ion Collider (RHIC). *Physics Review*, C79, 064903.
- [27] ALICE Collaboration (2012). Production of $K^*(892)^0$ and $\phi(1020)$ in pp collisions at $\sqrt{s} = 7$ TeV. *European Physical Journal*, C72, 2183.
- [28] ALICE Collaboration (2016). Production of $K^*(892)^0$ and $\phi(1020)$ in p-Pb collisions at $\sqrt{s_{NN}} = 5.02$ TeV. *European Physical Journal*, C76, 245.
- [29] ALICE Collaboration (2015). $K^*(892)^0$ and $\phi(1020)$ production in Pb-Pb collisions at $\sqrt{s_{NN}} = 2.76$ TeV, *Physics Review*, C91, 024609.

CHAPTER II

MAGNETIC HYPERTHERMIA FOR CANCER TREATMENT

Çiğdem Elif Demirci Dönmez¹ & Adem Dönmez²

¹(Dr.), Muğla Sıtkı Koçman University, e-mail: elifdemirci@mu.edu.tr

 ORCID 0000-0002-3081-0691

²(Assoc. Prof. Dr.), Muğla Sıtkı Koçman University, e-mail: adonmez@mu.edu.tr

 ORCID 0000-0002-9773-0493

1. INTRODUCTION

Cancer is one of the biggest disease in the worldwide. Despite intensive research efforts have been spent to improve new methods and techniques for diagnosis and treatment of cancer in recent years, this disease still remains one of the leading causes of death globally (Chaturvedi, Singh, Singh, & Singh, 2018; Cryer & Thorley, 2019; Grodzinski, Kircher, Goldberg, & Gabizon, 2019; Hartshorn et al., 2018; Kargozar & Mozafari, 2018; Yezdani, Khan, Kushwah, Verma, & Khan, 2018; Zottel, Videtič Paska, & Jovčevska, 2019)

There are many types of therapeutic procedures which are conventional such as surgery, chemotherapy, radiation therapy, hormone therapy, gene therapy and immunotherapy provide significant improvements in cancer treatments. Though these therapeutic procedures possess several advantages, most of them suffer from several clinic issues that may cause adverse side effects on healthy cells close to the target cancerous area.

Hyperthermia (also called thermotherapy) is a promising alternative cancer treatment to current conventional therapies. This effective treatment modality is defined as increasing normal body temperature (~ 37.5-38.3 °C) to higher temperatures (~ 42-45 °C) over a period of time by using a heat source (Anghileri & Robert, 2019; Guardia, Riedinger, Kakwere, Gazeau, & Pellegrino, 2014). The heat induced by heat source can harm or kill cancer cells with minimal damage to healthy ones.

The term hyperthermia comes from the combination of two Greek words *hyper*, means “raise”, and *therme*, means “heat”. The use of heat in treatment of various diseases was common in various cultures for centuries. In very ancient times, humans used natural sources such as sand, hot water and steam naturally occurring in the volcanic caves for the

purpose of local heating. The clinical use of hyperthermia was observed in Ayurveda (a traditional system of Indian medicine) around 3000 years ago. Hippocrates (540-480 BC) demonstrated that the disease was treated with heat using hot sand in summer. Hyperthermia for cancer treatment was first used by a Roman doctor named Aulus Cornelius Celsus (25 BC-50 AD), who observed that cancer tumors on early stage are extremely sensible to heat. However, the use of hyperthermia in the literature only goes back to last century. The first paper on hyperthermia was published by a German surgeon named Carl D. W. Busch (1826 – 1881) in 1866. This study was the fundamental research in hyperthermia showing that cancerous cells can be selectively killed using high temperature while not harm healthy cells (Busch, 1866). After this study, interest in research on hyperthermia was dramatically increased. Though, several work were done in late 1800s in this area, clinical hyperthermia were developed in 1980s. Today, research on hyperthermia continues very rapidly, intensely and enthusiastically.

Hyperthermia treatments can be classified into three main categories, depending on the treated area: local, regional and whole-body hyperthermia. Local hyperthermia is used to heat smaller area from organs like a tumor. Microwaves, radio waves, ultrasound waves are the form of energy is used to heat the tumor region from the outside of the body in local hyperthermia. Thin heating needles or probes, radiofrequency electrodes or implantable microwave antennas are also used for heating in local hyperthermia. In the regional hyperthermia, the heat is applied to treat a part of the body, such as an organ, limb or body cavity. Heat is produced by using external devices that are placed over the region to be heated. In one other of regional hyperthermia approach, which is called regional perfusion, the blood is removed and pumped into a heating device and then pumped back into the area (sometimes with chemotherapy drugs) for heating. In the whole-body hyperthermia the overall body temperature is raised by using heating blankets, thermal rooms and chambers, warm-water (or wax) immersion or inductive coils.

Hyperthermia can be applied alone or in combination with conventional therapies. Though both hyperthermia treatment alone and combined have various advantages, there are still many drawbacks to overcome:

- a) Difficulty in temperature control that might leads to undesirable side effects such as bleeding, infection, blistering, swelling, pain and burns,
- b) Difficulty in temperature measurement at cell level,
- c) Uncontrollable temperature release on healthy cells,
- d) Non-uniform heat dissipation through the targeted region,

- e) Lack of non-invasive control for deep cancer regions in the local hyperthermia approach,
- f) The small penetration depth which is generally not exceeded a few centimeters,
- g) Toxicity of therapeutic drugs.
- h) Limited aqueous solubility of chemotherapeutic drugs leads to toxicity.

Actually, these undesirable issues are the major obstacle to clinical cancer treatments. To overcome this obstacle, researchers have been pushed to develop a new method, which has non-invasiveness and reduced- or non-toxicity, is more efficient compared with current modalities. The use of magnetic nanoparticles in hyperthermia as heat agents seems to help eliminating the disadvantages mentioned above, known as magnetic hyperthermia.

In the next section, we focus on magnetic hyperthermia and types of nanoparticles used in magnetic hyperthermia. The physical principles of magnetic hyperthermia will be discussed in detail further on. Also, in-vitro and in-vivo studies in hyperthermia and future perspectives will be addressed.

2. MAGNETIC HYPERTHERMIA

Magnetic hyperthermia is based on the use of magnetic materials to convert magnetic energy into heat energy in an alternative magnetic field (Fig. 1).

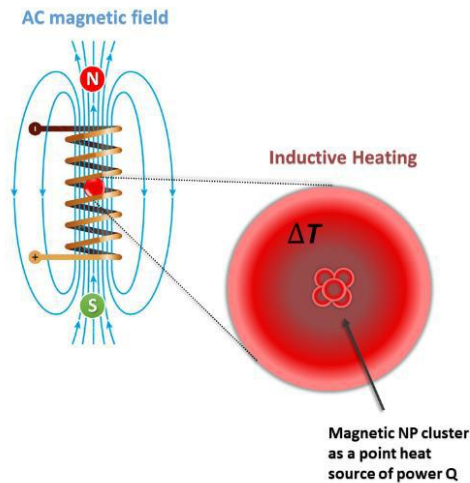


Fig. 1. The representation of magnetic hyperthermia.

The first magnetic hyperthermia experiment was performed by Gilchrist et al (1957). In this experiment, a therapeutic temperature (desired temperature to destroy cancer cells) range in 43-46 °C was successfully achieved using 20-100 nm sized maghemite ($\gamma\text{-Fe}_2\text{O}_3$) nanoparticles (under 1.2 MHz alternating magnetic field) to destroy metastases in lymphatic nodes.

When nanoparticles are subjected to alternating magnetic field, several heating mechanisms cause inductive heat as seen in Fig 1. These heating mechanisms will be discussed further. In biological environment, inductive heat is immediately transmitted to the surrounding cancer tissue to destroy it.

There are several advantages of magnetic hyperthermia:

- a) Less complications and side effects compared to conventional modalities,
- b) The possibility of multifaceted approach to treatment using magnetic nanoparticles as a drug delivery vehicle and also as induced heater for magnetic hyperthermia under external magnetic field,
- c) The accessibility to deeper tissues with higher penetration depth than conventional activation mechanisms (ultrasound and radiowaves),
- d) Efficient heating capabilities of magnetic hyperthermia by precise control of size and morphology of magnetic nanoparticles,
- e) Non-invasively releasing mechanisms of magnetic nanoparticles as a form of colloidal suspensions by drug release pathways.

The advantages of the magnetic hyperthermia lead to a shift in research towards the development of new type of nanomaterials to be used in magnetic hyperthermia therapy.

3. TYPES OF NANOPARTICLES USED IN MAGNETIC HYPERTHERMIA

Over the past decades, various types of magnetic nanoparticles have been studied for efficient magnetic hyperthermia. Magnetic nanoparticles used in magnetic hyperthermia can be generally categorized as: metals, metal oxides and alloys. Each type of materials has its own advantages as well as disadvantages, limitations and restrictions for clinical uses. In addition, multifunctional hybrid nanomaterials have been extensively investigated by researchers in recent years. These hybrid materials with enhanced features seems to be next generation systems for efficient magnetic hyperthermia.

3.1. MAGNETIC METAL AND MAGNETIC METAL OXIDE NANOPARTICLES

Magnetic metal nanoparticles and their oxides are the most commonly used magnetic materials in biomedical applications due to their relatively simple synthesis technique, stability in many colloidal media and their tunable magnetic properties. Iron (Fe), cobalt (Co), manganese (Mn) and Nickel (Ni) are some examples of magnetic metals. Iron oxides, such as magnetite (Fe_3O_4) and maghemite ($\gamma\text{-Fe}_2\text{O}_4$) and ferrites such as Co-, Mn- and NiFe_2O_4 are some examples of magnetic metal oxides. They have some positive and negative features compared to each other. For instance, Fe metal have higher magnetization compare to iron oxide of Fe_3O_4 and $\gamma\text{-Fe}_2\text{O}_4$ (Kafrouni & Savadogo, 2016). Higher magnetization is a desirable property for efficient magnetic hyperthermia in a safe frequency range ($f < 1.2$ MHz) (Hadjipanayis et al., 2008). Furthermore, iron and its oxides have lower toxicity compared to Co and Ni based nanoparticles (Kafrouni & Savadogo, 2016). Pradhan et al. (2007) showed that CoFe_2O_4 nanoparticles are more cytotoxic (with higher loss of cell viability of $>10\%$ at higher doses of >0.2 mg/mL) compared to Fe_3O_4 nanoparticles.

Besides the advantages of metals, high susceptibility to oxidation of metals limits their use in biomedical applications. At this point, the ferrites (with the general structural formula of MFe_2O_4 , where M is the metal ion) with high oxidative stability appear to be as an alternative to metallic magnetic nanoparticles. However, the CoFe_2O_4 nanoparticles can be chosen over the Fe_3O_4 nanoparticles in hyperthermia applications, because it has higher magnetocrystalline anisotropy ($23\text{-}40$ kJ/m³ for Fe_3O_4 and $180\text{-}200$ kJ/m³ for CoFe_2O_4 at room temperature) (Nguyen, 2016). Higher magnetocrystalline anisotropy may causes larger thermal energy dissipation. Though, it is observed that iron and iron oxide nanoparticles seem the most suitable for magnetic hyperthermia due to their known effects to metabolism and their lack of toxicity, many efforts is paid to other metallic magnetic nanoparticles (e.g. Co and Mn) due to increased heating efficiency with very small concentration. In the case that a good biocompatibility can be achieved, these metallic nanoparticles could be used safely in magnetic hyperthermia.

3.2. MAGNETIC ALLOY NANOPARTICLES

Magnetic alloy nanoparticles seem to be a good another alternative material for efficient magnetic hyperthermia. Palladium/Cobalt (Pd/Co), Iron/Cobalt (Fe/Co) and Iron/Nickel/Cobalt (Fe/Ni/Co) are some examples of magnetic alloys (Çelik & Fırat, 2018; Deger et al., 2002; Salati, Ramazani, & Almasi Kashi, 2020). They have interesting features make them possible candidates for the research in magnetic hyperthermia. For example, low Curie temperature of magnetic alloys make them very

suitable for self-regulated magnetic hyperthermia. Self-regulation means controllable heating at the tumor site. Heat control is achieved by controlling the Curie temperature of the magnetic nanoparticles which have Curie temperature in the range of 40-45 °C. The Curie temperature of any magnetic materials can be tuned by reasonable changing of particle size and composition. Self-regulation process leads to avoid undesirable sudden temperature change during magnetic hyperthermia experiments. In self-regulated hyperthermia, the magnetization of magnetic nanoparticles drops to zero and heating suddenly stops once Curie temperature is reached.

The earliest study of self-regulated hyperthermia using Nickel/Copper (Ni/Cu) alloy seeds have Curie temperature of 46-47 °C was made by Brezovich et al (1984). Recently, Barbosa et al (2019) have studied Ni/Cu alloys nanoparticles for enhanced heating in magnetic hyperthermia. Kawahara et al (2019) have studied the magnetic hyperthermia properties of self-controlled heating elements consisting of Fe/Al milling alloys. These investigations are important for a better understanding of the heating and self-regulated ability of magnetic alloy nanoparticles suitable for magnetic hyperthermia.

3.3. NEW MULTIFUNCTIONAL HYBRID MAGNETIC NANOPARTICLES

In recent years, multifunctional magnetic nanoparticles have raised great interest for development of novel therapeutics and diagnostic methods for routine clinical application in cancer treatments. These nanoparticles have some unique advantageous, such as feasibility to non-invasive delivery, biocompatibility, bioactivity, binding ability to cells, smart targeting, improved bloodstream circulation time, controlled drug delivery and release ability. The multifunctional hybrid nanostructures are made by combining magnetic nanoparticles with materials like natural and synthetic polymers (e.g. polysaccharides, proteins, polypropylene and polyethylene glycol) and porous materials (e.g. zeolite, mesoporous silica nanoparticles, metal organic frameworks).

3.3.1. POLYMERS

Polymers are extensively used materials in biomedical applications (Gaballah et al., 2019; Green & Elisseeff, 2016; Seppälä, Van Bochove, & Lendlein, 2020). They can be relatively designed and prepared easily in versatile architecture with appropriate functionality and physical, chemical and biological properties. There are several types of polymers, including hydrophilic and amphiphilic polymers, biodegradable and biocompatible polymers, stimuli responsive (e.g. pH and thermal responsive) polymers. A special class of polymers, functional polymers, which one or more reactive functional groups on the backbone or end of polymer chain, are

very appropriate to design multifunctional hybrid structures. For instance, Ding et al (2017) reported that magnetite-silver ($\text{Fe}_3\text{O}_4\text{-Ag}$) hybrid nanoparticles synthesized by a simple *in situ* reduction strategy. The obtained results in this study clearly indicates the enhancing effect of polymer coating on hyperthermia efficiency. In a very recent study, the efficiency of the niclosamide-loaded hyperbranched polymer-functionalized magnetic nanoparticles on mediated hyperthermia and niclosamide (an anticancer drug) bimodel therapy were investigated (Ahmad et al., 2020). The results in this study indicated that polymer-functionalized nanoparticles showed sufficient temperature gain for magnetic hyperthermia.

3.3.2. POROUS MATERIALS

Porous materials have received much attention in biomedical applications due to their ability to interact with biological ions and molecules both on their surface and entire volume. Various types of porous materials, such as zeolite, mesoporous silica nanoparticles, metal organic frameworks are used in different parts of body in accordance with the intended use.

For example, zeolites are very suitable to use in theranostic applications due to their high porous structure and tunable properties. In a very recent study, Vilaça et al (2019) developed a nanocomposite including zeolite as a suitable structure for the construct of a theranostic system. In this study, zeolite is used for drug encapsulation. The obtained results confirmed the successful formation of combined magnetic assemblies (magnetite nanoparticles) and microporous structure (zeolite) which are biocompatible and non-toxic. This study constitutes a step forward towards design multifunctional zeolite structures for theranostic applications in biomedicine.

Amongst the porous materials, the mesoporous silica nanoparticles are one of the most attractive materials due to their physicochemical features such as chemical, mechanical and thermal stability, high surface area, biocompatibility and uniform pore size. Moorthy et al (2018) reported that Fe_3O_4 modified mesoporous silica hybrid materials showed high drug capacity and pH-responsive drug release performance as well as high magnetic heating capacity with ability to reach the therapeutic temperature ($45\text{ }^\circ\text{C}$).

Another type of porous materials is metal organic frameworks (MOFs). In contrast to other porous materials, synthetic versatility and rich host-guest chemistry makes MOFs very suitable structures to design of advanced functional materials (Denny, Kalaj, Bentz, & Cohen, 2018; Desai, Sharma, Let, & Ghosh, 2019; D. Sun, Jang, Yim, Ye, & Kim, 2018). MOFs are very attractive materials for biomedical applications due to their

high porosity (can be used to load drugs) and controllable surface functionalities (can be used to bind targeting and binding ligands and agents). Since MOFs have higher drug loading capacity (related to high porosity structure) compared to ligand and polymer modified magnetic nanoparticles, they appear to be a better choice for synergetic hyperthermia with drug loading to improve hyperthermia efficiency.

Recently, Chen et al (2019) showed that efficient chemotherapy (due to pH-triggered drug release) and induced magnetic hyperthermia under alternating magnetic field (due to the magnetocaloric effect of Fe_3O_4 nanoparticles) achieved successfully by using $\text{Fe}_3\text{O}_4@\text{PDA}@\text{ZIF-90}$ (PDA: polydopamine and ZIF: zeolitic imidazolate frameworks which is a biocompatible MOF with acid-degradation) nanoparticles. There have been several promising studies published recently on hybrid materials with MOFs as novel systems to be used in biomedical applications (Beg et al., 2017; Keskin & Kizilel, 2011; Y. Sun et al., 2020).

4. PHYSICAL PRINCIPLES OF MAGNETIC HYPERTHERMIA

When magnetic materials are exposed to alternative magnetic field, they generate heat by the conversion of magnetic energy into thermal energy. The heat is induced via three potential mechanisms:

- a) Eddy current,
- b) Hysteresis losses,
- c) Néel and Brownian relaxations.

The heat dissipations from such of these mechanisms mainly depend on intrinsic characteristics of nanoparticles and some other external parameters. Particle size and shape, composition and magnetic anisotropy are some examples of intrinsic parameters. On the other hand, the external parameters include frequency, amplitude and homogeneity of alternating magnetic field and the viscosity and thermal conductivity of medium (e.g. glycerol, agar solution and tissue). The representation of Hysteresis loss and Néel and Brownian relaxations are schematically shown in Fig. 2.

4.1. EDDY CURRENTS

The first contribution of heating mechanism is defined by the contribution of eddy currents, which are generated as a consequence of the Faraday-Lenz law of electromagnetic induction. Eddy currents are a cause of energy loss that generate the heat energy (Joule heating), depending on the electrical resistivity and permeability of the material used and frequency of the applied field. In general, eddy currents occur not only in bulk magnetic materials but also in tissues. However, the tissues which have very low electrical conductivity ($0.6 \text{ } (\Omega\text{m})^{-1}$) produce a negligible

heating which is under practical therapeutic dose (Ortega & Pankhurst, 2012). Similar to tissues, since nano size materials have a very poor electrical conductivity the heat contribution from eddy currents considered to be negligible in magnetic hyperthermia. Therefore, the magnetic induction heating of magnetic materials is dominantly originated from hysteresis and relaxation losses.

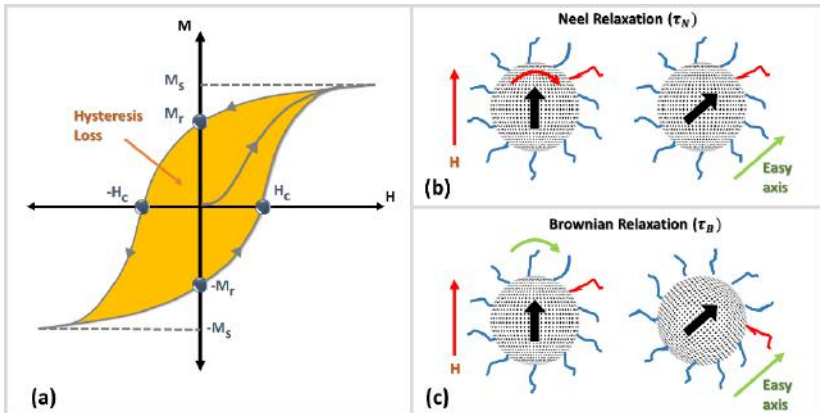


Fig. 2. The representation (a) hysteresis loss, (b) Néel relaxation, and (c) Brownian relaxation.

4.2. HYSTERESIS LOSSES

The second contribution of heating mechanism comes from hysteresis losses in a magnetic material. Hysteresis losses are directly proportional to enclosed area under the hysteresis loop mainly defined by saturation magnetization (M_s), magnetic coercivity (H_c) and remanence magnetization (M_r) as seen in Fig. 2a. Hysteresis losses occur in both large single and multi-domain magnetic nanoparticles which their size are on the order of 100 nm or larger (Deatsch & Evans, 2014). The energy loss per cycle for systems with larger particles is reduced due to the reduction in H_c with a corresponding reduction in M_r . Contrary, for smaller particles the energy loss is increased due to the enhancement of the anisotropy energy barriers which separate the different orientation states of particles.

4.3. NEEL AND BROWNIAN RELAXATIONS

The third contribution to heat heating mechanism comes from relaxations called Néel and Brownian relaxation. While Néel relaxation refers to the heating due to magnetic nanoparticle's dynamical fluctuations, the Brownian relaxation is related to physical rotation of the whole particles within the medium as seen in Fig. 2b-c (Fortin et al., 2007; Kumar & Mohammad, 2011).

The magnetism of any material is determined by the combination of finite size and surface effects when the size of material is reduced from

bulk to nano scale (~100 nm). At a very small size (i.e. a few tens of nanometers) a magnetic nanoparticle behaves like a giant paramagnetic atom with a fast response to the external magnetic field. This means that thermal energy causes the random flipping of the magnetization alignment away from its equilibrium state related to the energy barrier. The random flip of particle magnetic moment leads to zero net magnetization in the absence of an external magnetic field due to smaller anisotropy energy compared to thermal energy. This thermally activated magnetism which appears only in small ferromagnetic or ferrimagnetic nanoparticles is called superparamagnetism. Although coercivity and remanence disappear in superparamagnetic state, significant losses can still be observed due to Néel and Brownian relaxations for superparamagnetic nanoparticles.

Nanoparticles undergo Néel relaxation process with a characteristic relaxation time called Néel relaxation time, τ_N is given by,

$$\tau_N = \tau_0 \exp[K_{eff}V/k_B T] \quad (1)$$

where τ_0 is the attempt frequency has a value in the range of 10^{-13} - 10^{-9} s, K_{eff} is the effective anisotropy, k_B is the Boltzmann constant and T is the temperature. The K_{eff} is one of the key parameter that governs the heating efficiency of the magnetic nanoparticles.

Besides Néel relaxation, Brown relaxation occurs for the particles suspended in a fluid suspension with a viscosity η . In this case, the magnetic nanoparticle physically rotates itself within the fluid at a characteristic relaxation called Brown relaxation time, τ_B , is given by

$$\tau_B = \frac{3\eta V_h}{k_B T} \quad (2)$$

where η is the viscosity of the medium where the nanoparticles dispersed in, V_h is the hydrodynamic volume of the nanoparticles.

Both the relaxation mechanisms contribute independently on the magnetization of colloidal magnetic nanoparticles subjected to alternating magnetic field. The combined relaxation time is called effective relaxation time, τ_{eff} , is given by

$$\tau_{eff} = \frac{\tau_B \tau_N}{\tau_B + \tau_N} \quad (3)$$

As seen from equation the shorter relaxation time controls the effective time of reversal. This means that reversal occurs by the process with the smallest relaxation time constant (Dutz & Hergt, 2013). Néel relaxation emerged as a dominant process for smaller particle sizes, while Brown relaxation time dominates in case of larger in low viscous media (Deatsch & Evans, 2014). The contribution of Brown relaxation might be considered insignificant when magnetic particles are injected into tissue (Dutz, Kettering, Hilger, Müller, & Zeisberger, 2011).

Regardless of heating origin, measuring the amount of induced heat via loss and relaxation mechanisms is essential in order to compare the efficiency of magnetic nanoparticles. The heating efficiency in magnetic hyperthermia is presented by the specific loss power (SLP), also denoted as specific absorption rate (SAR). In non-adiabatic condition, the value of SLP can be experimentally calculated by determining the initial rate of temperature increase of a system under alternating magnetic field. SLP can be expressed in terms of Watts/gram (W/g) by the following equation,

$$SLP = C \frac{m_s \Delta T}{m_m \Delta t} \quad (4)$$

where C is the volume specific heat capacity of the sample solution, m_s is the mass of solution, m_m is the mass of magnetic material in the solution and $\Delta T/\Delta t$ is the initial slope of the temperature versus time dependence. SLP can also be defined according to the magnetic field frequency and amplitude by the following equation,

$$SLP(f, H) = \frac{P(f, H)}{\rho} = \frac{\pi \mu_0 \chi'' H^2 f}{\rho} \quad (5)$$

where ρ is the mass density of the magnetic material. H , f , μ_0 and χ'' are the amplitude of magnetic field, frequency of the magnetic field, magnetic permeability of free space and complex part of the susceptibility, respectively.

For an efficient magnetic hyperthermia SLP value is desired to be as large as possible. The SLP is drastically depends on structural properties of magnetic nanoparticles, such as particle size, shape and composition. In addition to structural properties of magnetic nanoparticles, the environmental properties include the viscosity of medium, frequency and amplitude of the external magnetic field can significantly alter the SLP during the magnetic hyperthermia experiments. In order to get an improved SLP, all parameters have to be optimized. There is found a large number of publications on optimizing the parameters for efficient hyperthermia related to SLP in the literature (Halgamuge & Song, 2020; Kwon et al., 2016; Liu et al., 2012; Sohn & Victora, 2010). The studies on this context related to biological issues mainly include synthesis and characterizations of magnetic nanoparticles in-vitro and in-vivo conditions.

5. IN-VITRO AND IN-VIVO STUDIES IN MAGNETIC HYPERTHERMIA

In magnetic hyperthermia research, the studies include the characterization of physical, chemical and biological properties of the nanoparticles. These characterizations are studied by in-vitro and in-vivo methods which are crucial to translate the new cancer diagnosis and treatment methods into routine clinical applications.

5.1. IN-VITRO STUDIES

In-vitro studies are those of performed in a controlled environment (such as a test tubes or laboratory dish) that simulates the real organs of living organisms. Fluidic, hydrogel and polymeric media, cell cultures and dead tissue are used as in-vitro environments. In-vitro studies are important to provide a valuable insight for future in-vivo studies.

In-vitro experimental analysis in magnetic hyperthermia research is essential to test the suitability for biological media of the nanoparticles. Besides providing a valuable knowledge about the biological suitability and efficiency of the nanoparticles, in-vitro experiments also provide a good insight about the other environmental parameters (such as the frequency and amplitude of applied magnetic field, viscosity of the medium and alternating magnetic field exposure time) which are necessary to be optimized for in-vivo tests of magnetic hyperthermia measurements.

In a much recent study, Minaei et al (2019), synthesized TMZ (temozolomide)-loaded FA (folic acid ligand)-conjugated magnetite triblock copolymers to investigate the in-vitro anti-cancer efficacy of these multifunctional nanoparticles combining magnetic hyperthermia in glioblastoma cancer cells. A high SAR values of 530 W/g was found from magnetic hyperthermia measurements. In-vitro results showed that TMZ-MNP-FA are very promising for localized combined chemo-hyperthermia. There can be found several publications about in-vitro studies on magnetic hyperthermia (Bhardwaj, Parekh, & Jain, 2020; Gkanas, 2013; Iacovita et al., 2020; Ramirez-Nuñez, Jimenez-Garcia, Goya, Sanz, & Santoyo-Salazar, 2018). In-vitro studies are key initial step of a clinical experiment to test a hypothesis. In the case of positive results from these studies, researchers move on to in-vivo experiments before clinical tests on humans.

5.2. IN-VIVO STUDIES

In-vivo refers to a medical experiment is done in the living organ or whole body. The animal models, such as mice, rats and rodents are used are used as in-vivo environments.

Very recently, Rego et al (2019) synthesized stable aminosilane-coated superparamagnetic iron oxide nanoparticles to evaluate the potential of magnetic hyperthermia in glioblastoma tumor model. First, the heating potential of the nanoparticles through specific absorption rate value were investigated under different frequencies and intensities of alternating magnetic field in-vitro to evaluate the best conditions of frequency and intensity of alternating magnetic field. Then, magnetic hyperthermia measurements were performed under these best conditions. The cell death of 52.0 % (in-vitro) and 32.8 % (in-vivo) and a high SAR of 195 W/g was

achieved. These results indicated that magnetic hyperthermia using aminosilane-coated superparamagnetic iron oxide nanoparticles is promising for the therapeutic process of glioblastoma tumors in animal model. There can be found several publications about in-vivo studies on magnetic hyperthermia (Y. Chen et al., 2014; Ha et al., 2019; Kim, Kim, Kim, Shim, & Lee, 2007)

6. CONCLUSIONS AND FUTURE PERSPECTIVES

Hyperthermia is a very successful cancer treatment method. This method can be employed alone or combined with conventional therapies to enhance its efficacy. Remarkably, hyperthermia has been demonstrated to provide numerous advantages when combined with chemotherapy and/or radiotherapy in nano platforms. The combined therapies which have more advantages and superiority compared to conventional therapies appear as innovative cancer treatments of recent years.

Although all the advantages of combined therapy there is still no routine in clinical practice of cancer treatments by using them. Actually, there are several drawbacks that must be overcome in order to translate these new therapies into a routine clinical cancer diagnosis and treatment. Difficulty in temperature control and temperature measurement at cell level, uncontrollable temperature release on healthy cells, non-uniform heat dissipation through the tumor region, lack of non-invasive transportation of nanoparticles to tumor region, small penetration depth and low solubility and toxicity of therapeutic drugs are the main problems that still need to be solved in current cancer therapy treatments.

The use of magnetic nanoparticles in hyperthermia as heat agents provide a more efficient cancer therapy modality while eliminating the aforementioned problems. The improvements that can be achieved in cancer treatments by incorporating magnetic nanoparticles into hyperthermia are as follows:

- a) The less complications and side effects compared to conventional modalities.
- b) The temperature control on tumor region by using self-regulating magnetic nanoparticles,
- c) The accessibility to deeper tissues with higher penetration,
- d) The successive of more efficient heating of magnetic hyperthermia by precise control of size and morphology of magnetic nanoparticles,
- e) The transportation of therapeutic drugs non-invasively by magnetic nanoparticles,

- f) The controllable releasing of therapeutic drugs using porous magnetic nanoparticles,
- g) The easy functionalization properties of magnetic nanoparticles allow the development of multifaceted approach to cancer treatment.

REFERENCES

- Ahmad, A., Gupta, A., Ansari, M. M., Vyawahare, A., Jayamurugan, G., & Khan, R. (2020). Hyperbranched Polymer-Functionalized Magnetic Nanoparticle-Mediated Hyperthermia and Niclosamide Bimodal Therapy of Colorectal Cancer Cells. *ACS Biomaterials Science and Engineering*, 6(2), 1102–1111. <https://doi.org/10.1021/acsbiomaterials.9b01947>
- Anghileri, L. J., & Robert, J. (2019). *Hyperthermia in Cancer Treatment* (L. J. Anghileri & J. Robert, Eds.). <https://doi.org/10.1201/9780429266546>
- Araújo-Barbosa, S., & Morales, M. A. (2019). Nanoparticles of Ni_{1-x}Cu_x alloys for enhanced heating in magnetic hyperthermia. *Journal of Alloys and Compounds*, 787, 935–943. <https://doi.org/10.1016/j.jallcom.2019.02.148>
- Beg, S., Rahman, M., Jain, A., Saini, S., Midoux, P., Pichon, C., ... Akhter, S. (2017). Nanoporous metal organic frameworks as hybrid polymer–metal composites for drug delivery and biomedical applications. *Drug Discovery Today*, 22(4), 625–637. <https://doi.org/10.1016/j.drudis.2016.10.001>
- Bhardwaj, A., Parekh, K., & Jain, N. (2020). In vitro hyperthermic effect of magnetic fluid on cervical and breast cancer cells. *Scientific Reports*, 10(1), 1–13. <https://doi.org/10.1038/s41598-020-71552-3>
- Brezovich, I. A., Atkinson, W. J., & Chakraborty, D. P. (1984). Temperature distributions in tumor models heated by self-regulating nickel-copper alloy thermoseeds. *Medical Physics*, 11(2), 145–152. <https://doi.org/10.1118/1.595490>
- Busch, W. (1866). Über den einfluss Welch heftigere Erysipeln auf organisiente Neubildungen aususuben. *Verhandl Naturn Preuss Rein Westphal*, 23, 28. Retrieved from <https://ci.nii.ac.jp/naid/10029676233>
- Çelik, Ö., & Firat, T. (2018). Synthesis of FeCo magnetic nanoalloys and investigation of heating properties for magnetic fluid hyperthermia. *Journal of Magnetism and Magnetic Materials*, 456, 11–16. <https://doi.org/10.1016/j.jmmm.2018.01.090>
- Chaturvedi, V. K., Singh, A., Singh, V. K., & Singh, M. P. (2018). Cancer Nanotechnology: A New Revolution for Cancer Diagnosis and Therapy. *Current Drug Metabolism*, 20(6), 416–429. <https://doi.org/10.2174/1389200219666180918111528>
- Chen, J., Liu, J., Hu, Y., Tian, Z., & Zhu, Y. (2019). Metal-organic framework-coated magnetite nanoparticles for synergistic magnetic

- hyperthermia and chemotherapy with pH-triggered drug release. *Science and Technology of Advanced Materials*, 20(1), 1043–1054. <https://doi.org/10.1080/14686996.2019.1682467>
- Chen, Y., Jiang, L., Wang, R., Lu, M., Zhang, Q., Zhou, Y., ... Zheng, Y. (2014). Injectable Smart Phase-Transformation Implants for Highly Efficient In Vivo Magnetic-Hyperthermia Regression of Tumors. *Advanced Materials*, 26(44), 7468–7473. <https://doi.org/10.1002/adma.201402509>
- Cryer, A. M., & Thorley, A. J. (2019, June 1). Nanotechnology in the diagnosis and treatment of lung cancer. *Pharmacology and Therapeutics*, Vol. 198, pp. 189–205. <https://doi.org/10.1016/j.pharmthera.2019.02.010>
- Deatsch, A. E., & Evans, B. A. (2014). Heating efficiency in magnetic nanoparticle hyperthermia. *Journal of Magnetism and Magnetic Materials*, 354, 163–172. <https://doi.org/10.1016/j.jmmm.2013.11.006>
- Deger, S., Boehmer, D., Türk, I., Roigas, J., Budach, V., & Loening, S. A. (2002). Interstitial hyperthermia using self-regulating thermoseeds combined with conformal radiation therapy. *European Urology*, 42(2), 147–153. [https://doi.org/10.1016/S0302-2838\(02\)00277-4](https://doi.org/10.1016/S0302-2838(02)00277-4)
- Denny, M. S., Kalaj, M., Bentz, K. C., & Cohen, S. M. (2018). Multicomponent metal-organic framework membranes for advanced functional composites. *Chemical Science*, 9(47), 8842–8849. <https://doi.org/10.1039/c8sc02356e>
- Desai, A. V., Sharma, S., Let, S., & Ghosh, S. K. (2019, September 15). N-donor linker based metal-organic frameworks (MOFs): Advancement and prospects as functional materials. *Coordination Chemistry Reviews*, Vol. 395, pp. 146–192. <https://doi.org/10.1016/j.ccr.2019.05.020>
- Ding, Q., Liu, D., Guo, D., Yang, F., Pang, X., Che, R., ... Gu, N. (2017). Shape-controlled fabrication of magnetite silver hybrid nanoparticles with high performance magnetic hyperthermia. *Biomaterials*, 124, 35–46. <https://doi.org/10.1016/j.biomaterials.2017.01.043>
- Dutz, S., & Hergt, R. (2013). Magnetic nanoparticle heating and heat transfer on a microscale: Basic principles, realities and physical limitations of hyperthermia for tumour therapy. *International Journal of Hyperthermia*, 29(8), 790–800. <https://doi.org/10.3109/02656736.2013.822993>
- Dutz, S., Kettering, M., Hilger, I., Müller, R., & Zeisberger, M. (2011). Magnetic multicore nanoparticles for hyperthermia-influence of

- particle immobilization in tumour tissue on magnetic properties. *Nanotechnology*, 22(26), 265102. <https://doi.org/10.1088/0957-4484/22/26/265102>
- Fortin, J. P., Wilhelm, C., Servais, J., Ménager, C., Bacri, J. C., & Gazeau, F. (2007). Size-sorted anionic iron oxide nanomagnets as colloidal mediators for magnetic hyperthermia. *Journal of the American Chemical Society*, 129(9), 2628–2635. <https://doi.org/10.1021/ja067457e>
- Gaballah, S. T., El-Nazer, H. A., Abdel-Monem, R. A., El-Liethy, M. A., Hemdan, B. A., & Rabie, S. T. (2019). Synthesis of novel chitosan-PVC conjugates encompassing Ag nanoparticles as antibacterial polymers for biomedical applications. *International Journal of Biological Macromolecules*, 121, 707–717. <https://doi.org/10.1016/j.ijbiomac.2018.10.085>
- Gilchrist, R. K., Medal, R., Shorey, W. D., Hanselman, R. C., Parrott, J. C., & Taylor, C. B. (1957). Selective inductive heating of lymph nodes. *Annals of Surgery*, 146(4), 596–606. <https://doi.org/10.1097/00000658-195710000-00007>
- Gkanas, E. I. (2013). In vitro magnetic hyperthermia response of iron oxide MNP's incorporated in DA3, MCF-7 and HeLa cancer cell lines. *Central European Journal of Chemistry*, 11(7), 1042–1054. <https://doi.org/10.2478/s11532-013-0246-z>
- Green, J. J., & Elisseeff, J. H. (2016). Mimicking biological functionality with polymers for biomedical applications. *Nature*, 540(7633), 386–394. <https://doi.org/10.1038/nature21005>
- Grodzinski, P., Kircher, M., Goldberg, M., & Gabizon, A. (2019). Integrating Nanotechnology into Cancer Care. *ACS Nano*, 13(7), 7370–7376. <https://doi.org/10.1021/acsnano.9b04266>
- Guardia, P., Riedinger, A., Kakwere, H., Gazeau, F., & Pellegrino, T. (2014). Magnetic Nanoparticles for Magnetic Hyperthermia and Controlled Drug Delivery. In *Bio- and Bioinspired Nanomaterials* (Vol. 9783527335, pp. 139–172). <https://doi.org/10.1002/9783527675821.ch06>
- Ha, P. T., Le, T. T. H., Bui, T. Q., Pham, H. N., Ho, A. S., & Nguyen, L. T. (2019). Doxorubicin release by magnetic inductive heating and in vivo hyperthermia-chemotherapy combined cancer treatment of multifunctional magnetic nanoparticles. *New Journal of Chemistry*, 43(14), 5404–5413. <https://doi.org/10.1039/C9NJ00111E>
- Hadjipanayis, C. G., Bonder, M. J., Balakrishnan, S., Wang, X., Mao, H., & Hadjipanayis, G. C. (2008). Metallic iron nanoparticles for MRI

- contrast enhancement and local hyperthermia. *Small*, 4(11), 1925–1929. <https://doi.org/10.1002/sml.200800261>
- Halgamuge, M. N., & Song, T. (2020). Optimizing heating efficiency of hyperthermia: Specific loss power of magnetic sphere composed of superparamagnetic nanoparticles. *Progress In Electromagnetics Research B*, 87, 1–17. <https://doi.org/10.2528/PIERB19121702>
- Hartshorn, C. M., Bradbury, M. S., Lanza, G. M., Nel, A. E., Rao, J., Wang, A. Z., ... Grodzinski, P. (2018, January 23). Nanotechnology Strategies to Advance Outcomes in Clinical Cancer Care. *ACS Nano*, Vol. 12, pp. 24–43. <https://doi.org/10.1021/acsnano.7b05108>
- Iacovita, C., Fizeşan, I., Pop, A., Scorus, L., Dudric, R., Stiufluic, G., ... Lucaciu, C. M. (2020). In Vitro Intracellular Hyperthermia of Iron Oxide Magnetic Nanoparticles, Synthesized at High Temperature by a Polyol Process. *Pharmaceutics*, 12(5), 424. <https://doi.org/10.3390/pharmaceutics12050424>
- Kafrouni, L., & Savadogo, O. (2016). Recent progress on magnetic nanoparticles for magnetic hyperthermia. *Progress in Biomaterials*, 5(3–4), 147–160. <https://doi.org/10.1007/s40204-016-0054-6>
- Kargozar, S., & Mozafari, M. (2018). Nanotechnology and Nanomedicine: Start small, think big. *Materials Today: Proceedings*, 5(7), 15492–15500. <https://doi.org/10.1016/j.matpr.2018.04.155>
- Kawahara, I., Goto, K., Kodama, K., Luo, Y., Fujiwara-Tani, R., Mori, T., ... Kuniyasu, H. (2019). Magnetic Hyperthermia Using Self-Controlled Heating Elements Consisting of Fe-Al Milling Alloy Induces Cancer Cell Apoptosis while Preserving Skeletal Muscle. *Pathobiology*, 86(5–6), 254–262. <https://doi.org/10.1159/000501524>
- Keskin, S., & Kizilel, S. (2011). Biomedical Applications of Metal Organic Frameworks. *Industrial and Engineering Chemistry Research*, 50(4), 1799–1812. <https://doi.org/10.1021/ie101312k>
- Kim, D. H., Kim, K. N., Kim, K. M., Shim, I. B., & Lee, Y. K. (2007). In vitro & in vivo toxicity of CoFe₂O₄ for application to magnetic hyperthermia. *NSTI Nanotech*, 748–751. Retrieved from <https://yonsei.pure.elsevier.com/en/publications/in-vitro-amp-in-vivo-toxicity-of-cofesub2subosub4sub-for-applicat>
- Kumar, C. S. S. R., & Mohammad, F. (2011, August 14). Magnetic nanomaterials for hyperthermia-based therapy and controlled drug delivery. *Advanced Drug Delivery Reviews*, Vol. 63, pp. 789–808. <https://doi.org/10.1016/j.addr.2011.03.008>
- Kwon, Y. S., Sim, K., Seo, T., Lee, J. K., Kwon, Y., & Yoon, T. J. (2016). Optimization of magnetic hyperthermia effect for breast cancer stem

- cell therapy. *RSC Advances*, 6(109), 107298–107304. <https://doi.org/10.1039/c6ra22382f>
- Liu, X. L., Fan, H. M., Yi, J. B., Yang, Y., Choo, E. S. G., Xue, J. M., ... Ding, J. (2012). Optimization of surface coating on Fe₃O₄ nanoparticles for high performance magnetic hyperthermia agents. *Journal of Materials Chemistry*, 22(17), 8235–8244. <https://doi.org/10.1039/c2jm30472d>
- Minaei, S. E., Khoei, S., Khoee, S., Vafashoar, F., & Mahabadi, V. P. (2019). In vitro anti-cancer efficacy of multi-functionalized magnetite nanoparticles combining alternating magnetic hyperthermia in glioblastoma cancer cells. *Materials Science and Engineering C*, 101, 575–587. <https://doi.org/10.1016/j.msec.2019.04.007>
- Moorthy, M. S., Bharathiraja, S., Manivasagan, P., Oh, Y., Phan, T. T. V., Mondal, S., ... Oh, J. (2018). Synthesis of Fe₃O₄ modified mesoporous silica hybrid for pH-responsive drug delivery and magnetic hyperthermia applications. *Journal of Porous Materials*, 25(4), 1251–1264. <https://doi.org/10.1007/s10934-017-0536-5>
- Nguyen, L. H. (2016). Influence of Saturation Magnetization And Viscosity on Specific Loss Power for CoFe₂O₄ and MnFe₂O₄ Magnetic Nanoparticles. *Vietnam Journal of Science and Technology*, 54(1A), 33. <https://doi.org/10.15625/2525-2518/54/1a/11803>
- Ortega, D., & Pankhurst, Q. A. (2012). Magnetic Hyperthermia. In *Nanoscience: Volume 1: Nanostructures Trough Chemistry* (pp. 60–88). <https://doi.org/10.1039/9781849734844-00060>
- Pradhan, P., Giri, J., Samanta, G., Sarma, H. D., Mishra, K. P., Bellare, J., ... Bahadur, D. (2007). Comparative evaluation of heating ability and biocompatibility of different ferite-based magnetic fluids for hyperthermia application. *Journal of Biomedical Materials Research - Part B Applied Biomaterials*, 81(1), 12–22. <https://doi.org/10.1002/jbm.b.30630>
- Ramirez-Núñez, A. L., Jimenez-Garcia, L. F., Goya, G. F., Sanz, B., & Santoyo-Salazar, J. (2018). In vitro magnetic hyperthermia using polyphenol-coated Fe₃O₄/γ-Fe₂O₃ nanoparticles from *Cinnamomum verum* and *Vanilla planifolia*: The concert of green synthesis and therapeutic possibilities. *Nanotechnology*, 29(7), 074001. <https://doi.org/10.1088/1361-6528/aaa2c1>
- Rego, G. N. de A., Mamani, J. B., Souza, T. K. F., Nucci, M. P., Silva, H. R. da, & Gamarra, L. F. (2019). Therapeutic evaluation of magnetic hyperthermia using Fe₃O₄-aminosilane-coated iron oxide


- nanoparticles in glioblastoma animal model. *Einstein (Sao Paulo, Brazil)*, 17(4), 1–9. https://doi.org/10.31744/einstein_journal/2019AO4786
- Salati, A., Ramazani, A., & Almasi Kashi, M. (2020). Tuning hyperthermia properties of FeNiCo ternary alloy nanoparticles by morphological and magnetic characteristics. *Journal of Magnetism and Magnetic Materials*, 498, 166–172. <https://doi.org/10.1016/j.jmmm.2019.166172>
- Seppälä, J., Van Bochove, B., & Lendlein, A. (2020). Developing Advanced Functional Polymers for Biomedical Applications. *Biomacromolecules*, 21(2), 273–275. <https://doi.org/10.1021/acs.biomac.9b01701>
- Sohn, H., & Victora, R. H. (2010). Optimization of magnetic anisotropy and applied fields for hyperthermia applications. *Journal of Applied Physics*, 107(9), 596. <https://doi.org/10.1063/1.3355903>
- Sun, D., Jang, S., Yim, S. J., Ye, L., & Kim, D. P. (2018). Metal Doped Core–Shell Metal–Organic Frameworks@Covalent Organic Frameworks (MOFs@COFs) Hybrids as a Novel Photocatalytic Platform. *Advanced Functional Materials*, 28(13), 1707110. <https://doi.org/10.1002/adfm.201707110>
- Sun, Y., Zheng, L., Yang, Y., Qian, X., Fu, T., Li, X., ... Tan, W. (2020). Metal–Organic Framework Nanocarriers for Drug Delivery in Biomedical Applications. *Nano-Micro Letters*, 12(1), 1–29. <https://doi.org/10.1007/s40820-020-00423-3>
- Vilaça, N., Gallo, J., Fernandes, R., Figueiredo, F., Fonseca, A. M., Baltazar, F., ... Bañobre-López, M. (2019). Synthesis, characterization and: In vitro validation of a magnetic zeolite nanocomposite with T 2-MRI properties towards theranostic applications. *Journal of Materials Chemistry B*, 7(21), 3351–3361. <https://doi.org/10.1039/c9tb00078j>
- Yezdani, U., Khan, M. G., Kushwah, N., Verma, A., & Khan, F. (2018). Application of nanotechnology in diagnosis and treatment of various diseases and its future advances in medicine. *World Journal of Pharmacy and Pharmaceutical Sciences*, 7(11), 1611–1633. <https://doi.org/10.20959/wjpps201818-12703>
- Zottel, A., Videtič Paska, A., & Jovčevska, I. (2019). Nanotechnology Meets Oncology: Nanomaterials in Brain Cancer Research, Diagnosis and Therapy. *Materials*, 12(10), 1588. <https://doi.org/10.3390/ma12101588>

CHAPTER III

PARTIAL PURIFICATION AND CHARACTERIZATION OF PEROXIDASE FROM ZEFERAN PEACH (*Prunus persica L.*)

Ayşe Türkhan

(Asst. Prof. Dr.); Iğdır University, e-mail: ayse.turkhan@igdir.edu.tr,

 ORCID 0000-0002-2195-9435

INTRODUCTION

Peroxidases (POD) (E.C. 1.11.1.7) is an enzyme belonging to the oxidoreductase family, and they are known as heme proteins containing ferriprotoporphyrin IX as a prosthetic group. The peroxidase enzyme catalyses numerous reactions like oxidation of various organic and inorganic compounds with a tendency to give electrons, along with reduction of such peroxides as hydrogen that accepts these electrons (Adams, 1978; Whitaker, 1994).

POD is known to catalyse dehydrogenation of many aromatic molecules such as hydroquinone and phenol, among which are pyrogallol, 2-toluidine, guaiacol, leucomalachite green, 2-cresol, propionyl promazine, and some azo dye derivatives (Pütter and Becker, 1987; Van-Huytstee, 1987). Plant peroxidases can achieve oxidation of a number of phenolic molecules, such as catechin, guaiacol, chlorogenic acid, and catechol against peroxide (Onsa, et al., 2004).

Peroxidases constitute one of the main enzyme groups used in industrial production and applications. The large number of pollutants stemming from industrial applications pose a menace not only to the environment but also to ecological balance as well. Peroxidases are also among the enzymes utilised effectively in preventing environmental pollution. Some other applications for which peroxidases are widely used are removal of phenolic compounds (Hamid and Rehman, 2009), detoxification of industrial dyes (Chivukula, et al., 1995), biosensor construction (Jia, et al., 2002), pulp industry (Khalid, et al., 2009), analytical kits, and diagnostic kits (Heller and Vreeke, 1997; Agostini, et al., 2002), degradation of chlorinated insecticides (Quintero, et al., 2008), and organic polymerization reactions (Liu, et al., 1999).

Since the peroxidase enzyme is eligible of industrial use, new sources are constantly being searched for the purification of this enzyme. Among the sources studied or this enzyme up to the present time have been Kudret Pomegranate (*Momordica charantia Descourt*) (Altınkaynak, et

al., 2020), Onion Roots (Öztekin, 2020), lettuce (*Lactuca sativa* L.) (Hu, et al., 2012), coarse lemon (*Citrus jambhiri*) (Mohamed, et al., 2008), turnip (*Brassica rapa*) (Motamed, et al., 2009), and zucchini (*Cucurbita pepo* L.) (Wang, et al., 2019). In this study, zeferan, a local peach variety of Iğdır province, was used for the first time as a source of peroxidase. Many pollutants attributable to various industrial applications pose a serious menace to the environment. The fact that peroxidase enzyme is capable of significantly reducing environmental pollution makes it essential that this enzyme should be obtained from as many sources as possible. In this study, peroxidase from zeferan peach variety was partially purified and biochemical properties such as optimum pH, optimum temperature K_m and V_{max} , thermal stability, pH stability were investigated.

MATERIAL AND METHODS

CHEMICALS USED

Guaiacol, hydrogen peroxide (H_2O_2 , 30%), Sodium acetate ($NaCH_3COO$), potassium dihydrogen phosphate (KH_2PO_4) and Tris-HCl were all obtained from Sigma-Aldrich Chemie GmbH Steinheim, Germany. The present study used zeferan, a local peach variety occurring in Iğdır central Melekli neighbourhood was used as the source of peroxidase enzyme. The Zeferan peach was collected in september and preserved at $-20\text{ }^\circ\text{C}$.

PREPARATION OF RAW ENZYME EXTRACT FROM ZEFERAN PEACH (*PRUNUS PERSICA* L.) AND PARTIAL PURIFICATION

Zeferan (*Prunus persica* L.) was collected from the peach orchard in Iğdır, Turkey and stored at $-20\text{ }^\circ\text{C}$ until the present study was launched. 35 grams of sample were taken while preparing the enzyme solution. The samples were freeze-thawed and pounded in a mortar. Afterwards, 70 mL of 50 mM phosphate (pH 6.0) buffer was added (Aydemir, 2004). The sample was filtered through a 4-layered cheesecloth and the filtrate obtained was centrifuged at $4\text{ }^\circ\text{C}$, 10,000 rpm for 30 minutes. The supernatant obtained was used as the crude enzyme extract.

To the obtained supernatant, cold acetone with the same volume was added by stirring slowly in an ice bath. The enzyme extract was centrifuged at $4\text{ }^\circ\text{C}$ for 30 minutes at 10,000 rpm after having been left at $4\text{ }^\circ\text{C}$ overnight, following which the supernatant part was discarded and the precipitate were dissolved in 15 mL of pH 6.0 phosphate buffer (Özen et al., 2004).

DETERMINATION OF PEROXIDASE ACTIVITY

Peroxidase activity determination is based on the principle of measuring the increase in absorbance at 470 nm in 3 minutes of the colored product formed by the oxidation of guaiacol (45 mM) known as the chromogenic substrate in the presence of H₂O₂ (22.5 mM) (Sisecioglu et al. 2010). Enzyme activity was calculated according to Kalin et al., 2014 (Kalin, et al., 2014).

DETERMINATION OF PROTEIN

Protein determination was achieved the Bradford method using bovine albumin (BSA) as the standard protein. The measurements were performed at 595 nm via the UV-vis spectrophotometer (Bradford, 1976).

OPTIMUM pH

Optimum pH for POD was examined separate activity measurements using 50 mM glisin-HCl (pH 3,0), 50 mM sodyum asetat (pH 4,0 ve 5,0), 50 mM fosfat (pH 6,0 ve 7,0) and 50 mM Tris- HCl (pH 8,0 ve 9,0) buffers. A pH -% relative activity graphic was plotted to present results. The pH with the highest activity was determined as the optimum pH.

OPTIMUM TEMPERATURE

In order to determine the optimum temperature of POD, the enzyme activity was determined at different temperatures varying between 10-70° C with intervals of 10 °C by means of the guaiacol / H₂O₂ substrate (Kalin, et al., 2014). A temperature-% relative activity graphic was drawn to present the results. The temperature with the highest activity was determined as the optimum temperature.

DETERMINATION OF Km AND Vmax VALUES

To determine the affinity of POD with the guaiacol substrate, peroxidase activity was measured at 1.67-20 mM substrate concentration, keeping the H₂O₂ concentration constant. Lineweaver-Burk graphics were drawn by calculating 1/V and 1/[S] values from the results. Based on this graphic, the Km and Vmax values of guaiacol were determined (Lineweaver and Burk, 1934).

DETERMINATION OF pH STABILITY

The pH stability of zeferan peroxidase were determine using 50 mM glycine-HCl (pH 3.0), 50 mM sodium acetate (pH 4.0 and 5.0), 50 mM phosphate (pH 6.0 and 7.0), and 50 mM Tris-HCl (pH 8.0) buffers. 1 mL of buffer solutions (for each pH):1 ml of the enzyme solution were kept at + 4 ° C by being mixed. Activity measurements were made for 5 days. The

residual activity (%) - time graph was drawn from the obtained results (Kalin, 2012).

DETERMINATION OF THERMAL STABILITY

To determine the thermal stability of POD, the enzyme was incubated for 1 hour at 4 ° C and 30 ° C, with the intervals being 20 minutes. The activity determination was achieved under optimal conditions by rapidly cooling the enzyme thanks to an ice bath for 5 minutes. The activity of the enzyme that had not been exposed to any previous treatment was acknowledged to be 100%. Finally, the residual activity (%) of the incubated enzymes was calculated (Kolcuoğlu, 2018).

RESULTS AND DISCUSSION

Previous studies have already elucidated the reaction mechanism by which guaiacol, which is used as a peroxidase substrate, is oxidized. This reaction mechanism has revealed that coloured 3,3'-dimethoxy-4,4'-biphenoquinone compound forms as a result of oxidation of guaiacol (Doerge, et al., 1997).

Among the sources studied or this enzyme up to the present time have been Kudret Pomegranate (*Momordica charantia* Descourt) (Altunkaynak, et al., 2020), Onion Roots (Öztekin, 2020), lettuce (*Lactuca sativa* L.) (Hu, et al., 2012), coarse lemon (*Citrus jambhiri*) (Mohamed, et al., 2008), turnip (*Brassica rapa*) (Motamed, et al., 2009), and zucchini (*Cucurbita pepo* L.) (Wang, et al., 2019).

The peroxidase enzyme was partially purified from Zeferan Peach by 1.75-fold via the cold acetone precipitation (Table 1). In a study, the peroxidase enzyme was purified as an intermediate step from Turkish black radish (*Raphanus sativus* L.) 1.358 fold with ammonium sulphate precipitation and characterized (Şisecioğlu, et al., 2010), another study the peroxidase enzyme from *A. pallidus* (P26) was 4,95 fold partially purified as an intermediate step (Taslimi, 2013).

Table 1. Steps of Purification of The Peroxidase From Zeferan Peach (*Prunus Persica* L.)

Purification steps	Volume (mL)	Total activity (EU/mL. min)	Total protein (mg)	Specific activity (U/mg protein)	Yield (%)	Purification fold
Crude Extract	70	7,4907	5,6476	1,33	100	1
Acetone Precipitation	15	1,76715	0,7618	2,32	23,59	1,75

OPTIMUM pH

To determine the optimum pH of peroxidase, the activity measurements were achieved separately via different buffers whose pH varied from 3.0 to 9.0, for which a pH -% relative activity graphic was drawn afterwards. As a result, the peroxidase showed the highest activity at pH 6.0 (Figure 1). The optimum pH values of peroxidase purified from chard (*Beta Vulgaris* L. var. cicla) (Yaman, 2018), black radish (*Raphanus sativus* L.) (Şisecioğlu, et al., 2010), and turnip roots (Kalin, et al., 2014) were found to be 6.0, 6.0, and 6.5, respectively. Previous studies on the POD enzyme was found the optimum pH values to usually vary from 5.0 to 7.5 (Gülçin and Yıldırım, 2005; Kumar, et al., 2011; Köksal and Gülçin, 2008; Lavery, et al., 2010; Kalin et al., 2014).

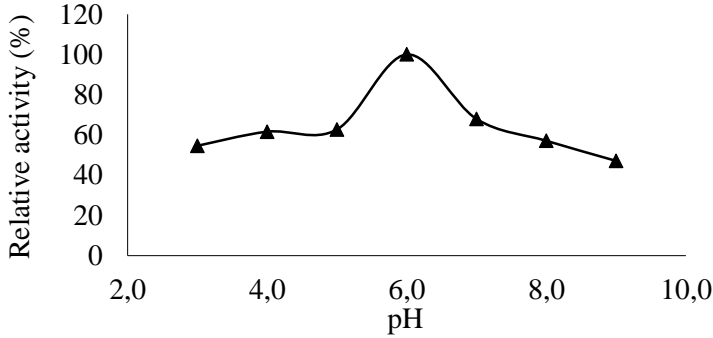


Figure 1. Optimum pH plot of zeferan peach peroxidase

OPTIMUM TEMPERATURE

To determine the optimum temperature value of the POD, activity determinations were achieved at 10-70 °C, with the intervals being 10 degrees. Through the data obtained, a temperature-% relative activity graph was drawn and the optimum temperature was found to be 30 °C (Figure 2). Peroxidase 40, 50, 60 °C was still found to retain 75% of its activity. This situation is important in terms of bringing this enzyme to the industry. The optimum temperatures of peroxidase from Turkish black radish and turnip roots are 30 °C (Kalin, et al., 2014). Previous studies into the POD enzyme have determined the optimum temperature value to generally vary between 30 and 50 °C (Gülçin and Yıldırım, 2005; Kumar, et al., 2011; Şisecioğlu, et al., 2010; Kalın, 2018). Peroxidase 40, 50, 60 °C was still found to retain 75% of its activity. This situation is important in terms of bringing this enzyme to the industry.

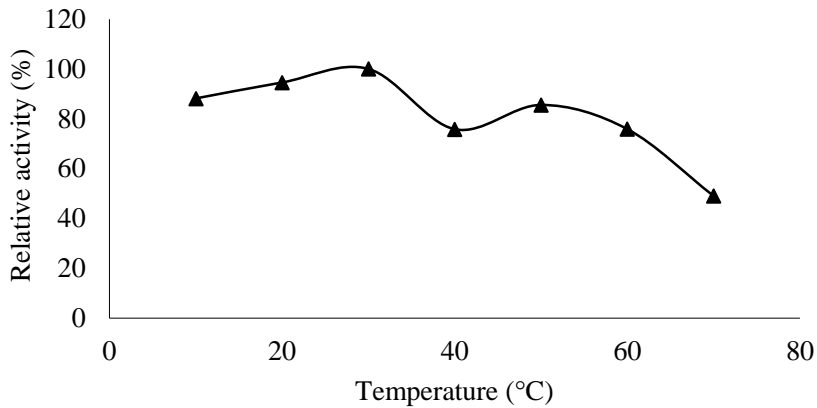


Figure 2. Optimum temperature plot of zeferan peach peroxidase

DETERMINATION OF K_m and V_{max} VALUES

The K_m and V_{max} values were determined for the guaiacol substrate of the Zeferan POD. For this purpose, the activity measurement was achieved in 6 different concentrations of guaiacol substrate between 1.67 and 20 mM under optimum conditions. K_m and V_{max} values for POD from Zeferan peach were calculated from the linear regression analysis of $1/V$ versus $1/[S]$. The K_m and V_{max} values of Zerefan POD were found to be 2.8 mM and 1.49 EU/mL.min, respectively (Figure 3). The K_m and V_{max} values of peroxidase purified from Turkish black radish (*Raphanus sativus* L.) (Kalin, et al., 2014), turnip (Kalin, et al., 2014) and onion roots (Öztekin, 2020) were found to be (24.88 mM and 3.23 EU/mL.min), (4.09 mM and 0.797 EU/mL.min) and (3.44 mM and 0.32 EU/mL.min), respectively. It was observed that the affinity to the guaiacol substrate of the peroxidase enzyme obtained from different sources could exhibit variations.

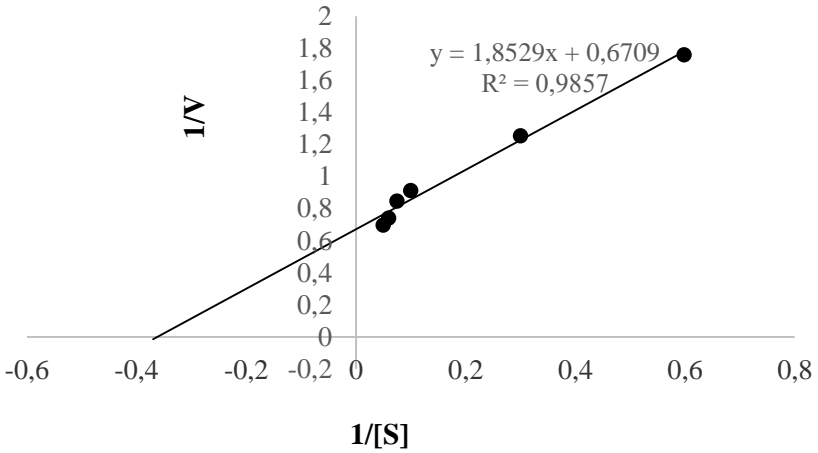


Figure 3. Lineweaver-Burk graph for zeferan peach peroxidase in the presence of guaiacol

DETERMINATION OF pH STABILITY

The pH stability of the POD was detected at 4 °C in the buffer solutions of between pH 3.0 and 8.0. After 24-h incubation at range pH 3.0 and 8.0 the POD residual activity was calculated above 85% (Figure 4). The POD activity was remained 68,05%, 63,23% and 62,83 after even 96-h incubation at pH 6.0, 7.0 and pH 8.0, respectively (Figure 4). Based on its pH values, the enzyme was observed to have exhibited different activities at different time intervals. High activity of peroxidase enzyme at pH 6.0, 7.0 and pH 8.0 is important for the usability of this enzyme. Similar results have also been reported in the literature (Şişecioglu, et al., 2010; Erol, 2019).

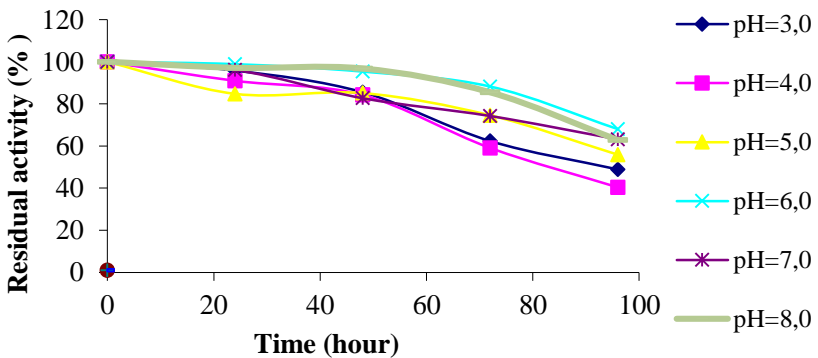


Figure 4. pH Stability of zeferan peach peroxidase

DETERMINATION OF THERMAL STABILITY

To determine the thermal stability of the zeferan peroxidase, the enzyme was incubated for one hour at 4 °C and 30 °C, respectively with intervals of 20 minutes. The activity determinations were achieved under optimal conditions through a rapid cooling in an ice bath for 5 minutes. The activity of the enzyme before any prior treatment was accepted to be 100%, and the percentage of residual activities of the incubated enzymes were calculated accordingly (Figure 5). The enzyme was observed to have maintained 88% and 78% of its activities after one hour of incubation at 4 °C and 30 °C, respectively (Figure 5). The good thermal stability of the peroxidase enzyme may allow the enzyme to be used for a long time at these temperatures. The thermal stability of horseradish peroxidase (HRP) was incubated at 20 °C - 50 °C for one hour, as a result of which the enzyme showed different activities at different temperatures (Erol, 2019).

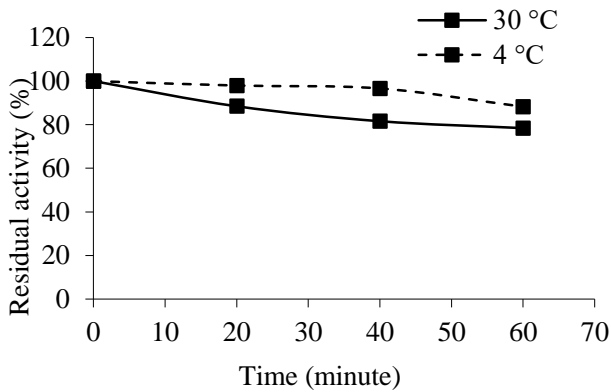


Figure 5. Thermal stability of zeferan peach peroxidase at 4 °C and 30°C

CONCLUSION

The peroxidase enzyme is a commercial enzyme capable of industrial use, new sources are continually being sought for purification of this enzyme. It is a fact that the enzymes utilized in many areas of industry have proved to be rather costly. For the sake of reducing this cost, investigations into cheaper enzyme production methods and sources are still in progress. The present studies, the peroxidase enzyme from zeferan, a local peach variety of Iğdır, was partially purified by 1.75 fold and characterized for the first time in the literature. Peroxidase partial purified from Zeferan peach has demonstrated high thermal and pH stability. The values obtained as a result of these characterization processes show that zeferan peroxidase, as an inexpensive enzyme source, can be purified by further purification techniques and brought to the industry by immobilization processes.

REFERENCES

- Adams, J. B. (1978). The inactivation and regeneration of peroxidase in relation to the high temperature-short time processing of vegetables. *Journal Food Technology*, 13, 281–297.
- Altınkaynak, C., Baldemir, A., Özdemir, N., Yılmaz, V., Öçsoy, İ. (2020). Kudret Narı (*Momordica charantia* Descourt.) Meyvesinden Saflaştırılan Peroksidaz Enzimi Kullanılarak Hibrit Nano Çiçekler Sentezlenmesi ve Direct blue 1 Gideriminde Kullanılabilirlikleri. *Bitlis Eren Üniversitesi Fen Bilimleri Dergisi*, 9, 573-583.
- Bradford, M. M. (1976). A rapid and sensitive method for the quantitation of microgram quantities of protein utilizing the principle of protein-dye binding. *Analytical Biochemistry*, 72, 248-254.
- Doerge, D. R., Divi, R. L., & Churchwell, M. I. (1997). Identification of the colored guaiacol oxidation product produced by peroxidases. *Analytical Biochemistry*, 250, 10–17.
- Erol, B. (2019). Katalaz ve Peroksidaz Enzimlerinin Parafin Destekte İmmobilize Edilerek Tekstil Boyası Giderilmesinde Kullanımının İncelenmesi. Yüksek Lisans Tezi Sivas Cumhuriyet Üniversitesi Fen Bilimleri Enstitüsü. Sivas.
- Gülçin, I., & Yıldırım, A. (2005). Purification and characterization of peroxidase from *Brasica oleracea* var. *Acephala*. *Asian Journal of Chemistry*, 17, 2175–2183.
- Hamid, H. & Rehman, K. U. (2009). Potential applications of peroxidases. *Food Chemistry*, 115(4), 1177-1186.
- Hu, Y., Wu, J., Luo, P., & Mo, Y. (2012). Purification and partial characterization of peroxidase from lettuce stems. *African Journal of Biotechnology*, 11(11), 2752-2756.
- Kalın, R., (2012). Peroksidaz Enziminin Afinite Kromatografisi Tekniği İle Karaturp (*Raphanus sativus* L.) ve Şalgamdan (*Brassica rapa* L.) Saflaştırılması ve Karakterizasyonu. Yüksek Lisans Tezi, Atatürk Üniversitesi, Fen Bilimleri Enstitüsü, Erzurum.
- Kalin, R., Atasever, A., & Ozdemir, H. (2014). Single-step purification of peroxidase by 4 aminobenzohydrazide from turkish blackradish and turnip roots. *Food Chemistry*, 335-340.

- Khalid, A., Arshad, M., & Crowley, D. E. (2009). Biodegradation potential of pure and mixed bacterial cultures for removal of 4-nitroaniline from textile dye wastewater. *Water Research*, 43(4), 1110-1116.
- Köksal, E., & Gülçin, I. (2008). Purification and characterization of peroxidase from cauliflower (*Brassica oleracea* L. var. *botrytis*) buds. *Protein and Peptide Letters*, 15, 320–326.
- Kolcuoğlu, Y., Kuyumcu, İ., & Colak, A. (2018). A catecholase from *Laccaria laccata* a wild edible mushroom and its catalytic efficiency in organic media. *Journal of Food Biochemistry*, 1–11.
- Kumar, R., Singh, K. A., Singh, V. K., & Jagannadham, M. V. (2011). Biochemical characterization of a peroxidase isolated from Caribbean plant: *Euphorbia cotinifolia*. *Process Biochemistry*, 46, 1350–1357.
- Lavery, C. B., Macinnis, M. C., Macdonald, M. J., Williams, J. B., Spencer, C. A., Burke, A. A., et al. (2010). Purification of peroxidase from horseradish (*Armoracia rusticana*) roots. *Journal of Agricultural and Food Chemistry*, 58, 8471–8476.
- Lineweaver, H., & Burk, D. (1934). The determination of enzyme dissociation constants. *Journal of the American Chemical Society*, 57(685), 1934.
- Mohamed, S. A., El-Badry, M. O., Drees, E. A., & Fahmy, A. S. (2008). Properties of a cationic peroxidase from *Citrus jambhiri* cv. Adalia. *Applied biochemistry and biotechnology*, 150(2), 127-137.
- Motamed, S., Ghaemmaghami, F., Alemzadeh, I., (2009). Turnip (*Brassica rapa*) Peroxidase: Purification and Characterization. *Industrial & Engineering Chemistry Research*, 48, 23, 10614-10618.
- Onsa, G. H., Saari, N., Selamat, J., & Bakar, J. (2004). Purification and characterization of membrane bound peroxidases from Metroxylon sagu. *Food Chemistry*, 85, 365–376.
- Öztekin, A. (2020). Guaiakol Peroksidazın Soğan Köklerinden Afinite Kromatografisi ile Saflaştırılması. *Iğdır Üniv. Fen Bil Enstitüsü Dergisi*, 10(2), 1163-1170.


- Pandey, V. P., Singh, S., Singh, R., & Dwivedi U.N. (2012). Purification and characterization of peroxidase from papaya (*Carica papaya*) fruit. *Applied biochemistry and biotechnology*, 167(2), 367-376.
- Pütter, J., Becker., & R. (1987). *Methods of Enzymatic Analysis Peroxidases*. Bergmeyer, Third Edition, VCH. 286, New York.
- Quintero, J. C., Moreira, M. T., Feijoo, G., & Lema, J. M. (2008). Screening of white rot fungal species for their capacity to degrade lindane and other isomers of hexachlorocyclohexane (HCH). *Ciencia e Investigacion Agraria*, 35(2), 123-132.
- Sisecioglu, M., Gulcin, İ., Cankaya, M., Atasever, A., Sehitoglu, M. H., Kaya, H.B., & Ozdemir, H. (2010). Purification and characterization of peroxidase from Turkish black radish (*Raphanus sativus* L). *Journal of Medicinal Plants Research*, 4(12), 1187-1196.
- Taslimi, P., 2013. *Aeribacillus pallidus* (P26) bakterisinden peroksidaz enziminin saflaştırılması ve kinetiğinin araştırılması, Yüksek Lisans Tezi, Atatürk Üniversitesi, Fen Bilimleri Enstitüsü, Erzurum.
- Van-Huystee, R. B., (1987). Some molecular aspects of plant peroxidase biosynthetic studies. *Ann. Rev. Plant. Physiol*, 38, 205-219.
- Wang., X. L., Wang, G. Y., Wang, Z. S., Wang, Y. Y., & Huang, R. (2019). Purification and characterization of peroxidase from zucchini (*Cucurbita pepo* L.). *Journal Of Food Processing And Preservation*, 43, 7.
- Whitaker, J. R., (1994). Catalase and peroxidase. In *Principles of Enzymology for the Food Sciences*, Whitaker, J. R., Ed., pp 565-578, Dekker: New York.
- Yaman, M. (2018). Peroksidazin Üç Fazlı Ayırma Yöntemi İle Pazıdan (*Beta Vulgaris* L. var. cicla) Saflaştırılması. Yüksek Lisans Tezi, İstanbul Üniversitesi-Cerrahpaşa Lisansüstü Eğitim Enstitüsü. İstanbul.

CHAPTER IV


PREPARATION AND CHARACTERIZATION OF URANIUM OXIDE MICROSPHERES BY INTERNAL SOL-GEL PROCESS

Süleyman İnan¹ & Berkan Çetinkaya²

¹(Assoc. Prof.) Ege University, e-mail: inansuleyman@gmail.com

 ORCID 0000-0003-4185-0979

²(Dr.) Ege University, e-mail: berkancetinkaya@gmail.com

 ORCID 0000-0003-0868-3603

1. INTRODUCTION

Population and income growth are the main factors causing the increase in primary energy consumption in the world. It is predicted that the population growth will significantly affect the global energy demand increase due to the developing industry and urbanization (Republic of Turkey Ministry of Energy and Natural Resources, 2017).

According to the scenarios, although the share of fossil fuels will decrease relatively in the period until 2040, these fuels will continue to be the dominant sources. The share of nuclear energy in primary energy resources is predicted to increase, and the share of renewable energy resources in 2040 is expected to be 16.1%. According to the current policies scenario, global electricity demand is expected to increase by 80% until 2040, with an annual average of 2.3%. Renewable resources are the energy resources with the fastest growth rate, with an annual average growth of 9.8%. Nuclear power will have an annual average growth rate of 2.3% and hydroelectricity an annual average growth rate of 1.8%. The growth rate of these three sources is more than the growth rate of total primary energy. The distribution of the world's primary energy demand by resources is given in Figure 1.

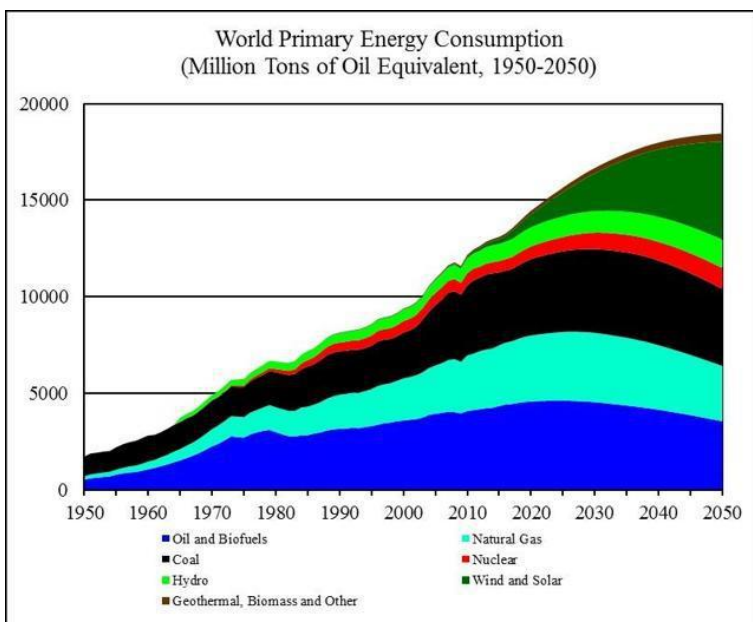


Figure 1: Distribution of World Primary Energy Demand by Resources (<https://seekingalpha.com/article/4083393-world-energy-2017minus-2050-annual-report>)

According to January 2020 data of the International Atomic Energy Agency (IAEA), there are 447 nuclear reactors operating in 30 countries. A total of 52 nuclear power plants are currently under construction in 19 countries including Turkey. 10% of the electricity production in the world is provided by nuclear energy (IAEA, 2019). As seen in Table 1, USA, which has the most nuclear power plants in the world with 96 power plants, obtained 19.3% of its electricity production from nuclear energy in 2018. Russia, South Korea and France provide 17.9%, 23.7% and 71.7% of their electricity generation from nuclear energy, respectively. China, which has 48 nuclear power plants, has started the construction of 10 new nuclear power plants to meet the electricity demand to be realized in the coming years (IAEA, 2020).

Table 1: The Number of Nuclear Power Plants in Operation and Under Construction in the World and the Share of Nuclear Energy in Electricity Generation of Countries (IAEA, 2020)

Country	Number of Nuclear Power Plants in Operation *	Number of Power Plants Under Construction *	Share of Nuclear Energy in Electricity Generation (%) **
USA	96	2	19.3%
France	58	1	71.7%
China	48	10	4.2%

Russia	38	4	17.9%
Japan	37	2	6.2%
South Korea	24	4	23.7%
India	22	7	3.1%
Canada	19	-	14.9%
United Kingdom	15	1	17.7%
Ukraine	15	2	53.0%
Belgium	7	-	39.0%
Spain	7	-	20.4%
Sweedeen	7	-	40.3%
Germany	6	-	11.7%
Czechia	6	-	34.5%
Pakistan	5	2	6.8%
Switzerland	4	-	37.7%
Finland	4	1	32.4%
Hungary	4	-	50.6%
Slovakia	4	2	55.0%
Argentina	3	1	4.7%
Brazil	2	1	2.8%
Bulgaria	2	-	34.7%
Mexico	2	-	5.3%
Romania	2	-	17.2%
South Africa	2	-	4.7%
Armenia	1	-	25.6%
Iran	1	1	2.1%
Netherlands	1	-	3.0%
Slovenia	1	-	35.9%
UAE	-	4	-
Bangladesh	-	2	-
Belarus	-	2	-
Turkey	-	1	-
TOTAL	447	52	

*IAEA as of January 16, 2020

**IAEA 2018 data

In the Electricity Energy Market and Supply Security Strategy Document, which was prepared to ensure a competitive electricity market and energy supply security, the goal of including nuclear energy in the supply portfolio is also included in order to increase fuel diversity. (Republic of Turkey Ministry of Energy and Natural Resources, 2017).

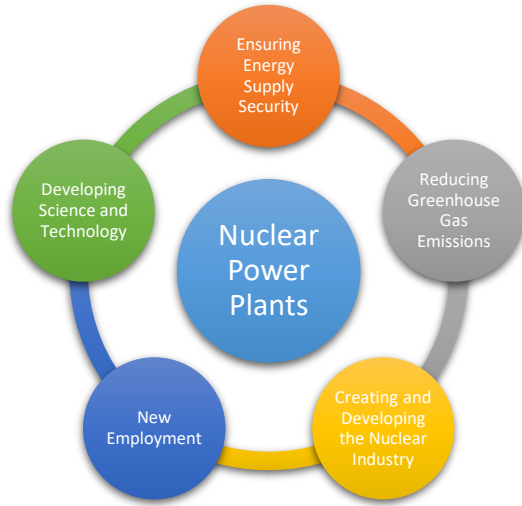


Figure 2: The Importance of Nuclear Power Plants for Turkey (Republic of Turkey Ministry of Energy and Natural Resources, 2017)

As of the end of 2016, the share of natural gas in electricity generation is 32.1% and the share of coal is 33.7%. As stated in the Electric Energy Market and Supply Security Strategy Document published by the Supreme Planning Council in 2009, our country plans to reduce the share of natural gas in electricity production to less than 30% in 2023 and accepts nuclear energy as an obligation, not an option, in terms of reducing energy imports in ensuring our energy supply security.

The uranium exploration studies carried out in many fields in our country could not be carried out with sufficient sensitivity due to various reasons. The grade and apparent amount of uranium deposits found as a result of the searches made so far are given in Table 2.

Table 2: Turkey Uranium Deposits (General Directorate of Mineral Research and Exploration, 2017)

Region	Grade(%)	U ₃ O ₈ ton
Salihli-Köprübaşı	0.04-0.07	3.487
Uşak-Eşme-Fakılı	0.05	490
Aydın-Söke-Küçükçavdar	0.04	208
Aydın-Söke-Demirtepe	0.08	1.729
Yozgat-Sorgun	0.1	6.700
		Total: 12.614 tons U ₃ O ₈

Our uranium ores found by Mineral Research and Exploration (MTA) total approximately 12.614 tons of uranium. There are three types of ores in Salihli Köprübaşı. These; Kasar, Ecinnitaş and Taşharman. In 1980, 1,300 kg of yellow cake was produced from 1,000 tons of uranium ore with 0.05% U_3O_8 grade in Kasar and natural uranium fuel pellets were made from this yellow cake in MTA laboratories. After 1980, pilot nuclear fuel production studies continued at TAEK Çekmece Nuclear Research and Training Center. Since the found areas were transferred to Etibank, MTA bought the land again in April 2010 and started work in Köprübaşı.

Powder metallurgy procedures for the production of uranium metal oxide, carbide and nitride fuels are very old. These procedures have been successfully used industrially for the production of UO_2 , (U, Pu) O_2 , (U, Pu)C pellets. Although the production of UO_2 pellets using powder metallurgy is a well-known procedure, some of the problems encountered are listed below:

- Processing of large quantities of highly toxic radioactive powders,
- Presence of many mechanical steps in fuel fabrication,
- Difficulties in remote control of the process,
- Problems caused by the doses exposed as a result of ^{241}Am accumulation and aging of the production facility.

Considering all these, problems have arisen in the fabrication of nuclear fuels using conventional powder metallurgy processes due to cost increases and technological difficulties. In the early 60's, studies were carried out to develop solution-based fuel fabrication processes in the production of Th- ^{233}U fuels. Coated fuel microspheres (UC₂, UThC₂) were produced using solution / sol based procedures called the sol-gel process (Vaidya, 2002).

The sol-gel method is based on the conversion of a sol (even a true solution) into a hydroxide gel by dispersing it into an organic solvent. Many gel preparation methods are used in the synthesis of ceramics, catalysts and inorganic sorbents. The common point of all these methods is that they consist of suitable process components to bind colloidal particles together to form the gel structure. These processes are commonly referred to as "sol-gel" processes and their chemistry is quite complex. Gels are generally hydrated metal oxides. The gelation process is divided into two as external gelation or internal gelation. In various sol-gel methods developed, droplets of organic polymer solutions or sols are gelled with ammonia. This process usually takes place by mass transfer from ammonia solution or vapor (Tel, 1997).

The sol-gel process has been used in nuclear fuel fabrication since the 1960s. Some applications are given below:

- Synthesis of ultra fine particles or microspheres for liquid fuels,
- Synthesis of sol-gel particles for vibratory compression,
- Synthesis of compressible and sintered sol-gel particles for pellet type fuel,
- Production of coated fuel core microspheres for HTGRs,
- Creation of microspheres for sphere-pack fuel.

In the internal gelation sol-gel process, the cooled feed solution containing metal nitrate, hexamethylenetetramine (HMTA) and urea is heated, releases ammonia, and a hydrated gel is formed. The gels formed by the internal gelation technique become metal oxides by drying and heating processes. The microspheres obtained show homogeneous size distribution and perfect sphericity. Unlike external gelation, the internal gelation method enables spheres with smooth surfaces without cracking. Also, since solid gels are formed from aqueous solutions during internal gelation, the final products exhibit a homogeneous distribution of dissolved elements in the feed solution. Such homogeneous products are desired for mixed oxide fuel pellets that can be pressed from microspheres with low compressive strength (Katalenich, 2017).

In the study, it is aimed to obtain high homogeneity and density $\text{UO}_3 \cdot \text{NH}_3 \cdot \text{H}_2\text{O}$ spheres by sol-gel technique with starting chemicals $\text{UO}_2(\text{NO}_3)_2 \cdot 6\text{H}_2\text{O}$, $\text{CO}(\text{NH}_2)_2$ and $\text{C}_6\text{H}_{12}\text{N}_4$. After aging and drying, characterization studies were carried out.

2. EXPERIMENTAL

2.1 General Process

In the study, firstly the nitrate solution of uranium was prepared in the production of $\text{UO}_3 \cdot \text{NH}_3 \cdot \text{H}_2\text{O}$ spheres based on the sol-gel method of nuclear fuel production. $\text{UO}_3 \cdot \text{NH}_3 \cdot \text{H}_2\text{O}$ spheres were obtained by starting from the nitrate solution and going through the stages shown in the process flow chart given in Figure 3. The characterization studies of microspheres were performed by TG/DTA and BET surface area and porosity analysis.

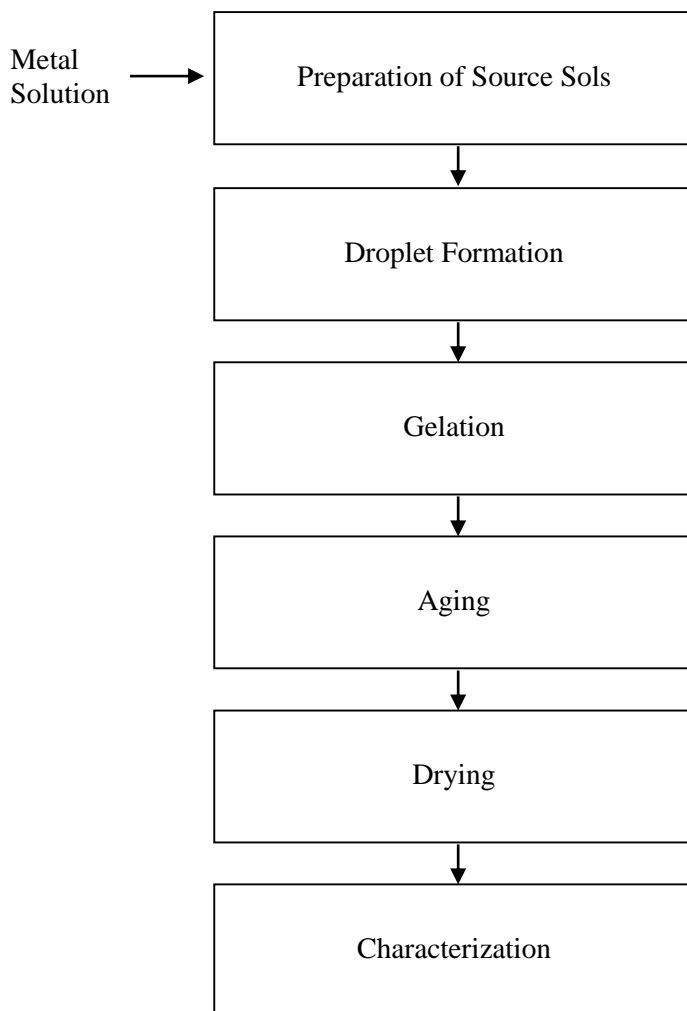
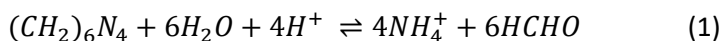


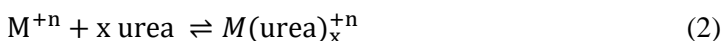
Figure 3: Flow Chart of the Study

2.2 Preparation of Sols

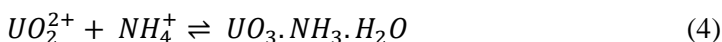
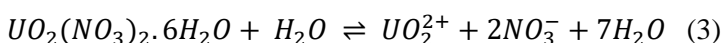
The synthesis of gel beads is based on the formation of cold sol droplets in the organic disperser and then the decomposition of the HMTA in the structure to release ammonia when heated. This process is commonly referred to as the "internal gelation process" (Haas et al., 1983). The release of homogeneous ammonia during the gelation reaction allows uniform precipitation of metal oxides without deterioration due to shell formation or tensile forces. The hydrolytic decomposition reaction of HMTA in acidic medium is shown in Equation 1.



Hydrogen ions are neutralized by the degradation of HMTA and thus, with the increase in the pH of the aqueous solution, hydrous metal oxides can precipitate or metal oxide sols can turn into gel form. The kinetics and direction of the reaction regarding the decomposition of HMTA given in Equation 1 depends on the temperature. The feed solutions to be used for the synthesis of the beads by the internal gelation process must have a long gelation time at low temperature to prevent premature gelation in the injection system, and a short gelation time at high temperatures to quickly harden the gel beads. For many metals, gelation at low temperatures can be delayed or prevented by adding urea to the complex (Equation 2).



The dissolution of uranyl nitrate hexahydrate in water and the precipitation reaction of the formed uranyl with ammonia are given in Equation 3 and Equation 4.



Ammonium diuranate (ADU), which precipitates by the reaction of uranyl ion with ammonia, is actually a mixture of ammonium uranate compounds. ADU with four different crystal structures was determined. These;

	<u>NH₃/U mol ratio</u>
6UO ₃ ·12H ₂ O	0
6UO ₃ ·2NH ₃ ·10H ₂ O	0.33
6UO ₃ ·3NH ₃ ·9H ₂ O	0.50
6UO ₃ ·4NH ₃ ·8H ₂ O	0.66

2.3 Droplet Formation and Gelation

The droplet forming system is important in obtaining the desired diameter and uniform spheres. A 1 mL injector tip was used to create droplets and the prepared sols were sent to the spiral gelation column by a peristaltic pump. In gelation, choosing an organic solvent with a high surface tension and a small density difference with sol is a key factor. Therefore, CCl₄ was chosen as the gelling medium. The mechanism shown in Figure 4 consists of jacketed heater, condenser, cooled circulation water

bath, peristaltic pumps, spiral gelation column and connections. The prepared sols were given to the gelation system and oxide gel spheres were obtained.

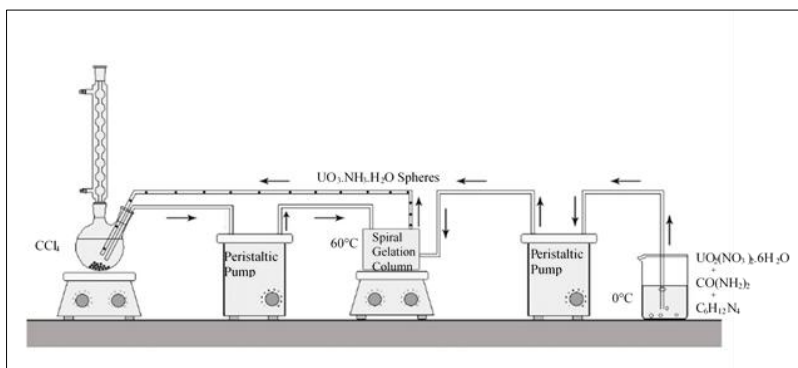


Figure 4: Internal Gelation Sol-Gel Experiment Setup

2.4 Aging and Drying

The purpose of the aging process is to prevent the deterioration of spheres during drying. During aging, the spheres shrink a little. It is estimated that there is grain growth at this time. Therefore, uranium oxide gel spheres were kept in CCl_4 boiling under reflux for 2 hours. The drying process was carried out in the oven at $60\text{ }^\circ\text{C}$ for 48 hours and then in the vacuum oven at $60\text{ }^\circ\text{C}$ for 72 hours.

2.5 Characterization Studies

2.5.1 Thermal Analysis

TG/DTA analysis of $\text{UO}_3.\text{NH}_3.\text{H}_2\text{O}$ microspheres were carried out in two different atmospheres as N_2 and O_2 between room temperature and $1300\text{ }^\circ\text{C}$. The spheres were analyzed at a gas flow rate of 20 mL/min for N_2 and 200 mL/min for O_2 , at a heating rate of $10\text{ }^\circ\text{C/min}$. Alumina silicate crucible was used during the analysis. Mass loss versus temperature and potential difference values were recorded.

2.5.2 BET Surface Area and BJH Porosity Analysis

Surface area and porosity analysis of $\text{UO}_3.\text{NH}_3.\text{H}_2\text{O}$ spheres were performed by Micromeritics ASAP 2020 surface area and porosity analyzer. Firstly, the spheres were kept under vacuum at $100\text{ }^\circ\text{C}$ and atmospheric gases and water vapor in the pores were removed. The BET surface area and porosity of the spheres were measured by nitrogen gas adsorption method at liquid nitrogen temperature.

3. RESULTS AND DISCUSSION

3.1 Synthesis of $\text{UO}_3 \cdot \text{NH}_3 \cdot \text{H}_2\text{O}$ Microspheres

From Equation 1, Equation 2, Equation 3 and Equation 4, it has been calculated that 2 moles of urea and 1.5 moles of HMTA are required for 1 mol of uranium. $\text{UO}_3 \cdot \text{NH}_3 \cdot \text{H}_2\text{O}$ source sol was prepared with $\text{UO}_2(\text{NO}_3)_2 \cdot 6\text{H}_2\text{O}$ at 1 M metal concentration. Sol solution was prepared by dissolving 5.0283 g $\text{UO}_2(\text{NO}_3)_2 \cdot 6\text{H}_2\text{O}$, 1.2026 g $\text{CO}(\text{NH}_2)_2$ and 2.0998 g $\text{C}_6\text{H}_{12}\text{N}_4$ in 10 mL 0 °C deionized water.

The gelation of the prepared sol solution was carried out by means of the experimental setup (Figure 4). The system consists of a jacketed heater, condenser, cooled circulation water bath, peristaltic pumps, spiral gelation column and connections. There was ~1 L of boiling CCl_4 in the collection vessel under the condenser. Due to the low vapor pressure, CCl_4 was heated under the condenser, thus the loss of CCl_4 by evaporation was prevented. CCl_4 taken from the collection vessel by peristaltic pump passes through the spiral gelation column and was fed back to the collection vessel. The prepared source sol was sent to the spiral gelation column using a peristaltic pump. Due to surface tension forces, the sol solution injected into CCl_4 took the spherical form. The column was kept under a constant temperature of 60 °C. While the spheres formed at the injection tip moved through the column, they reacted with ammonia released by the hydrolytic decomposition of HMTA due to the temperature and gelled in the form of $\text{UO}_3 \cdot \text{NH}_3 \cdot \text{H}_2\text{O}$. The spherical gels moved on along the column and were collected in the collection vessel.

3.2 Aging and Drying

After precipitation, the gel spheres were allowed to age for 2 hours in boiling CCl_4 . Structural changes that occur during aging are of great importance during drying. The capillary pressure that occurs during drying increases in direct proportion to the interfacial area of the gel structure. If this interface area can be reduced by the grain growth process, the capillary pressure force generated during drying becomes less. With aging, harder and more durable gel structures can be formed.

The synthesized spheres (Figure 5) were dried in the oven at 60 °C for 48 hours and in the vacuum oven at 60 °C for 72 hours.



Figure 5: Synthesized $\text{UO}_3 \cdot \text{NH}_3 \cdot \text{H}_2\text{O}$ Microspheres

3.3 Characterization Studies

3.3.1 Thermal Analysis

TG/DTA analysis of synthesized $\text{UO}_3 \cdot \text{NH}_3 \cdot \text{H}_2\text{O}$ spheres were carried out in N_2 and O_2 atmospheres. TG/DTA curve of $\text{UO}_3 \cdot \text{NH}_3 \cdot \text{H}_2\text{O}$ microspheres in N_2 atmosphere is shown in Figure 6. The hump seen around 100°C in the TGA curve shows the removal of water and moisture in the structure. The corresponding endothermic peak is also seen in the DTA curve. With the decomposition of ammonium nitrate (NH_4NO_3), urea and HMTA and the removal of the crystal water in the structure, the mass loss reached $\sim 70\%$ around $\sim 225^\circ\text{C}$. It is thought that the endothermic peak around 600°C indicates the conversion of UO_3 to U_3O_8 . The endothermic peak seen around $\sim 1175^\circ\text{C}$ is attributed to the beginning of sintering.

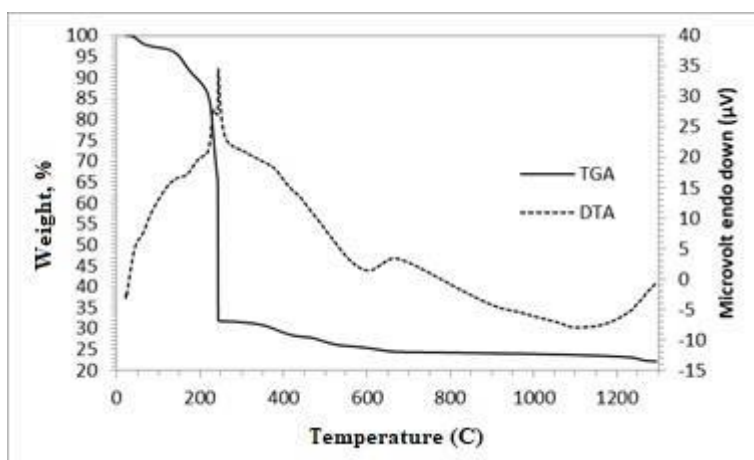


Figure 6: TG/DTA Curve of $\text{UO}_3 \cdot \text{NH}_3 \cdot \text{H}_2\text{O}$ Spheres in N_2 Atmosphere

TG/DTA curve of $\text{UO}_3 \cdot \text{NH}_3 \cdot \text{H}_2\text{O}$ microspheres in O_2 atmosphere is shown in Figure 7. The hump seen around 100°C in the TGA curve shows

the removal of water and moisture in the structure. With the decomposition of ammonium nitrate (NH_4NO_3), urea and HMTA and the removal of the crystal water in the structure, the mass loss reached $\sim 50\%$ around $\sim 225^\circ\text{C}$. On the other hand, the endothermic peak showing the conversion of UO_3 to U_3O_8 could not be observed in the DTA curve. The endothermic peak seen around $\sim 1175^\circ\text{C}$ is attributed to the beginning of sintering.

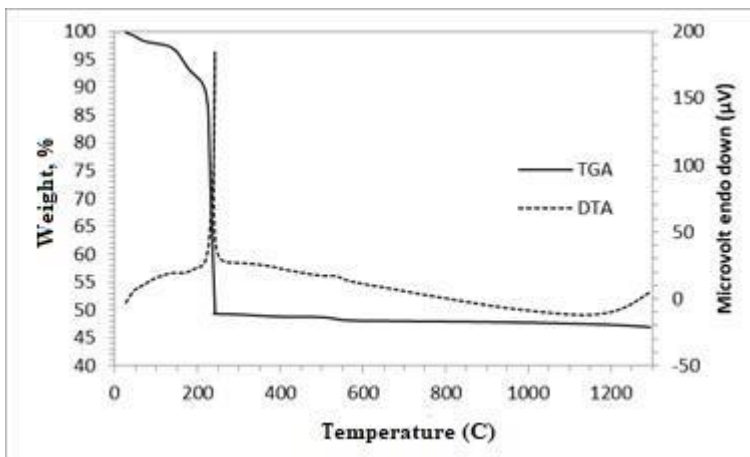


Figure 7: TG/DTA Curve of $\text{UO}_3\cdot\text{NH}_3\cdot\text{H}_2\text{O}$ Spheres in O_2 Atmosphere

3.3.2 BET Surface Area and BJH Porosity Analysis

The BET surface area and BJH porosity analysis of $\text{UO}_3\cdot\text{NH}_3\cdot\text{H}_2\text{O}$ spheres dried at 60°C were performed by nitrogen gas adsorption at liquid nitrogen temperature. BET surface area of the $\text{UO}_3\cdot\text{NH}_3\cdot\text{H}_2\text{O}$ spheres was found to be $0.89\text{ m}^2/\text{g}$. The total pore volume and the average pore diameter were obtained as $0.0040\text{ cm}^3/\text{g}$ and 44.4 nm , respectively.

4. CONCLUSION

In the study, it was aimed to obtain high homogeneity and density $\text{UO}_3\cdot\text{NH}_3\cdot\text{H}_2\text{O}$ spheres by using sol-gel technique with starting chemicals $\text{UO}_2(\text{NO}_3)_2\cdot 6\text{H}_2\text{O}$, $\text{CO}(\text{NH}_2)_2$ and $\text{C}_6\text{H}_{12}\text{N}_4$. Firstly, a nitrate solution of uranium with a metal concentration of 1 M was prepared in order to obtain durable sols suitable for gelation by utilizing the gelling property of uranium. Urea was added to this solution as a gelation retarding agent and HMTA as a source of ammonia, and the sol solution was prepared. The prepared sol solution was gelled in the form of spheres by using the injection tip and spiral gelation column. For this purpose, the assembly consisting of peristaltic pump, injection tip, spiral gelation column and connections was designed and manufactured.

The droplet forming system is important in obtaining the desired diameter and uniform spheres. A 1 mL injector needle was used to create

droplets and the prepared sol was sent to the spiral gelation column using a peristaltic pump. Due to the surface tension forces, the sol solution injected into CCl_4 gelled in spherical form. The column was kept under a constant temperature of $60\text{ }^\circ\text{C}$. While the spheres formed at the injection tip moved through the column, they reacted with the ammonia released by the hydrolytic decomposition of HMTA due to the heat and gelled in the form of $\text{UO}_3\cdot\text{NH}_3\cdot\text{H}_2\text{O}$. The spherical gels were collected in the collection vessel by moving along the column.

After aging and drying, characterization studies of gel spheres were performed by TG/DTA, BET surface area and BJH porosity analyzes. It is thought that water and moisture in the structure up to a temperature of $100\text{ }^\circ\text{C}$ and urea, unreacted HMTA and crystal water up to a temperature of $\sim 225\text{ }^\circ\text{C}$ were removed from the structure. It is thought that the endothermic peak seen around $600\text{ }^\circ\text{C}$ in $\text{UO}_3\cdot\text{NH}_3\cdot\text{H}_2\text{O}$ spheres heated in N_2 atmosphere indicates the conversion of UO_3 to U_3O_8 . This peak was not observed in $\text{UO}_3\cdot\text{NH}_3\cdot\text{H}_2\text{O}$ spheres heated in O_2 atmosphere. The endothermic peak seen around $\sim 1175\text{ }^\circ\text{C}$ in both atmospheres was attributed to the beginning of sintering.

In our country, the construction of nuclear reactors has started in line with the approved agreements. As a result of the searches made by MTA, significant uranium reserves were found in our country and the searches are still ongoing. Undoubtedly, our country is obliged to carry out studies on UO_2 fuel production and to provide knowledge within the framework of the evaluation of nuclear fuel resources.

In the present study, $\text{UO}_3\cdot\text{NH}_3\cdot\text{H}_2\text{O}$ microspheres were successfully obtained using the internal sol-gel process. With further studies, it is planned to convert $\text{UO}_3\cdot\text{NH}_3\cdot\text{H}_2\text{O}$ spheres to UO_2 form by H_2 reduction.

ACKNOWLEDGEMENT

This study was supported by Ege University Scientific Research Projects Coordinaton. We would like to thank Ege University for the financial support of this project (Project No. BAP 18 NBE 002).

REFERENCES


- General Directorate of Mineral Research and Exploration, Feasibility Studies Department. (2017). *Dünyada ve Türkiye’de Uranyum ve Toryum* (Mine Series: 3). Retrieved from <https://www.mta.gov.tr/v3.0/sayfalar/bilgi-merkezi/maden-serisi/Uranyum-Toryum.pdf>
- Haas, P.A., Pitt, W.W., Robinson, S.M. and Ryon, A.D. (1983). Preparation of Metal Oxide Gel Spheres with Hexamethylenetetraamine as an Ammonia Donor. *Industrial & Engineering Chemistry Product Research and Development*, 22, 461-466. doi: 10.1021/i300011a015
- International Atomic Energy Agency (IAEA). (2020). Power Reactor Information System - Nuclear Share of Electricity Generation in 2018. Retrieved January 20, 2020 from <https://pris.iaea.org/PRIS/WorldStatistics/NuclearShareofElectricityGeneration.aspx>
- International Atomic Energy Agency (IAEA). (2019). Preliminary Nuclear Power Facts and Figures for 2019. Retrieved May 20, 2020 from <https://www.iaea.org/newscenter/news/preliminary-nuclear-power-facts-and-figures-for-2019>
- Katalenich, J. A. (2017). Production of Cerium Dioxide Microspheres by an Internal Gelation Sol-Gel Method, *Journal of Sol-Gel Science and Technology*, 82, 654-663.
- Republic of Turkey Ministry of Energy and Natural Resource, Strategy Development Department. (2017). *Dünya ve Türkiye Enerji ve Tabii Kaynaklar Görünümü* (No. 15).
- Tel, H. (1997). *Sol-jel Geçışı ile ThO_2 -(%0-40) UO_3 Kaynak Mikroküreciklerinin Elde Edilmesi, $(Th,U)O_2$ Peletlerinin Hazırlanması ve Üretim Koşullarının İncelenmesi*. Doktora Tezi, Ege Üniversitesi, Fen Bilimleri Enstitüsü, Nükleer Bilimler Anabilim Dalı, Bornova-İzmir.
- Vaidya, V.N. (2002). Sol-gel Process For Ceramic Nuclear Fuels. Retrieved November 4, 2020 from: <http://barc.gov.in/publications/nl/2002/200203-01.pdf>
- World Energy 2017-2050: Annual Report*. (2017). Retrieved November 4, 2020 from <https://seekingalpha.com/article/4083393-world-energy2017minus-2050-annual-report>

CHAPTER V


ON KIROV-TYPE GENERALIZATION OF GAUSS-WEIERSTRASS OPERATORS

Başar Yılmaz¹ & Gümrah Uysal²

¹(Dr), Kirikkale University, e-mail: basaryilmaz77@yahoo.com

 ORCID 0000-0003-3937-992X

²(Dr), Karabük University, e-mail: fgumrahuyisal@gmail.com

 ORCID 0000-0001-7747-1706

INTRODUCTION

The studies concerning approximation by linear positive operators became strongly ingrained part of theory of approximation. In the current article, we will handle the sequences of integral operators, known in the literature as Gauss-Weierstrass operators, from another perspective. The classical form of these operators is described by the following formula:

$$(W_n f)(x) := \sqrt{\frac{n}{4\pi}} \int_{-\infty}^{\infty} f(x+t) e^{-\frac{nt^2}{4}} dt, \quad x \in \mathbb{R}, \quad n \in \mathbb{N}, \quad (1.1)$$

where the function f is enriched with some properties in order to obtain finite integral value.

The operators of type (1.1) have been investigated in several works, such as (see [1-5]). Here, for extensive information, we mention the monograph [6] and the references therein.

On the other hand, Kirov [7] defined the Bernstein polynomials $B_{n,r}$ for r -times differentiable functions $f \in C^r([0,1])$. In the same paper he showed that $B_{n,r}$ have better approximation properties than classical Bernstein polynomials B_n .

The following operator whose analogous modification was defined in [8] is the Kirov-type modification of the Gauss-Weierstrass operators:

$$(W_{n,r} f)(x) := \sqrt{\frac{n}{4\pi}} \int_{-\infty}^{\infty} \sum_{j=0}^r \frac{f(x+t)}{j!} (t)^j e^{-\frac{nt^2}{4}} dt, \quad (1.2)$$

where $x \in \mathbb{R}, n \in \mathbb{N}, r \in \mathbb{N}_0$ $\mathbb{N}_0 := \mathbb{N} \cup \{0\}$ and $f: \mathbb{R} \rightarrow \mathbb{R}$, r -times differentiable functions. Here, $W_{n,0}(f)$ denotes $W_n(f)$.

Throughout this paper which is a continuation of [8], our aim is to obtain additional approximation properties of the operators (1.2) and in order to achieve this, we refer a new space containing all real valued functions whose exponential transformation is Lebesgue integrable with p -th power over \mathbb{R} and call it the exponential weighted space. We examine the generalized Gauss-Weierstrass operators $W_{n,r}$ for functions f belonging to the exponential weighted spaces $L_q^p(\mathbb{R})$ and $L_q^{p,r}(\mathbb{R})$ whose definitions are given bellow. Using appropriate modulus of continuity defined on exponential weighted spaces, we obtain the order of convergence of the operators of type (1.2), the Voronovskaya-type theorem and quantitative results for these operators.

Following [1], let $q > 0$ be a fixed number and

$$\lambda_q(x) := e^{-qx^2}, x \in \mathbb{R}. \quad (1.3)$$

For a fixed $1 \leq p \leq \infty$ and $q > 0$ we denote by L_q^p the set of all real-valued functions f defined on \mathbb{R} for which the p -th power of $\lambda_q f$ is Lebesgue-integrable on \mathbb{R} if $1 \leq p < \infty$ and $\lambda_q f$ is uniformly continuous and bounded on \mathbb{R} if $p = \infty$. Let the norm in L_q^p be given by the formula:

$$\|f\|_{p,q} = \|f(\cdot)\|_{p,q} := \begin{cases} \left(\int_{-\infty}^{\infty} |\lambda_q(x) f(x)|^p dx \right)^{\frac{1}{p}}, & \text{if } 1 \leq p < \infty, \\ \sup_{x \in \mathbb{R}} \lambda_q(x) |f(x)|, & \text{if } p = \infty. \end{cases} \quad (1.4)$$

Also, let $r \in \mathbb{N}_0$ and $L_q^{p,r} = L_q^{p,r}(\mathbb{R})$ be the class of all r -times differentiable functions $f \in L_q^p$ with derivatives $f^{(k)} \in L_q^p$, $1 \leq k \leq r$. The norm in $L_q^{p,r}$ is given by (1.4). ($L_q^{p,0} \equiv L_q^p$) The spaces L_q^p and $L_q^{p,r}$ are called exponential weighted spaces (see [9]).

For $f \in L_q^p$ we define the modulus of smoothness (see [10])

$$\omega_k(f, L_q^p; t) := \sup_{|h| \leq t} \|\Delta_h^k f(\cdot)\|_{p,q} \text{ for } t \geq 0. \quad (1.5)$$

Here,

$$\Delta_h^1 f(x) = f(x+h) - f(x)$$

and

$$\Delta_h^2 f(x) = f(x+h) - f(x-h) - 2f(x) \quad x, h \in \mathbb{R}. \quad (1.6)$$

From (1.4)-(1.6) for $f \in L_q^p$ the following conditions are satisfied (see [1, 11]) for $\lambda, t \geq 0$ and $k = 1, 2$:

$$i) \lim_{t \rightarrow 0} \omega_k(f, L_q^p; t) = 0 \quad (1.7)$$

$$ii) \omega_k(f, L_q^p; t_1) \leq \omega_k(f, L_q^p; t_2) \quad \text{if } 0 \leq t_1 < t_2 \quad (1.8)$$

$$iii) \omega_k(f, L_q^p; \lambda t) \leq (1 + \lambda)^k e^{q(t\lambda)^2} \omega_k(f, L_q^p; t) \quad (1.9)$$

AUXILIARY RESULTS

In this part, we shall give some fundamental properties of the Generalized Gauss-Weierstrass integral operators $W_{n,r}$ in the spaces $L_{2q}^p(\mathbb{R})$. Firstly, we give the following two lemmas. It is easy to verify these two lemmas.

Lemma 1. *The equality*

$$I_r := \sqrt{\frac{n}{4\pi}} \int_0^\infty t^r e^{-\frac{nt^2}{4}} dt = \begin{cases} 1 & \text{if } r = 0, \\ 2^k (2k-1)!! \left(\frac{1}{n}\right)^k & \text{if } r = 2k \geq 2, \\ \frac{2^{2k+1} k!}{n^{\frac{k+1}{2}} \sqrt{\pi}} & \text{if } r = 2k + 1, \end{cases}$$

where $(2k-1)!! = 1.3.5 \dots (2k-1)$ for $k \in \mathbb{N}$, holds for every $r \in \mathbb{N}_0$ and $n > 0$ (see [8]).

Lemma 2. *Let $e_0(x) = 1$, $e_1(x) = x$ and $\varphi_x(t) = t - x$ for $x, t \in \mathbb{R}$ and $k \in \mathbb{N}$. Then,*

$$W_n(e_i; x) = e_i(x) \quad \text{for } x \in \mathbb{R} \text{ and } n \in \mathbb{N}. \quad i = 0, 1 \quad (2.2)$$

$$W_n(\varphi_x^k(t); x) = \frac{((-1)^{k+1} \Gamma(\frac{k+1}{2}))}{2\sqrt{\pi} n^{\frac{k}{2}}} \quad (2.3)$$

$$W_n(|\varphi_x(t)| \exp(q|\varphi_x(t)|^2); x) = \sqrt{\frac{n}{\pi}} \frac{\Gamma(\frac{k+1}{2})}{(n-q)^{\frac{k+1}{2}}}, \quad n > q + 1 \quad (2.4)$$

where Γ is gamma function. Now using Lemma 1, we prove main lemma.

Lemma 3. Let $f \in L_q^p(\mathbb{R})$ with fixed $1 \leq p \leq \infty, q > 0$, then for $n > 8q + 1$, we have

$$\|W_{n,r}f\|_{p,2q} \leq \sum_{j=0}^r \|f^{(j)}\|_{p,q} I_r. \quad (2.6)$$

The formula (1.2) and inequality (2.5) Show that the integral $W_{n,r}(f)$ for fixed $r \in \mathbb{N}_0$ and $n > 0$ is a linear positive operator from $L_q^p(\mathbb{R})$ into $L_{2q}^p(\mathbb{R})$.

Proof. If $r \in \mathbb{N}_0$ and $1 \leq p < \infty$, then, by (1.2), using Minkowski inequality and (2.1), we obtain for $L_q^{p,r}(\mathbb{R})$ and $n > 8q + 1$

$$\begin{aligned} \|W_{n,r}f\|_{p,2q} &= \sum_{j=0}^r \frac{1}{j!} \left(\int_{-\infty}^{\infty} |e^{-2qx^2} (W_{n,r}f)(x)|^p dx \right)^{\frac{1}{p}} \\ &\leq \sum_{j=0}^r \frac{1}{j!} \left(\int_{-\infty}^{\infty} e^{-2qx^2} \left| \sqrt{\frac{n}{4\pi}} \int_{-\infty}^{\infty} \sum_{j=0}^r f(x+t) (t)^j e^{-\frac{nt^2}{4}} dt \right|^p dx \right)^{\frac{1}{p}} \\ &\leq \sum_{j=0}^r \frac{1}{j!} \sqrt{\frac{n}{4\pi}} \int_{-\infty}^{\infty} |t|^j e^{-\frac{nt^2}{4}} dt \left(\int_{-\infty}^{\infty} |e^{-2q(u-t)^2} f^{(j)}(u)|^p du \right)^{\frac{1}{p}} dt \\ &= \sum_{j=0}^r \frac{1}{j!} \sqrt{\frac{n}{4\pi}} \int_{-\infty}^{\infty} |t|^j e^{-\frac{nt^2}{4}} dt \left(\int_{-\infty}^{\infty} e^{-2u^2p+2qt^2p} |f^{(j)}(u)|^p du \right)^{\frac{1}{p}} \\ &= \sum_{j=0}^r \frac{2}{j!} \|f^{(j)}\|_{p,q} \int_0^{\infty} t^j e^{-t^2(\frac{n}{4}-2q)} dt = \sum_{j=0}^r \frac{2}{j!} \|f^{(j)}\|_{p,q} I_r, \end{aligned}$$

where I_r is given by (2.1).

APPROXIMATION RESULTS

Theorem 1. If $f \in L_q^{p,r}(\mathbb{R})$ with fixed $1 \leq p \leq \infty, q > 0, r \in \mathbb{N}$ and $n > 8q + 1$. Then, we have

$$\|W_{n,r}(f) - f\|_{p,2q} \leq H(r)n^{-\frac{r}{2}}\omega_1\left(f^{(r)}, L_q^p; \frac{1}{\sqrt{n}}\right). \quad (3.1)$$

$H(r)$ is a positive constant depending only on r and $\omega_1(f^{(r)}, L_q^p; \cdot)$ is defined by (1.5).

Proof. We can write the following Taylor-type theorem with $f \in L_q^{p,r}(\mathbb{R})$ and $x, t \in \mathbb{R}$

$$f(x) = \sum_{j=0}^r \frac{f^{(j)}(t)}{j!} (x-t)^j + \frac{(x-t)^j}{(r-1)!} S_r(t, x),$$

where

$$S_r(t, x) := \int_0^1 (1-u)^{r-1} [f^{(r)}(t+u(x-t)) - f^{(r)}(t)] du. \quad (3.2)$$

By (3.2), (3.3) and (1.2) it follows that

$$\begin{aligned} W_{n,r}(f; x) - f(x) &= \frac{(-1)^{r+1}}{(r-1)!} W_n((t-x)^r S_r(t, x); x) \\ &= \sqrt{\frac{n}{4\pi}} \frac{(-1)^{r+1}}{(r-1)!} \int_{-\infty}^{\infty} \left(t^r \int_0^1 (1-u)^{r-1} \Delta_{-ut}^1 f^{(r)}(x+t) du \right) e^{-\frac{nt^2}{4}} dt \quad (3.4) \end{aligned}$$

for $x \in \mathbb{R}$ and $n > 8q + 1$.

i) Let $1 \leq p < \infty$, if we use the Minkowski inequality and (1.4), we can find (3.4):

$$\begin{aligned} & \|W_{n,r}(f) - f\|_{p,2q} \\ &= \frac{\sqrt{n}}{\sqrt{4\pi}(r-1)!} \times \\ & \left(\int_{-\infty}^{\infty} \left| e^{-2qx^2} \int_{-\infty}^{\infty} t^r e^{-\frac{nt^2}{4}} \left(\int_0^1 (1-u)^{r-1} \Delta_{-ut}^1 f^{(r)}(x+t) du \right) dt \right|^p dx \right)^{\frac{1}{p}} \\ & \leq \frac{\sqrt{n}}{\sqrt{4\pi}(r-1)!} \times \\ & \left(\int_{-\infty}^{\infty} |t|^r e^{-t^2(\frac{n}{4}-2q)} \left(\int_0^1 (1-u)^{r-1} \|\Delta_{-ut}^1 f^{(r)}(\cdot)\|_{p,q} du \right) dt \right) \end{aligned}$$

$$\begin{aligned}
&\leq \frac{\sqrt{n}}{\sqrt{4\pi}(r-1)!} \times \\
&\left(\int_{-\infty}^{\infty} |t|^r e^{-t^2(\frac{n}{4}-2q)} \left(\int_0^1 (1-u)^{r-1} \omega_1(f^{(r)}, L_q^p; u|t|) du \right) dt \right) \\
&\leq \frac{\sqrt{n}}{\sqrt{4\pi}(r-1)!} \int_{-\infty}^{\infty} |t|^r e^{-t^2(\frac{n}{4}-2q)} \omega_1(f^{(r)}, L_q^p; |t|) dt
\end{aligned}$$

by using (1.9)

$$\begin{aligned}
&\leq \frac{1}{r!} \omega_1\left(f^{(r)}, L_q^p; \frac{1}{\sqrt{n}}\right) \sqrt{\frac{n}{\pi}} \int_0^{\infty} t^r (1 + \sqrt{nt}) e^{-t^2(\frac{n}{4}-2q)} dt \\
&= \frac{1}{r!} (I_r + \sqrt{n} I_{r+1}) \omega_1\left(f^{(r)}, L_q^p; \frac{1}{\sqrt{n}}\right) \\
&= H(r) n^{-\frac{r}{2}} \omega_1\left(f^{(r)}, L_q^p; \frac{1}{\sqrt{n}}\right) \text{ for all } n > 0,
\end{aligned}$$

where I_r is given by (2.1). Using (2.1), we obtain (3.1) for $1 \leq p < \infty$.

ii) If $p = \infty$, then it follows from (1.5) and (1.9) that

$$\begin{aligned}
|\Delta_{-ut}^1 f^{(r)}(x+t)| &\leq \omega_1(f^{(r)}, L_q^\infty; u|t|) \\
&\leq \omega_1(f^{(r)}, L_q^\infty; |t|) \\
&\leq (1 + \sqrt{nt}) \omega_1\left(f^{(r)}, L_q^\infty; \frac{1}{\sqrt{n}}\right) \tag{3.5}
\end{aligned}$$

$n \in \mathbb{N}$ and for $0 \leq u \leq 1$. Using by (3.4) and (3.5), we obtain (3.1) for $p = \infty$.

Corollary 1. If $f \in L_q^{p,r}(\mathbb{R})$, $1 \leq p < \infty$, $q > 0$ and $r \in \mathbb{N}_0$ then

$$\lim_{n \rightarrow \infty} n^{-\frac{r}{2}} \|W_{n,r}(f) - f\|_{p,2q} = 0.$$

Similarly to the proof of Theorem 2 given in paper [8] and applying Corollary 1, we give the Voronovskaya-type theorem for $W_{n,r}$.

Theorem 2. Let $f \in L_q^{p,r}(\mathbb{R})$, $r \in \mathbb{N}_0$ and $q > 0$. Then,

$$W_{n,r}(f; x) - f(x)$$

$$= \frac{(-1)^r - 1}{(r+1)!} I_{r+1} f^{(r+1)}(x) + \frac{(-1)^r + 1}{(r+2)!} I_{r+2} f^{(r+2)}(x) + o\left(n^{-(1+\frac{r}{2})}\right)$$

as $n \rightarrow \infty$, at every $x \in \mathbb{R}$. Especially, if r is even number, then

$$\lim_{n \rightarrow \infty} \frac{(r+2)!}{I_{r+2}} [W_{n,r}(f; x) - f(x)] = 2(r+1)f^{(r+2)}(x) \text{ at every } x \in \mathbb{R}.$$

Theorem 3. Let $f \in L_q^{\infty, r+2}(\mathbb{R})$, $q > 0$ and even number $r \in \mathbb{N}_0$.

Then

$$\begin{aligned} & \left\| \frac{(r+2)!}{I_{r+2}} [W_{n,r}(f; x) - f(x)] - 2(r+1)f^{(r+2)} \right\|_{p,2q} \\ & \leq (r+4) \frac{\omega_1(f^{(r+2)}, L_q^\infty; \frac{1}{\sqrt{n}})}{(r+2)!} \sqrt{\frac{n}{\pi}} \left[\frac{\Gamma(\frac{r+3}{2})}{(n-q)^{\frac{r+3}{3}}} + \frac{\sqrt{n}\Gamma(\frac{r+4}{2})}{(n-q)^{\frac{r+4}{2}}} \right]. \end{aligned}$$

Proof. For $f \in L_q^{\infty, r+2}$ and $x, t \in \mathbb{R}$ the Taylor-type formula

$$f(x) = \sum_{j=0}^{r+2} \frac{f^{(j)}(t)}{j!} (x-t)^j + \frac{(x-t)^{r+2}}{(r+1)!} S_1(t, x), \quad (3.9)$$

where

$$S_1(t, x) := \int_0^1 (1-u)^{r+1} [f^{(r+2)}(t+u(x-t)) - f^{(r+2)}(t)] du. \quad (3.10)$$

Similarly, for $f^{(r+1)} \in L_q^{\infty, 1}$, we get

$$f^{(r+1)}(t) = f^{(r+1)}(x) + f^{(r+2)}(x)(t-x) + (t-x)S_2(t, x), \quad (3.11)$$

where

$$S_2(t, x) := \int_0^1 [f^{(r+2)}(t+u(x-t)) - f^{(r+2)}(x)] du. \quad (3.12)$$

By using (1.2) and (3.11), we can write the formula (3.9) as follows:

$$\begin{aligned}
f(x) &= \sum_{j=0}^r \frac{f^{(j)}(t)}{j!} (x-t)^j + \frac{(x-t)^{r+1}}{(r+1)!} f^{(r+1)}(x) \\
&\quad + \left(\frac{1}{(r+2)!} - \frac{1}{(r+1)!} \right) f^{(r+2)}(x) (x-t)^{r+2} \\
&\quad - \frac{(x-t)^{r+2}}{(r+1)!} S_2(t, x) \\
&\quad + \frac{(x-t)^{r+2}}{(r+2)!} [f^{(r+2)}(t) - f^{(r+2)}(x)] \\
&\quad + \frac{(x-t)^{r+2}}{(r+1)!} S_1(t, x).
\end{aligned}$$

Using operator W_n and (1.1)-(1.2) as fixed point $x \in \mathbb{R}$, we get from the last equality:

$$f(x) = W_{n,r}(f; x) - \frac{\Gamma\left(\frac{r+3}{2}\right) f^{(r+2)}(x)}{\sqrt{\pi n}^{\frac{r+2}{2}} (r+2)!} + K_1(x) + K_2(x) + K_3(x),$$

where

$$K_1(x) := \frac{1}{(r+1)!} W_n((t-x)^{r+2} S_2(t, x); x)$$

$$K_2(x) := \frac{1}{(r+2)!} W_n((t-x)^{r+2} [f^{(r+2)}(t) - f^{(r+2)}(x)]; x)$$

$$K_3(x) := \frac{1}{(r+1)!} W_n((t-x)^{r+2} S_1(t, x); x).$$

Therefore, we obtain

$$\begin{aligned}
&\left\| \sqrt{\pi n}^{\frac{r+2}{2}} (r+2)r! [W_{n,r}(f) - f] - \Gamma\left(\frac{r+3}{2}\right) f^{(r+2)}(x) \right\|_{\infty, 2q} \\
&\leq \sqrt{\pi n}^{\frac{r+2}{2}} (r+2)r! \times (\|K_1(x)\|_{\infty, 2q} + \|K_2(x)\|_{\infty, 2q} + \|K_3(x)\|_{\infty, 2q}).
\end{aligned}$$

From (3.12), there holds:

$$\begin{aligned}
\lambda_q(x) |K_1(x)| &\leq \frac{e^{-qx^2}}{(r+1)!} W_n(|t-x|^{r+2} S_2(t, x); x) \\
&\leq \frac{1}{(r+1)!} W_n(|t-x|^{r+2} \omega_1(f^{(r+2)}, L_q^\infty; |t-x|); x)
\end{aligned}$$

and from (1.9), it follows that

$$\begin{aligned}
&\leq \frac{1}{(r+1)!} W_n \left(|t-x|^{r+2} (1 \right. \\
&\quad \left. + |t-x|\sqrt{n}) e^{q|t-x|^2} \omega_1 \left(f^{(r+2)}, L_q^\infty; \frac{1}{\sqrt{n}} \right); x \right) \\
&= \frac{1}{(r+1)!} \omega_1 \left(f^{(r+2)}, L_q^\infty; \frac{1}{\sqrt{n}} \right) \times \left[\frac{W_n(|t-x|^{r+2} e^{q|t-x|^2}; x) + \right. \\
&\quad \left. \sqrt{n} W_n(|t-x|^{r+3} e^{q|t-x|^2}; x) \right]
\end{aligned}$$

and then by (2.4) we get

$$\|K_1(x)\|_{\infty, 2q} \leq \frac{\omega_1 \left(f^{(r+2)}, L_q^\infty; \frac{1}{\sqrt{n}} \right)}{(r+1)!} \sqrt{\frac{n}{\pi}} \left[\frac{\Gamma \left(\frac{r+3}{2} \right)}{(n-q)^{\frac{r+3}{3}}} + \frac{\sqrt{n} \Gamma \left(\frac{r+4}{2} \right)}{(n-q)^{\frac{r+4}{2}}} \right].$$

Similarly, by (1.5) and (1.9) we can write

$$\begin{aligned}
|f^{(r+2)}(t) - f^{(r+2)}(x)| &\leq e^{qx^2} \omega_1(f^{(r+2)}, L_q^\infty; |t-x|) \\
&\leq e^{q|t-x|^2 + qx^2} (1 + |t-x|\sqrt{n}) e^{q|t-x|^2} \omega_1 \left(f^{(r+2)}, L_q^\infty; \frac{1}{\sqrt{n}} \right),
\end{aligned}$$

and from (3.10), there holds:

$$\begin{aligned}
S_1(t, x) &\leq \int_0^1 (1-u)^{r+1} \omega_1(f^{(r+2)}, L_q^\infty; u|t-x|) e^{qt^2} du \\
&\leq e^{qt^2} \omega_1(f^{(r+2)}, L_q^\infty; |t-x|) \int_0^1 (1-u)^{r+1} du \\
&\leq \frac{1}{r+2} e^{q|t-x|^2 + qx^2} (1 + |t-x|\sqrt{n}) \omega_1 \left(f^{(r+2)}, L_q^\infty; \frac{1}{\sqrt{n}} \right).
\end{aligned}$$

Then, using (2.4) and above inequalities, we conclude that (3.13)

$$\|K_2(x)\|_{\infty, 2q} \leq \frac{\omega_1 \left(f^{(r+2)}, L_q^\infty; \frac{1}{\sqrt{n}} \right)}{(r+2)!} \sqrt{\frac{n}{\pi}} \left[\frac{\Gamma \left(\frac{r+3}{2} \right)}{(n-q)^{\frac{r+3}{3}}} + \frac{\sqrt{n} \Gamma \left(\frac{r+4}{2} \right)}{(n-q)^{\frac{r+4}{2}}} \right],$$

and

$$\|K_3(x)\|_{\infty, 2q} \leq \frac{\omega_1 \left(f^{(r+2)}, L_q^\infty; \frac{1}{\sqrt{n}} \right)}{(r+2)!} \sqrt{\frac{n}{\pi}} \left[\frac{\Gamma \left(\frac{r+3}{2} \right)}{(n-2q)^{\frac{r+3}{3}}} + \frac{\sqrt{n} \Gamma \left(\frac{r+4}{2} \right)}{(n-q)^{\frac{r+4}{2}}} \right]$$

For $n \geq q + 1$. In short by (3.13) and (3.14), we achieve the desired inequality (3.8).

REFERENCES


- [1] Rempulska, L. and Tomczak, K., (2009). On some properties of the Picard operators. *Archiv der Mathematik*. (Brno), 45, 125-135.
- [2] Mohapatra, R. N. and Rodriguez, R. S. (1990). On the rate of convergence of singular integrals for Hölders continuous functions. *Mathematische Nachrichten* 149, 117-124.
- [3] Anastassiou, G. A. and Aral, A. (2010). On Gauss-Weierstrass type integral operators. *Demonstratio Mathematica*, 43(4), 841-849
- [4] Deeba, E., Mohapatra, R. N. and Rodriguez, R. S. (1988). On the degree of approximation of some singular integrals. *Rendiconti di Matematica e delle sue Applicazioni*, 7, 345-355.
- [5] Krech, G. and Krech, I. (2019). On some bivariate Gauss-Weierstrass operators. *Constructive Mathematical Analysis*, 2(2), 57-53.
- [6] Butzer, P. L. and Nessel, R. J. (1971). *Fourier Analysis and Approximation, I,II*; Birkhauser, Basel and Academic Press, New York.
- [7] Kirov, G. H. (1992). A generalization of the Bernstein polynomials. *Mathematica Balkanica (N.S.)*, 2(2), 147-153.
- [8] Rempulska, L. and Walczak, Z. (2005). On modified Picard and Gauss-Weierstrass singular integrals. *Ukrainian Mathematical Journal*, 57(11), 1844-1852.
- [9] Becker, M., Kucharski, D. and Nessel, R. J. (1978). Global approximation theorems for the Szasz-Mirakyan operators in exponential weight spaces, in *Linear Spaces and Approximation*, Proc. Conf. Oberwolfach, 1977), Birkhauser Verlag, Basel, 319-333.
- [10] Ditzian, Z. and Totik, V. (1987). *Moduli of Smoothness*, Springer-Verlag, New-York.
- [11] Yilmaz, B. (2019). On some approximation properties of Gauss-Weierstrass operators, *Communications Faculty Sciences University of Ankara Series A1: Mathematics and Statistics*, 68(2), 2154-2160.

CHAPTER VI

APPROXIMATION BY FUZZY BERNSTEIN TYPE RATIONAL FUNCTIONS

Esma Yildiz Özkan¹

¹(Assoc. Prof.), Gazi University, e-mail: esmayildiz@gazi.edu.tr

 ORCID 0000-0003-1283-833X

1. INTRODUCTION

The Bernstein type rational functions were introduced by Balázs, in which it is considered some approximation properties and its relations with probability theory (Balázs, 1975; Balázs, 1977). Balázs and Szabados proved the approximation results under some more restrictive conditions (Balázs and Szabados, 1982). Totik set down the saturation properties of the Bernstein type rational functions (Totik, 1984). Recently, q -analogue and (p,q) -analogue of one and two variable Bernstein type rational functions have been studied, for instance, see the references (Ispir and Ozkan, 2013; Ozkan, 2014; Ozkan, 2016; Ozkan, 2019).

Zareh introduced the fuzzy sets in (Zareh, 1965). The fuzzy real numbers were defined by Wu and Ming (Wu and Ming, 1991; Wu and Ming, 1992). Recently, significant results of the approximation theory have been generalized in fuzzy sense. The Weierstrass approximation theorem in fuzzy sense was given by Gal (Gal, 1993; Gal 1994), Wu and Danghang (Wu and Danghang, 1999). Anastassiou presented the corresponding Shisha-Mond inequality in fuzzy sense and the well-known Korovkin theorem, and he applied the results to the fuzzy operators. Also, he studied the fuzzy Korovkin type approximation of the Szasz-Mirakjan and the Baskakov-type operators defined on positive real axis in fuzzy sense (Anastassiou, 2010).

In this chapter, we consider Bernstein type rational functions defined by Balázs called Balázs operator. We give degree of the approximation for the Balázs operator concerning to bounded and continuous functions with the help of the first modulus of continuity considering the basic Riesz representation theorem for any linear positive operator. Later, we define fuzzy Balázs operator and give the relations between the Balázs operator and the corresponding fuzzy Balázs operator. Lastly, we obtain degree of the approximation for the fuzzy Balázs operator concerning to fuzzy bounded and continuous functions on positive real axis with the help of the

fuzzy modulus of continuity considering the fuzzy Riesz representation theorem.

2. PRELIMINARIES

In this part, we recall some basic definitions and results. The details can be found in the references (Goetschel and Voxman, 1986; Wu and Ming, 1991; Wu and Ming, 1992; Ming, 1993; Kim and Ghil, 1997; Anastassiou, 2010). Fuzzy real number is a sententious concept in fuzzy mathematics. However, there are many definitions, in this study, we purpose the following basic concepts.

Definition 1. Let $z: \mathbb{R} \rightarrow [0,1]$ be any function. z is called a fuzzy real number if z satisfies

- i. There exists at least an element $x_0 \in \mathbb{R}$ satisfying $z(x_0) = 1$,
- ii. For each $\lambda \in [0,1]$ and $\rho, \sigma \in \mathbb{R}$

$$z(\lambda\rho + (1 - \lambda)\sigma) \geq \min\{z(x), z(y)\},$$

equivalently, for all $\eta \in [0,1]$, the set $\{x \in \mathbb{R}: z(x) \geq \eta\}$ is convex.

- iii. There exists at least a neighborhood $V(x_0)$ satisfying $z(x) \leq z(x_0) + \varepsilon$ for all $x \in V(x_0)$,
- iv. The set $\overline{\{x \in \mathbb{R}: z(x) > 0\}}$ is compact, where \bar{A} is the closure of any set A .

By $\mathbb{R}_{\mathcal{F}}$ is denoted the set of all fuzzy real numbers. Let denote us by $[z]^r = \{x \in \mathbb{R}: z(x) \geq r\}$, which is a bounded and closed interval of \mathbb{R} for all $r \in [0,1]$. Let $r_1, r_2 \in [0,1]$ such that $r_1 \leq r_2$ then $[z]^{r_1} \subseteq [z]^{r_2}$. The addition denoted by $w \oplus z$ and the scalar product denoted by $k \odot z$ on $\mathbb{R}_{\mathcal{F}}$ are defined by

$$[w \oplus z]^r = [w]^r + [z]^r, [k \odot z]^r = k[z]^r,$$

uniquely for $w, z \in \mathbb{R}_{\mathcal{F}}$, $k \in \mathbb{R}$ and $r \in [0,1]$, respectively.

Let $D: \mathbb{R}_{\mathcal{F}} \times \mathbb{R}_{\mathcal{F}} \rightarrow [0, \infty)$ be defined by

$$D(w, v) = \sup_{r \in [0,1]} \max\{|w_-^r - z_-^r|, |w_+^r - z_+^r|\},$$

where $[z]^r = [z_-^r, z_+^r]$, $[w]^r = [w_-^r, w_+^r] \subset \mathbb{R}$. D is a metric on $\mathbb{R}_{\mathcal{F}}$. $(\mathbb{R}_{\mathcal{F}}, D)$ is a complete metric space, which has very close properties of a metric derived by a norm. A partial order on $\mathbb{R}_{\mathcal{F}}$ is defined by “ \leq ” such that $w, z \in \mathbb{R}_{\mathcal{F}}$, $w \leq z$ if and only if $[w]^r \subseteq [z]^r$ for all $r \in [0,1]$ if and only if $w_-^r \leq z_-^r$, $w_+^r \leq z_+^r$ for all $r \in [0,1]$.

Lemma 1. Let $k, l \in \mathbb{R}$, $w, z \in \mathbb{R}_{\mathcal{F}}$ and $\tilde{0} = \chi_{\{0\}}$ be the characteristic function of $\{0\}$. Then

- i. A neutral element with respect to \oplus is $\tilde{0} \in \mathbb{R}_{\mathcal{F}}$,

- ii. For each $z \neq \tilde{0}, z \in \mathbb{R}_{\mathcal{F}}$ has not an opposite in $\mathbb{R}_{\mathcal{F}}$,
- iii. If $k, l > 0$ or $k, l \leq 0$, we have

$$(k + l) \odot z = k \odot z \oplus l \odot z,$$

(The above property does not hold for general $k, l \in \mathbb{R}$.)

- iv. $k \odot (w \oplus z) = k \odot w \oplus k \odot z$,
- v. $k \odot (l \odot z) = (k \cdot l) \odot z$.

Let (X, d) be any metric space and $S \subset X$ be a subset. A function $\varphi: S \rightarrow \mathbb{R}_{\mathcal{F}}$ is called a fuzzy real number valued function on S or shortly a fuzzy function on S .

Definition 2. Let S be an open (or compact) subset of real numbers. Any function $\varphi: S \rightarrow \mathbb{R}_{\mathcal{F}}$ is called a fuzzy continuous at $x_0 \in S$ if and only if φ is sequential continuous at $x_0 \in S$. If φ is continuous for each $x_0 \in S$, then φ is called a fuzzy continuous function on S . The space of all fuzzy continuous functions is denoted by $\mathcal{C}_{\mathcal{F}}(S)$.

Definition 3. Any function $\varphi: S \rightarrow \mathbb{R}_{\mathcal{F}}$ is called a fuzzy bounded function on S if and only if there exists $M > 0$ such that $D(f(x), \tilde{0}) \leq M$ for all $x \in S$.

Definition 4. Let $\varphi: S \rightarrow \mathbb{R}_{\mathcal{F}}$ be a fuzzy function on S . The first modulus of continuity of φ is defined by

$$\omega_1^{\mathcal{F}}(\varphi; \delta) := \sup_{\substack{x, y \in S \\ d(x, y) \leq \delta}} D(\varphi(x), \varphi(y)),$$

for $0 < \delta < \text{diameter}(S)$. If $\delta > \text{diameter}(S)$ then

$$\omega_1^{\mathcal{F}}(\varphi; \delta) := \omega_1^{\mathcal{F}}(\varphi; \text{diameter}(S)).$$

Proposition 1. For $\delta > 0$, assume that $\omega_1^{\mathcal{F}}(\varphi; \delta)$, $\omega_1(\varphi_-^r; \delta)$ and $\omega_1(\varphi_+^r; \delta)$ are finite. Then it holds

$$\omega_1^{\mathcal{F}}(\varphi; \delta) = \sup_{r \in [0, 1]} \max\{\omega_1(\varphi_-^r; \delta), \omega_1(\varphi_+^r; \delta)\},$$

where $\omega_1(f; \delta) = \sup_{\substack{t, x \in S \\ |t-x| \leq \delta}} |f(t) - f(x)|$ is the first modulus of continuity

for all $f \in \mathcal{C}(S)$ satisfying

$$|f(t) - f(x)| \leq \omega_1(f; \delta) \left(1 + \frac{|t-x|}{\delta}\right) \quad (2.1)$$

We recall the following general fuzzy integral.

Let (Ω, Σ, μ) be a complete σ -finite measure space and let Φ be a fuzzy function on Ω defined by

$$\Phi(\omega) = \{(\Phi_-^r(\omega), \Phi_+^r(\omega)): r \in [0, 1], \omega \in \Omega\}.$$

Definition 5. $\Phi: \Omega \rightarrow \mathbb{R}_{\mathcal{F}}$ is called measurable if and only if for all closed subset E of \mathbb{R} , the function $\Phi^{-1}(E): \Omega \rightarrow [0,1]$ defined by

$$\Phi^{-1}(E)(\omega) = \sup_{x \in E} \Phi(\omega)(x), \forall \omega \in \Omega,$$

is measurable.

Theorem 1. The followings are equivalent:

- i. Φ is measurable,
- ii. For all $r \in [0,1]$, Φ_-^r and Φ_+^r are measurable. Since Φ_-^r and Φ_+^r are integrable, we have that the corresponding parameterized representation

$$\left\{ \left(\int_A \Phi_-^r d\mu, \int_A \Phi_+^r d\mu \right) : r \in [0,1], A \in \Sigma \right\}$$

is a fuzzy real number.

Definition 6. A measurable function $\Phi: \Omega \rightarrow \mathbb{R}_{\mathcal{F}}$ is called integrable if Φ_-^r and Φ_+^r are integrable for all $r \in [0,1]$, or equivalently, if Φ_-^0 and Φ_+^0 are integrable. In this case, the fuzzy integral of Φ over $A \in \Sigma$ is defined by

$$\int_A \Phi d\mu := \left\{ \left(\int_A \Phi_-^r d\mu, \int_A \Phi_+^r d\mu \right) : r \in [0,1], \forall A \in \Sigma \right\}.$$

The fuzzy integral has the following properties.

Theorem 2. Let $\Phi, \Psi: \Omega \rightarrow \mathbb{R}_{\mathcal{F}}$ be fuzzy integrable functions. Then

- i. Let $c_1, c_2 \in \mathbb{R}$, then $c_1\Phi + c_2\Psi$ is integrable and

$$\int_A (c_1\Phi + c_2\Psi) d\mu = c_1 \int_A \Phi d\mu + c_2 \int_A \Psi d\mu, \forall A \in \Sigma$$

- ii. $D(\Phi, \Psi)$ is a real valued integrable function and

$$D\left(\int_A \Phi d\mu, \int_A \Psi d\mu\right) \leq \int_A D(\Phi, \Psi) d\mu, \forall A \in \Sigma.$$

Let (X, d) be any metric space and S be a subset of X .

Definition 7. Let φ, ϕ be fuzzy functions on S . We denote $\varphi \succcurlyeq \phi$ if and only if $\varphi(x) \geq \phi(x)$ for all $x \in S$ if and only if $\varphi_+^r(x) \geq \phi_+^r(x)$ and $\varphi_-^r(x) \geq \phi_-^r(x)$ for all $x \in S, r \in [0,1]$ if and only if $\varphi_+^r \geq \phi_+^r$ and $\varphi_-^r \geq \phi_-^r$ for all $r \in [0,1]$.

Definition 8. Let $L_{\mathcal{F}}$ be any operator from $C_{\mathcal{F}}(S)$ into itself, such that

$$L_{\mathcal{F}}(c_1\varphi + c_2\phi) = c_1L_{\mathcal{F}}(\varphi) + c_2L_{\mathcal{F}}(\phi),$$

for all $c_1, c_2 \in \mathbb{R}$ and $\varphi, \phi \in C_{\mathcal{F}}(S)$, then $L_{\mathcal{F}}$ is called a fuzzy linear operator on the space $C_{\mathcal{F}}(S)$.

Definition 9. Let $L_{\mathcal{F}}$ be a fuzzy linear operator from $C_{\mathcal{F}}(S)$ into itself. $L_{\mathcal{F}}$ is called positive if and only if whenever $\varphi, \phi \in C_{\mathcal{F}}(S)$ such that $\varphi \succcurlyeq \phi$ then $L_{\mathcal{F}}(\varphi) \succcurlyeq L_{\mathcal{F}}(\phi)$ if and only if $(L_{\mathcal{F}}(\varphi))_+^r \geq (L_{\mathcal{F}}(\phi))_+^r$ and $(L_{\mathcal{F}}(\varphi))_-^r \geq (L_{\mathcal{F}}(\phi))_-^r$ for all $r \in [0,1]$. Here

$$[L_{\mathcal{F}}(\varphi)(x)]^r = \left[(L_{\mathcal{F}}(\varphi)(x))_-^r, (L_{\mathcal{F}}(\varphi)(x))_+^r \right],$$

for all $x \in S, r \in [0,1]$.

For example, the fuzzy Bernstein operator is a fuzzy linear positive operator (Gal, 1994).

Let W be a compact subset of any metric space (X, d) .

Theorem 3. Let L be a linear positive operator from $C(W)$ into itself. Then there exists uniquely a fuzzy linear positive operator $L_{\mathcal{F}}$ on $C_{\mathcal{F}}(W)$ produced by L satisfying

$$(L_{\mathcal{F}}(\varphi))_{\pm}^r = L(\varphi_{\pm}^r),$$

respectively in \pm , for all $r \in [0,1]$ and $\varphi \in C_{\mathcal{F}}(W)$. Additionally, if $L(\varphi_{\pm}^r)$ are equicontinuous regarding to $r \in [0,1]$ respectively in \pm , then $L_{\mathcal{F}}(\varphi) \in C_{\mathcal{F}}(W)$ whenever $\varphi \in C_{\mathcal{F}}(W)$.

Let $L_{\mathcal{F}}$ be a fuzzy linear positive operator from $C_{\mathcal{F}}(W)$ into itself. Assume that there exists a linear positive operator L from $C(W)$ into itself with the properties

$$(L_{\mathcal{F}}(\varphi))_{\pm}^r = L(\varphi_{\pm}^r), \tag{2.2}$$

respectively in \pm , for all $r \in [0,1]$ and $\varphi \in C_{\mathcal{F}}(W)$. For example, the real Bernstein operators and the corresponding fuzzy Bernstein operators fulfill the properties given by (2.2) (see Example 9.7 in (Anastassiou, 2010)).

We recall the fuzzy Riesz representation theorem.

Theorem 4. Let $L_{\mathcal{F}}$ be a fuzzy linear positive operator from $C_{\mathcal{F}}(W)$ into itself satisfying the properties given by (2.2). Then there exists a unique positive finite complete Borel measure μ_x on W for all $x \in W$ such that

$$L_{\mathcal{F}}(\varphi)(x) = \int_W \varphi(s)\mu_x(ds),$$

for all $\varphi \in C_{\mathcal{F}}(W)$.

Remark 1. Let L be a linear positive operator from $C(W)$ into itself, by the basic Riesz representation theorem, then we have

$$L(f)(x) = \int_W f(s)\mu_x(ds),$$

for all $f \in C(W)$, where μ_x is a unique positive finite complete Borel measure on W .

Theorem 5. Let $(V, \|\cdot\|)$ be any real normed vector space, Y be a convex subset of V , $x_0 \in Y$ be fixed and μ be a complete Borel measure on Y such that $\mu(Y) = p > 0$. Let also $\varphi \in C_{\mathcal{F}}^B(Y)$, i.e. φ is a fuzzy real valued bounded and continuous function on Y . Then the following inequality holds

$$\begin{aligned} D\left(\int_Y \varphi(s)d_{\mu}s, \varphi(x_0)\right) &\leq (p-1)D(\varphi(x_0), \delta) \\ &+ \omega_1^{\mathcal{F}}\left(\varphi; \left(\int_Y \|s-x_0\|^2 d_{\mu}s\right)^{1/2}\right) \min\{p+1, p+\sqrt{p}\}. \end{aligned} \tag{2.3}$$

Selecting $Y = \mathbb{R}^+ = [0, \infty)$, we obtain

$$\begin{aligned} D\left(\int_Y \varphi(s)d_{\mu}s, \varphi(x_0)\right) &\leq (p-1)D(\varphi(x_0), \delta) \\ &+ \omega_1^{\mathcal{F}}\left(\varphi; \left(\int_{\mathbb{R}^+} \|s-x_0\|^2 d_{\mu}s\right)^{1/2}\right) \min\{p+1, p+\sqrt{p}\}, \end{aligned} \tag{2.4}$$

for all $\varphi \in C_{\mathcal{F}}^B(\mathbb{R}^+)$.

3. SOME APPROXIMATION RESULTS FOR FUZZY BALÁZS OPERATORS

Let $C_B(\mathbb{R}^+)$ be the space of all the real valued continuous and bounded functions defined on \mathbb{R}^+ .

Bernstein type rational functions concerning to any function $f \in C_B(\mathbb{R}^+)$ is defined by

$$R_n(f; x) = \frac{1}{(1 + a_n x)^n} \sum_{k=0}^n f\left(\frac{k}{b_n}\right) \binom{n}{k} (a_n x)^k, n \in \mathbb{N},$$

where (a_n) and (b_n) are any real sequences independent of x (Balázs, 1975). Here R_n is a linear positive operator called Balázs operator from $C_B(\mathbb{R}^+)$ into itself.

Lemma 2. If $x \in \mathbb{R}^+$, then it holds the following inequalities

- i. $R_n(1; x) = 1,$
- ii. $R_n(s; x) = \frac{x}{1+a_n x},$
- iii. $R_n(s^2; x) = \frac{x^2 + \frac{x}{b_n}}{(1+a_n x)^2},$
- iv. $R_n(s - x; x) = -\frac{a_n x^2}{1+a_n x},$
- v. $R_n((s - x)^2; x) = \frac{a_n^2 x^4 + \frac{x}{b_n}}{(1+a_n x)^2}.$

Let X_j be real random variables, which are distributed independently and identically and let $S_n = \sum_{j=1}^n X_j$ for $n \in \mathbb{N}$.

Let the expectation operator be denoted by E . Then the Balázs operators R_n has the form $E\left(f\left(\frac{S_n}{n}\right)\right)$.

Let X be any random variable. The geometric distribution of X is defined by

$$P_X := \sum_{v=0}^n \frac{1}{1 + a_n x} \left(\frac{a_n x}{1 + a_n x}\right)^v \delta_v,$$

where δ_v is Dirac measure at v . In this case, $E(X) = 1 + a_n x$ and $Var(X) = a_n x(1 + a_n x)$. The corresponding probability measure μ for the Balázs operator R_n is defined by

$$\mu := \frac{1}{(1 + a_n x)^n} \sum_{i=0}^n \binom{n}{i} (a_n x)^i \delta_{i/n}.$$

Now, we have the following degree of the approximation for the Balázs operators R_n .

Theorem 6. If $f \in C_B(\mathbb{R}^+)$ then it holds

$$|R_n(f; x) - f(x)| \leq 2\omega_1\left(f; \sqrt{\frac{a_n^2 x^4 + \frac{x}{b_n}}{(1+a_n x)^2}}\right), \quad (3.1)$$

for all $x \in \mathbb{R}^+$ and $n \in \mathbb{N}$.

Proof. Let the probability measure on \mathbb{R}^+ be denoted by μ . By Considering Remark 1 and (i) of Theorem 2, we can be written

$$\begin{aligned} |R_n(f; x) - f(x)| &= \left| \int_{\mathbb{R}^+} f(s) d_\mu s - f(x) \right|, \\ &= \left| \int_{\mathbb{R}^+} (f(s) - f(x)) d_\mu s \right|. \end{aligned} \quad (3.2)$$

From (3.2), by considering Corollary 7.1.1 in (Anastassiou, 1993), we get

$$|R_n(f; x) - f(x)| \leq \int_{\mathbb{R}^+} |f(s) - f(x)| d_\mu s. \quad (3.3)$$

By applying (2.1) to (3.3), we obtain

$$|R_n(f; x) - f(x)| \leq \omega_1(f; \delta) \left(1 + \frac{1}{\delta} \int_{\mathbb{R}^+} |s - x| d_\mu s \right). \quad (3.4)$$

By considering Cauchy-Schwarz inequality, we get

$$|R_n(f; x) - f(x)| \leq \omega_1(f; \delta) \left(1 + \frac{1}{\delta} \left(\int_{\mathbb{R}^+} (s - x)^2 d_\mu s \right)^{1/2} \right),$$

which implies

$$|R_n(f; x) - f(x)| \leq \omega_1(f; \delta) \left(1 + \frac{1}{\delta} (R_n((s - x)^2; x))^{1/2} \right), \quad (3.5)$$

In (3.5), by selecting $\delta := (R_n((s - x)^2; x))^{1/2}$ given by (v) of Lemma 2, we reach desired result.

Remark 2. Taking $\mu = F_{\frac{S_n}{n}}$ in (3.1), we obtain that the Balázs operator R_n has the form

$$E \left(f \left(\frac{S_n}{n} \right) \right) = \int_{\mathbb{R}^+} dF_{\frac{S_n}{n}}.$$

In this case, the standard deviation in geometric case is

$$\left(\int_{\mathbb{R}^+} (s - x)^2 d_\mu s \right)^{1/2} = \frac{\sqrt{a_n^2 x^4 + \frac{x}{b_n}}}{(1 + a_n x)^2}.$$

Now, we define the fuzzy variant of Balázs operator.

Definition 10. We define fuzzy Balázs operator concerning to $\varphi \in C_{\mathcal{F}}(\mathbb{R}^+)$ by

$$R_n^{\mathcal{F}}(\varphi; x) = \frac{1}{(1 + a_n x)^n} \sum_{j=0}^n * \varphi \left(\frac{j}{b_n} \right) \odot \binom{n}{j} (a_n x)^j, n \in \mathbb{N}, x \in \mathbb{R}^+,$$

where (a_n) and (b_n) are any real sequences independent of x and $\sum_{j=0}^n$ * is finite fuzzy summation on $\mathbb{R}_{\mathcal{F}}$.

In the following, we can give the relation between the Balázs operator R_n and the fuzzy Balázs operator $R_n^{\mathcal{F}}$ and some properties of the fuzzy Balázs operator.

Lemma 3. Let $\varphi: \mathbb{R}^+ \rightarrow \mathbb{R}_{\mathcal{F}}$ be any fuzzy continuous function.

- i. If $\varphi \in C_{\mathcal{F}}^B(\mathbb{R}^+)$ then $R_n(\varphi_{\pm}^r; x)$ are uniformly bounded for all $r \in [0,1]$, $x \in \mathbb{R}^+$, respectively in \pm ,
- ii. The fuzzy Balázs operator $R_n^{\mathcal{F}}$ is a fuzzy linear positive operator,
- iii. $\left(R_n^{\mathcal{F}}(\varphi; x)\right)_{\pm}^r = R_n(\varphi_{\pm}^r; x)$ for all $r \in [0,1]$, $x \in \mathbb{R}^+$,
- iv. If $\varphi \in C_{\mathcal{F}}^B(\mathbb{R}^+)$ then the fuzzy Balázs operator $R_n^{\mathcal{F}}(\varphi; \cdot) \in C_{\mathcal{F}}^B(\mathbb{R}^+)$.

Proof.

- i. For $\varphi \in C_{\mathcal{F}}^B(\mathbb{R}^+)$, φ_{\pm}^r are equicontinuous, respectively in \pm , and uniformly bounded in r over \mathbb{R}^+ . By Proposition 1 and Theorem 6, we see that

$$\begin{aligned} |R_n(\varphi_{\pm}^r; x)| &\leq |\varphi_{\pm}^r(x)| + 2\omega_1\left(\varphi_{\pm}^r; \sqrt{\frac{a_n^2 x^4 + \frac{x}{b_n}}{(1+a_n x)^2}}\right), r \in [0,1], x \in \mathbb{R}^+, \\ &\leq D(\varphi(x), \delta) + \omega_1^{\mathcal{F}}\left(\varphi; \sqrt{\frac{a_n^2 x^4 + \frac{x}{b_n}}{(1+a_n x)^2}}\right) := M(\varphi), \end{aligned}$$

i.e.

$$|R_n(\varphi_{\pm}^r; x)| \leq M(\varphi),$$

where the constant $M(\varphi) > 0$ for all $r \in [0,1]$, $x \in \mathbb{R}^+$, thus $R_n(\varphi_{\pm}^r; x)$ are uniformly bounded for all $r \in [0,1]$, $x \in \mathbb{R}^+$.

- ii. We prove the linearity by considering Definition 8. Let $\varphi, \phi: \mathbb{R}^+ \rightarrow \mathbb{R}_{\mathcal{F}}$ be fuzzy continuous functions and $\gamma, \rho \in \mathbb{R}$.

$$\begin{aligned} R_n^{\mathcal{F}}(\gamma\varphi + \rho\phi; x) &= \frac{1}{(1+a_n x)^n} \sum_{j=0}^n * (\gamma\varphi + \rho\phi) \left(\frac{j}{b_n}\right) \odot \binom{n}{j} (a_n x)^j, \\ &= \frac{1}{(1+a_n x)^n} \sum_{j=0}^n * \left[\gamma \odot \varphi \left(\frac{j}{b_n}\right) \oplus \rho \odot \phi \left(\frac{j}{b_n}\right) \right] \odot \binom{n}{j} (a_n x)^j, \end{aligned}$$

$$\begin{aligned}
&= \frac{1}{(1+a_n x)^n} \sum_{j=0}^n * \gamma \odot \varphi \left(\frac{j}{b_n} \right) \odot \binom{n}{j} (a_n x)^j, \\
&\quad \oplus \frac{1}{(1+a_n x)^n} \sum_{j=0}^n * \rho \odot \phi \left(\frac{j}{b_n} \right) \odot \binom{n}{j} (a_n x)^j, \\
&= \gamma \odot \frac{1}{(1+a_n x)^n} \sum_{j=0}^n * \odot \varphi \left(\frac{j}{b_n} \right) \odot \binom{n}{j} (a_n x)^j, \\
&\quad \oplus \rho \odot \frac{1}{(1+a_n x)^n} \sum_{j=0}^n * \odot \phi \left(\frac{j}{b_n} \right) \odot \binom{n}{j} (a_n x)^j, \\
&= \gamma \odot R_n^{\mathcal{F}}(\varphi; x) \oplus \rho \odot R_n^{\mathcal{F}}(\phi; x).
\end{aligned}$$

We obtain the positivity by considering Definition 9. Let $\varphi, \phi: \mathbb{R}^+ \rightarrow \mathbb{R}_{\mathcal{F}}$ be fuzzy continuous functions, then the functions φ_{\pm}^r and ϕ_{\pm}^r map \mathbb{R}^+ to \mathbb{R} for all $r \in [0,1]$. Assume that $\varphi \succcurlyeq \phi$, if and only if $\varphi_+^r \geq \phi_+^r$ and $\varphi_-^r \geq \phi_-^r$ for all $r \in [0,1]$. Then

$$\varphi_{\pm}^r \left(\frac{j}{b_n} \right) \geq \phi_{\pm}^r \left(\frac{j}{b_n} \right),$$

respectively in respect to \pm for all $r \in [0,1]$, and

$$\varphi_{\pm}^r \binom{j}{b_n} \binom{n}{j} (a_n x)^j \geq \phi_{\pm}^r \binom{j}{b_n} \binom{n}{j} (a_n x)^j, \forall r \in [0,1].$$

And consequently, it holds

$$\begin{aligned}
&\frac{1}{(1+a_n x)^n} \sum_{j=0}^n \varphi_{\pm}^r \binom{j}{b_n} \binom{n}{j} (a_n x)^j \geq \\
&\frac{1}{(1+a_n x)^n} \sum_{j=0}^n \phi_{\pm}^r \binom{j}{b_n} \binom{n}{j} (a_n x)^j.
\end{aligned}$$

Therefore

$$R_n(\varphi_{\pm}^r; x) \geq R_n(\phi_{\pm}^r; x), \forall r \in [0,1].$$

- iii. Let $\varphi: \mathbb{R}^+ \rightarrow \mathbb{R}_{\mathcal{F}}$ be a fuzzy continuous function, which has the form $[\varphi(x)]^r = [\varphi_-^r(x), \varphi_+^r(x)]$ for all $r \in [0,1], x \in \mathbb{R}^+$. Then

$$\begin{aligned}
[R_n^{\mathcal{F}}(\varphi; x)]^r &= \left[\left(R_n^{\mathcal{F}}(\varphi; x) \right)_-^r, \left(R_n^{\mathcal{F}}(\varphi; x) \right)_+^r \right] \\
&= \left[\frac{1}{(1+a_n x)^n} \left(\sum_{j=0}^n * \varphi \left(\frac{j}{b_n} \right) \odot \binom{n}{j} (a_n x)^j \right)_-^r, \right. \\
&\quad \left. \frac{1}{(1+a_n x)^n} \left(\sum_{j=0}^n * \varphi \left(\frac{j}{b_n} \right) \odot \binom{n}{j} (a_n x)^j \right)_+^r \right]
\end{aligned}$$

$$\begin{aligned}
& \left. \frac{1}{(1+a_n x)^n} \left(\sum_{j=0}^n * \varphi \left(\frac{j}{b_n} \right) \odot \binom{n}{j} (a_n x)^j \right)^r \right]_+ \\
&= \left[\frac{1}{(1+a_n x)^n} \sum_{j=0}^n \varphi_-^r \left(\frac{j}{b_n} \right) \binom{n}{j} (a_n x)^j, \right. \\
& \quad \left. \frac{1}{(1+a_n x)^n} \sum_{j=0}^n \varphi_+^r \left(\frac{j}{b_n} \right) \binom{n}{j} (a_n x)^j \right] \\
&= [R_n(\varphi_-^r; x), R_n(\varphi_+^r; x)].
\end{aligned}$$

Thus $(R_n^{\mathcal{F}}(\varphi; x))_{\pm}^r = R_n(\varphi_{\pm}^r; x)$ for all $r \in [0,1]$, $x \in \mathbb{R}^+$, respectively.

- iv. For $\varphi \in C_{\mathcal{F}}^B(\mathbb{R}^+)$, by Theorem 3, the Balázs operator produces the unique fuzzy linear positive operator $R_n^{\mathcal{F}}(\varphi; x)$ from $C_{\mathcal{F}}(\mathbb{R}^+)$ into itself satisfying

$$R_n^{\mathcal{F}}(\varphi; x) = \int_{\mathbb{R}^+} \varphi d\mu,$$

and since $R_n(\varphi_{\pm}^r; x)$ are equicontinuous regarding to $r \in [0,1]$, respectively in \pm , $R_n^{\mathcal{F}}(\varphi; \cdot)$ is in $C_{\mathcal{F}}(\mathbb{R}^+)$.

On the other hand,

$$\begin{aligned}
D(R_n^{\mathcal{F}}(\varphi; x), \tilde{\delta}) &= \frac{1}{(1+a_n x)^n} D \left(\sum_{j=0}^n * \varphi \left(\frac{j}{b_n} \right) \odot \binom{n}{j} (a_n x)^j, \tilde{\delta} \right) \\
&\leq \frac{1}{(1+a_n x)^n} \sum_{j=0}^n \binom{n}{j} (a_n x)^j D \left(\varphi \left(\frac{j}{b_n} \right), \tilde{\delta} \right) \\
&\leq M \frac{1}{(1+a_n x)^n} \sum_{j=0}^n \binom{n}{j} (a_n x)^j = M.
\end{aligned}$$

Here there exists $M > 0$ such that $D \left(\varphi \left(\frac{j}{b_n} \right), \tilde{\delta} \right) \leq M$, since φ is fuzzy bounded, i. e. $R_n^{\mathcal{F}}(\varphi; \cdot)$ is fuzzy bounded on \mathbb{R}^+ . Consequently, $R_n^{\mathcal{F}}(\varphi; \cdot)$ is in $C_{\mathcal{F}}^B(\mathbb{R}^+)$.

Now, we give the following degree of approximation for the fuzzy Balázs operator $R_n^{\mathcal{F}}$.

Theorem 7. For $\varphi \in C_{\mathcal{F}}^B(\mathbb{R}^+)$, we have

$$D\left(R_n^{\mathcal{F}}(\varphi; x), \varphi(x)\right) \leq 2\omega_1^{\mathcal{F}}\left(\varphi; \frac{\sqrt{a_n^2 x^4 + \frac{x}{b_n}}}{(1+a_n x)^2}\right), x \in \mathbb{R}^+.$$

Proof. By Theorem 4, we can write

$$D\left(R_n^{\mathcal{F}}(\varphi; x), \varphi(x)\right) \leq D\left(\int_{\mathbb{R}^+} \varphi(s) d_{\mu} s, \varphi(x)\right), \quad (3.6)$$

for all $\varphi \in C_{\mathcal{F}}^B(\mathbb{R}^+)$. Considering (3.6) and Theorem 5, we we obtain

$$\begin{aligned} D\left(R_n^{\mathcal{F}}(\varphi; x), \varphi(x)\right) \\ \leq c_{\mu} \omega_1^{\mathcal{F}}\left(\varphi; \left(\int_{\mathbb{R}^+} (s-x)^2 d_{\mu} s\right)^{\frac{1}{2}}\right) + M|\mu(\mathbb{R}^+) - 1|. \end{aligned}$$

On the other hand, by Lemma 2, we acquire

$$\mu(\mathbb{R}^+) = \int_{\mathbb{R}^+} d_{\mu} s = R_n(1; x) = 1 < \infty,$$

which indicates

$$D\left(R_n^{\mathcal{F}}(\varphi; x), \varphi(x)\right) \leq 2\omega_1^{\mathcal{F}}\left(\varphi; \frac{\sqrt{a_n^2 x^4 + \frac{x}{b_n}}}{(1+a_n x)^2}\right), x \in \mathbb{R}^+.$$

4. CONCLUSION

Let (a_n) and (b_n) be any real sequences such that

$$\lim_{n \rightarrow \infty} a_n = \lim_{n \rightarrow \infty} \frac{1}{b_n} = 0 \text{ as } n \rightarrow \infty.$$

Then

$$\lim_{n \rightarrow \infty} \frac{\sqrt{a_n^2 x^4 + \frac{x}{b_n}}}{(1+a_n x)^2} = 0.$$

In Theorem 6,

$$\lim_{n \rightarrow \infty} \omega_1\left(f; \frac{\sqrt{a_n^2 x^4 + \frac{x}{b_n}}}{(1+a_n x)^2}\right) = 0,$$

which means $R_n(f; \cdot)$ converges to f on the space $C_B(\mathbb{R}^+)$.

In Theorem 7,

$$\lim_{n \rightarrow \infty} \omega_1^{\mathcal{F}} \left(\varphi; \frac{\sqrt{a_n^2 x^4 + \frac{x}{b_n}}}{(1+a_n x)^2} \right) = 0,$$

which means $R_n^{\mathcal{F}}(\varphi; \cdot)$ converges to φ on the space $C_{\mathcal{F}}^B(\mathbb{R}^+)$.

REFERENCES

1. Anastassiou, G.A. (1993) Moments in Probability and Approximation Theory. Pitman/Longman 287 UK.
2. Anastassiou, G.A. (2010) Fuzzy Mathematics: Approximation Theory. Springer-Verlag Berlin.
3. Balázs, K. (1975) Approximation by Bernstein type rational functions. Acta Math. Acad. Sci. Hungar. 26, 123-134.
4. Balázs, K. (1977) Approximation by Bernstein type rational functions and its relations with probability theory. (Hungarian) Magyar Tud. Acad. Mat. Fiz. Oszt. Közl. 23 (1-2), 41-68.
5. Balázs, K. and Szabados, J. (1982) Approximation by Bernstein type rational functions. II. Acta Math. Acad. Sci. Hungar. 40, 331-337.
6. Gal, S.G. (1993) A fuzzy variant of the Weierstrass' approximation theorem. J. Fuzzy Math. 1 (4), 865-872.
7. Gal, S.G. (1994) Degree of approximation of fuzzy mappings by fuzzy polynomials. J. Fuzzy Math. 2 (4), 847-853.
8. Goetschel, R. and Voxman, W. (1986) Elementary fuzzy calculus. Fuzzy Sets and Systems. 18, 31-43.
9. Kim, Y.K. and Ghil, B.M. (1997) Integrals of fuzzy real number valued functions. Fuzzy Sets and Systems. 86, 213-222.
10. Ming, M. (1993) On embedding problem of fuzzy number space. Part IV. Fuzzy Sets and Systems. 58, 185-193.
11. Ozkan, E.Y. (2016) An upper estimate of complex q -Balázs-Szabados-Kantorovich operators on compact disk. GUJS. 29 (2), 479-486.
12. E.Y. Özkan, (2016) Approximation by complex bivariate Balázs-Szabados operators, Bull. Malays. Math. Sci. Soc., 39 (1), 1-16.
13. Ozkan, E.Y. (2019) Approximation properties of Kantorovich type q -Balázs-Szabados operators. Demonstr. Math. 52 (1), 10-19.
14. Ozkan, E.Y. (2014) Approximation properties of bivariate complex q -Balázs-Szabados operators of tensor product kind. J. Inequal. Appl. 2014: 20, 1-12.
15. Ozkan, E.Y. (2014) Statistical approximation properties of q -Balázs-Szabados-Stancu operators. Filomat 28 (9), 1943-1952.
16. Ozkan, E.Y. and Ispir, N. (2018) Approximation by (p,q) -analogue of Balázs-Szabados operators. Filomat 32 (6), 2257-2271.
17. Ispir, N. and Ozkan, E.Y. (2013) Approximation properties of complex q -Balázs-Szabados operators in compact disks. J. Inequal. Appl. 2013: 361, 1-12.
18. Totik, V. (1984) Saturation for Bernstein type rational functions. Acta Math. Hungar. 43 (3-4), 219-250.
19. Wu, C. and Danghang, L. (1999) A fuzzy variant Weierstrass approximation theorem. J. Fuzzy Math. 7 (1), 101-104.


20. Wu, C. and Ming, M. (1991) On embedding problem of fuzzy number space. Part I. Fuzzy Sets and Systems. 44, 33-38.
21. Wu C. and Ming, M. (1992) On embedding problem of fuzzy number space. Part II. Fuzzy Sets and Systems. 45, 189-202.
22. Zareh, L.A. (1965) Fuzzy sets. Inform. and Control. 8, 338-353.

CHAPTER VII

CURVATURE TENSORS ON NORMAL METRIC CONTACT PAIR MANIFOLDS

İnan Ünal

(Asst. Prof.Dr.) Munzur University, e-mail: nanunal@munzur.edu.tr,

 ORCID 0000-0003-1318-9685

1. INTRODUCTION

A contact manifold is a $(2k + 1)$ -dimensional differentiable manifold with a contact form. Contact manifolds have many applications in mathematics and some applied areas such as mechanics, optics, thermodynamics, control theory and theoretical physics [1]. Also, contact manifolds are special solutions of Einstein fields equation with some certain conditions. Thus, these type of manifolds have many applications in the theory of relativity. In 1960s many developments occurred in the Riemannian geometry of contact manifolds, by tensorial viewpoint. Especially, Sasaki used tensorial approach for the Riemannian geometry of contact manifolds which is similar to the almost complex structures (see [2]). Later, the subject was become an interesting notion and took the attention of researchers who have been working on differential geometry. Along with many other studies, some subclasses of contact manifolds have been defined. An important one of these subclasses is the contact pair structures.

A Riemannian manifold with a contact pair structure is called as a contact pair manifold. These type of manifolds were firstly studied in [3] as bicontact manifolds. The authors worked on Calabi-Eckman manifolds by considering complex manifolds. They obtained some results on the contact and complex structures. The notion of bicontact manifolds have been studied under the name of contact pairs in the 2000s by Bande and Hadjar. They constructed almost contact structure on a contact pair manifold and defined the associated metric [4]. In 2010, the normality of an almost contact metric pair structure was studied in [5]. In 2020, presented author has defined the notion of generalized quasi-Einstein normal metric contact pair (NMCP) manifolds and obtained some results on curvature relations [6]. Also, same author worked on certain flatness conditions on NMCP manifolds in [7,8] and examined NMCP manifolds under semi-symmetry conditions [9].

A conformal transformation is a map which converts a metric to another with preserving angle between two vector fields. Conformal curvature tensor on a Riemann manifold is a curvature tensor of the $(1, 3)$ – type that is invariant under conformal transformations. This tensor gives important information about the Riemann geometry of the manifold. If it vanishes then the manifold is said to be conformally flat, i.e the manifold is flat under conformal transformations. A concircular transformation is a special conformal transformation and, preserves the geodesic circle. These type of transformations and their applications to differential geometry were studied by Yano [10]. In same paper Yano defined concircular curvature tensor and showed that this tensor is invariant under concircular transformations. A Riemannian manifold is called concircularly flat if this tensor vanishes. Yano and Sawaski [11] introduced quasi-conformal curvature tensor which includes both concircular and conformal curvature tensor as special cases. If this tensor vanishes on the manifold identically then the manifold is called quasi-conformally flat. Flatness conditions of conformal, concircular and quasi-conformal curvature tensors on contact manifolds has many geometric and physical applications. For example, while a conformal flat Sasakian manifold is of constant curvature [12], a normal complex contact metric manifold is not conformal, concircular and quasi-conformal flat [13]. On the other hand, a conformally flat NMCP manifold is a generalized quasi-Einstein manifold [6]. A type of curvature tensor were defined in [14] with the name of generalized quasi-conformal curvature (GQC) tensor. This tensor contains the concircular, conformal, quasi-conformal, conharmonic, projective and m-projective curvature tensors for the special values of coefficients. GQC curvature tensor on NMCP manifolds has been studied by Ünal [9].

In this chapter, we present a review on the normal contact pair manifolds under certain conditions on curvature tensors. Firstly, we give some fundamental facts on the contact pair manifolds and curvature tensors. Later, we present many results on NMCP manifolds under some flatness conditions of these curvature tensors. Finally, we examine some symmetry properties of normal contact metric pair manifolds with curvature tensors.

2. A REVIEW ON CONTACT PAIR MANIFOLDS

A contact manifold is a $(2k + 1)$ – dimensional differentiable manifold with a contact 1-form η which satisfies $\eta \wedge (d\eta)^k \neq 0$ [2]. In 1960s this type of manifolds was studied with tensorial approach. For this aim, the almost contact structure were given as similar to almost complex structures. After that, more researcher took their attention to this subject

and the contact geometry have been developed dramatically. An almost contact structure is defined as follow;

2.1. Definition

Let M be a $(2k+1)$ - dimensional differentiable manifold and ϕ be a $(1,1)$ -tensor field on M . If we have ,

$$\phi^2 = -I + \eta \otimes \xi, \eta(\xi) = 1, \phi\xi = 0$$

for a vector field ξ on M , then (ϕ, η, ξ) is called almost contact structure (M, ϕ, η, ξ) is called as an almost contact structure [2].

An almost complex manifold is a complex manifold if the Nijenhuis tensor of almost complex structure J is zero, that means J is integrable. We have a complex structure J on the product manifold $M \times \square$. Similarly if J is integrable then (M, ϕ, η, ξ) is called normal contact manifold or Sasaki manifold. Also there are many sub classes of almost contact manifolds which are normal or not. We refer to reader [2] for more details on the contact geometry.

The another type of contact manifolds is complex contact manifolds. The Riemannian geometry of complex contact manifolds have been studied since 1970s. Although, a complex manifold seem to be similar to complexified of a real contact manifold; unfortunately all complex contact manifolds are not complexified a real contact structure. So, a complex contact manifold have many different properties. Complex almost contact structure on complex manifolds is defined as follow;

2.2. Definition

A complex almost contact metric manifold is a complex odd $(2k+1)$ - dimensional complex manifold with $(J, \phi, \phi \circ J, \xi, -J \circ \xi, \eta, \eta \circ J, g)$ structure such that

$$\phi^2 = (\phi \circ J)^2 = -I + \eta \otimes \xi - (\eta \circ J) \otimes (J \circ \xi)$$

$$\eta(\xi) = 1, \eta(-J \circ \xi) = 0, (\eta \circ J)(-J \circ \xi) = 1, (\eta \circ J)(\xi) = 0$$

$$g(\phi Y_1, Y_2) = -g(Y_1, \phi Y_2), g((\phi \circ J)Y_1, Y_2) = -g(Y_1, (\phi \circ J)Y_2)$$

where g is a Hermitian metric on M , J is a natural almost complex structure [15].

The normality of complex almost contact metric manifolds were given by Ishihara-Konishi [15] and Korkmaz [16] . Normal complex contact metric manifolds were studied by several authors [13,16,17].

Blair et al. [8] worked on Calabi-Eckman manifold similar to complex manifolds. They gave a new kind of manifolds with structure, which was called by bicontact manifolds. Contact pair manifolds have some different properties from contact and complex contact manifolds. A contact pair manifold is defined as follow:

2.3. Definition

Let M be a k -dimensional differentiable manifold such that $k = 2m + 2n + 2$ for m, n integers. Two 1-forms ω_1, ω_2 on M is called contact pair of type (m, n) if we have

$$\omega_1 \wedge (d\omega_1)^m \wedge \omega_2 \wedge (d\omega_2)^n \neq 0,$$

$$(d\omega_1)^{m+1} = 0, (d\omega_2)^{n+1} = 0.$$

$(M, (\omega_1, \omega_2))$ is called as a contact pair manifold [4].

We have two distributions D_1 and D_2 which are the kernels of ω_1 and ω_2 , respectively. Also, two characteristic foliations of M are given by $F_1 = D_1 \cap \ker d\omega_1$ and $F_2 = D_2 \cap \ker d\omega_2$. Moreover, F_1 and F_2 has contact forms which are induced from ω_2, ω_1 , respectively. The characteristic vector fields Z_1 and Z_2 of a contact pair manifold are given by

$$\omega_1(Z_1) = \omega_2(Z_2) = 1, \omega_1(Z_2) = \omega_2(Z_1) = 0.$$

Also, two subbundles TG_1 and TG_2 are defined as $TG_i = \ker d\omega_i \cap \ker \omega_1 \cap \ker \omega_2$, for $i = 1, 2$. Thus, we have

$$TF_i = TG_i \oplus \square Z_j, 1 \leq i, j \leq 2, i \neq j.$$

The tangent bundle of $(M, (\omega_1, \omega_2))$ can be decomposable by different ways. We can write $TF_1 = TG_1 \oplus \square Z_2$ and $TF_2 = TG_2 \oplus \square Z_1$. Therefore we get $TM = TG_1 \oplus TG_2 \oplus \square Z_1 \oplus \square Z_2$. Also we can state $TM = H \oplus V$ for $H = TG_1 \oplus TG_2$ and $V = \square Z_1 \oplus \square Z_2$, we call H is horizontal subbundle and V is vertical subbundle of TM .

Let Y be an arbitrary vector field on M . We can write $Y = Y^H + Y^V$, where Y^H, Y^V horizontal and vertical component of Y , respectively. On the other hand, for $Y^1 \in TF_1$ and $Y^2 \in TF_2$, we have $Y = Y^1 + Y^2$. Also we can write $Y^1 = Y^{1^h} + \omega_2(Y^1)Z_2$ and $Y^2 = Y^{2^h} + \omega_1(Y^2)Z_1$, where Y^{1^h} and Y^{2^h} are horizontal parts of Y^1, Y^2 respectively. Thus we have $Y^H = Y^{1^h} + Y^{2^h}$, $Y^V = \omega_1(Y^2)Z_1 + \omega_2(Y^1)Z_2$. From all these decompositions of X finally we get

$$Y = Y^{1^h} + Y^{2^h} + \omega_1(Y^2)Z_1 + \omega_2(Y^1)Z_2,$$

$$\omega_1(Y^{1^h}) = \omega_1(Y^{2^h}) = 0, \quad \omega_2(Y^{1^h}) = \omega_2(Y^{2^h}) = 0.$$

Almost contact metric structure on contact pair manifolds is given as follow:

2.4. Definition

A $(k = 2m + 2n + 2)$ -dimensional differentiable manifold M is called a metric almost contact pair manifold such that

$$\phi^2 = -I + \omega_1 \otimes Z_1 + \omega_2 \otimes Z_2, \quad \phi Z_1 = \phi Z_2 = 0. \quad (1.1)$$

$$g(\phi Y_1, \phi Y_2) = g(Y_1, Y_2) - \omega_1(Y_1)\omega_1(Y_2) - \omega_2(Y_1)\omega_2(Y_2)$$

where ϕ is $(1,1)$ -tensor field on M [18].

As mentioned above we have two induced contact forms on the foliations F_1 and F_2 . For to define almost contact structures on F_1 and F_2 we need the decomposability of ϕ , i.e $\phi = \phi_1 + \phi_2$. If $\phi TF_i \subset TF_i$ for $1 \leq i \leq 2$, then ϕ is said to be decomposable. Thus, we have an almost contact structure (α_1, Z_1, ϕ_1) (*resp.* (α_2, Z_2, ϕ_2)) on TF_2 (*resp.* TF_1) if ϕ is decomposable. Throughout the paper we assume that ϕ is decomposable. Moreover, we have

$$g(Y_i, Z_i) = \alpha_i(Y_i), \quad g(Z_i, Z_j) = \delta_{ij}, \quad g(Z, Z) = 2$$

$$\nabla_{Z_i}^{Z_j} = 0, \quad \nabla_{Z_i}^{\phi} = 0, \quad \nabla_{Y_1}^{Z_1} = -\phi_1 Y_1, \quad \nabla_{Y_1}^{Z_2} = -\phi_2 Y_1$$

where $\phi = \phi_1 + \phi_2$ and $Z = Z_1 + Z_2$.

Following definition determine us the kind of Riemannian metric on a metric almost contact pair manifold.

2.5. Definition

Let $(M, \phi, Z_1, Z_2, \omega_1, \omega_2, g)$ be a metric almost contact pair manifold. The Riemannian metric g is called [3]

- compatible if $g(\phi Y_1, \phi Y_2) = g(Y_1, Y_2) - \omega_1(Y_1)\omega_1(Y_2) - \omega_2(Y_1)\omega_2(Y_2)$ for all $Y_1, Y_2 \in \Gamma(TM)$.
- associated if $g(Y_1, \phi Y_2) = (d\omega_1 + d\omega_2)(Y_1, Y_2)$ and $g(Y_1, Z_i) = \omega_i(Y_1)$, for $i = 1, 2$ and for all $Y_1, Y_2 \in \Gamma(TM)$.

The normality of a metric almost contact manifold M has been given in [18]. The authors defined two almost complex structures on M as,

$$J = \phi - \omega_2 \otimes Z_1 + \omega_1 \otimes Z_2, \quad T = \phi + \omega_2 \otimes Z_1 - \omega_1 \otimes Z_2.$$

M is said to be normal if J and T are integrable. With following theorem we have covariant derivation of ϕ as similar to almost contact manifolds.

2.6. Theorem

Let $(M, \phi, Z_1, Z_2, \omega_1, \omega_2, g)$ be a normal metric contact pair manifold then we have

$$g((\nabla_{Y_1} \phi)Y_2, Y_3) = \sum_{i=1}^2 (d\omega_i(\phi Y_2, Y_1)\omega_i(Y_3) - d\omega_i(\phi Y_3, Y_1)\omega_i(Y_2)),$$

where Y_1, Y_2, Y_3 are arbitrary vector fields on M [5].

Curvature properties of NMCP manifolds were studied in [19,20]. We use the following statements for the Riemann curvature;

$$R(Y_1, Y_2)Y_3 = \nabla_{Y_1} \nabla_{Y_2} Y_3 - \nabla_{Y_2} \nabla_{Y_1} Y_3 - \nabla_{[Y_1, Y_2]} Y_3,$$

$$R(Y_1, Y_2, Y_3, Y_4) = g(R(Y_1, Y_2)Y_3, Y_4)$$

for all $Y_1, Y_2, Y_3, Y_4 \in \Gamma(TM)$. Also the Ricci operator is defined by

$$QY = \sum_{i=1}^{\dim(M)} R(Y, E_i)E_i,$$

and the Ricci curvature and scalar curvature are given by

$$Ric(Y_1, Y_2) = g(QY_1, Y_2) \text{ and } scal = \sum_{i=1}^{dim(M)} Ric(E_i, E_i)$$

where $E_i, 1 \leq i \leq dim(M)$ are orthonormal basis of M .

On the other hand, we have following relations [19,20];

$$R(Y_1, Z, Z, Y_3) = d\omega_1(\phi Y_3, Y_1)\omega_1(Y_2) + d\omega_2(\phi Y_3, Y_1)\omega_2(Y_2) \\ - d\omega_1(\phi Y_3, Y_1)\omega_1(Y_2) - d\omega_2(\phi Y_3, Y_2)\omega_2(Y_1)$$

and for $Y_4, Y_5 \in \Gamma(H)$ we get

$$R(Y_4, Z, Z, Y_5) = -g(Y_4, Y_5) \\ R(Z, Y_4)Y_5 = d\omega_1(\phi Y_5, Y_4)Z_1 + d\omega_2(\phi Y_5, Y_4)Z_2, \\ R(Y_1, Z)Z = -\phi^2 Y_1.$$

Let take an orthonormal basis of M as follow:

$$\{E_1, E_2, \dots, E_p, \phi E_1, \phi E_2, \dots, \phi E_m, E_{m+1}, E_{m+2}, \dots, E_{m+n}, \\ \phi E_{m+1}, \phi E_{m+2}, \dots, \phi E_n, Z_1, Z_2\}$$

then for all $Y_1 \in \Gamma(TM)$ we get the Ricci curvature of M as

$$Ric(Y_1, Z) = \sum_{i=1}^{2m+2n} [d\omega_1(\phi E_i, E_i)\omega_1(Y_1) + d\omega_2(\phi E_i, E_i)\omega_2(Y_1)].$$

So, we obtain the following results [20]:

$$Ric(Y_1, Z) = 0, \text{ for } Y_1 \in \Gamma(H), \\ Ric(Z, Z) = 2m + 2n, Ric(Z_1, Z_1) = 2m, \\ Ric(Z_2, Z_2) = 2n, Ric(Z_1, Z_2) = 0.$$

A generalized quasi-Einstein (GQE) manifold is a generalization of quasi-Einstein manifolds [21]. These type of manifolds were defined by Chaki [22] and De and Ghosh [23]. In this study we follow the definition of De and Ghosh. Also, GQE manifolds have arisen in the solutions of Einstein fields equations in general relativity. Unal [6] studied on the NMCP manifolds which are GQE manifolds.

2.7. Definition

A $k = (2m + 2n + 2)$ -dimensional NMCP manifold M is said to be a generalized quasi-Einstein manifold if its Ricci tensor is not identically zero and satisfies;

$$\begin{aligned} \text{Ric}(Y_1, Y_2) &= \lambda g(Y_1, Y_2) + (2m - \lambda)\omega_1(Y_1)\omega_1(Y_2) \\ &\quad + (2n - \lambda)\omega_2(Y_1)\omega_2(Y_2) \end{aligned}$$

for all vector fields $Y_1, Y_2 \in \Gamma(TM)$ and λ is non-zero scalar [6].

By the following lemma we can determine a NMCP GQE manifold via decomposition of vector fields.

2.8. Lemma

A NMCP is a GQE manifold if and only if we have $\text{Ric}(Y_1, Y_2) = \lambda g(Y_1, Y_2)$ for all $Y_1, Y_2 \in \Gamma(H)$ [6].

With the following theorem we state the existence of NMCP GQE manifolds.

2.9. Theorem

Let M be a k -dimensional NMCP manifold with scalar curvature $scal \neq k - 2$. If we have the relation

$$\begin{aligned} &\text{Ric}(Y_2, Y_3)\text{Ric}(Y_1, Y_4) \\ &- \text{Ric}(Y_1, Y_3)\text{Ric}(Y_2, Y_4) = \frac{1}{2}(scal - k + 2)[g(Y_2, Y_3)g(Y_1, Y_4) \\ &\quad - g(Y_1, Y_3)g(Y_2, Y_4)] \end{aligned}$$

M for all $Y_1, Y_2, Y_3, Y_4 \in \Gamma(TM)$, then M is a GQE manifold [6].

Let π be a plane section in $T_Q M$ for any $Q \in M$. The sectional curvature of π is given as $\text{Sec}(\pi) = \text{Sec}(u \wedge v)$, where u, v orthonormal vector fields. For any $(p + q)$ -dimensional subspace $L \subset T_Q M$, $2 \leq m + n \leq k$, its scalar curvature $scal(L)$ is denoted by

$$scal(L) = \sum_{1 \leq i, j \leq m+n} \text{Sec}(E_i \wedge E_j)$$

where E_1, \dots, E_k is any orthonormal basis of L []. When $L = T_Q M$, the scalar curvature is just the scalar curvature $scal(Q)$ of M at $Q \in M$.

By following theorem we present the characterization of NMCP GQE manifolds.

2.10. Theorem

An $(k = 2m + 2n + 2)$ -dimensional NMCP is a GQE manifold if and only if there exist a function μ on M satisfying

$$\text{scal}(P) + m + n - \mu = \sec(P^\perp), \quad Z_1, Z_2 \in T_Q P^\perp$$

$$\text{scal}(N) + m + n = \sec(N^\perp), \quad Z_1, Z_2 \in T_Q N^\perp$$

$$\text{scal}(R) + n - m = \sec(R^\perp), \quad Z_1 \in T_Q R, Z_2 \in T_Q R^\perp$$

where $(m + n + 1)$ -plane sections P, R and $(m + n)$ -plane section N ; P^\perp, N^\perp and R^\perp denote the orthogonal complements of P, N and R in $T_Q M$, respectively [6].

De and Ghosh defined the notion of generalized quasi-constant curvature for a Riemannian manifold.

2.11. Definition

A NMCP manifold M is called a space of generalized quasi-constant curvature if we have

$$\begin{aligned} R(Y_1, Y_2, Y_3, Y_4) = & A[g(Y_2, Y_3)g(Y_1, Y_4) - g(Y_1, Y_3)g(Y_2, Y_4)] \\ & + B[g(Y_1, Y_4)\eta_1(Y_2)\eta_1(Y_3) - g(Y_1, Y_3)\eta_1(Y_2)\eta_1(Y_4) \\ & + g(Y_2, Y_3)\eta_1(Y_1)\eta_1(Y_4) - g(Y_2, Y_4)\eta_1(Y_1)\eta_1(Y_3)] \\ & + C[g(Y_1, Y_4)\eta_2(Y_2)\eta_2(Y_3) - g(Y_1, Y_3)\eta_2(Y_2)\eta_2(Y_4) \\ & + g(X_2, X_3)\eta_2(X_1)\eta_2(X_4) - g(Y_2, Y_4)\eta_2(Y_1)\eta_2(Y_3)] \end{aligned}$$

for all $Y_1, Y_2, Y_3, Y_4 \in \Gamma(TM)$, where A, B, C are constant [23].

Presented author [6] examined NMCP manifolds are space of generalized quasi-constant curvature and he proved that such manifolds are generalized quasi-Einstein manifolds.

3. FLATNESS OF CURVATURE TENSORS ON NMCP MANIFOLDS

Let V be a vector space, g be positive defined metric on V and let define a map T by:

$$T : V \times V \rightarrow Hom(V, V)$$

$$(Y_1, Y_2) \rightarrow T(Y_1, Y_2)$$

If T has following properties then it is said to be a curvature tensor:

1. $T(Y_1, Y_2) = -T(Y_2, Y_1)$
2. $g(T(Y_1, Y_2)Y_3, Y_4) = -g(T(Y_1, Y_2)Y_4, Y_3)$
3. $T(Y_1, Y_2)Y_3 + T(Y_2, Y_3)Y_1 + T(Y_3, Y_1)Y_2 = 0$

for all $Y_1, Y_2, Y_3 \in V$. If V is the tangent space of a manifold then we can define any curvature tensor on this manifold. One of canonical example of curvature tensors is well known Riemannian curvature tensor.

A Euclidean space is a manifold with zero Riemannian curvature tensor. This mean that the Euclidean space is flat. Flatness is measured with the being zero of the Riemannian curvature tensor of a Riemannian manifold. If a Riemannian manifold is flat it is understood that the manifold is locally Euclidean. Therefore, the flatness is an important notion for the classification of Riemannian manifolds. Some special maps can transform a Riemannian manifold to a Euclidean space. One of them is conformal maps. If a Riemannian manifold could be transformed to a Euclidean space with conformal maps then we recall this manifold by conformally flat. A conformal map has a curvature invariant which is called a conformal curvature tensor. Thus, we determine the conformally flatness with this tensor. Conformal curvature tensor on a $k = (2m + 2n + 2)$ - dimensional NMCP manifold is defined as follow:

$$\begin{aligned} C(Y_1, Y_2)Y_3 = & R(Y_1, Y_2)Y_3 + \frac{scal}{(2m + 2n + 1)(2m + 2n)} (g(Y_2, Y_3)Y_1 \\ & - g(Y_1, Y_3)Y_2) + \frac{1}{2m + 2n} (g(Y_1, Y_3)QY_2 - g(Y_2, Y_3)QY_1 \\ & + Ric(Y_1, Y_3)Y_2 - Ric(Y_2, Y_3)Y_1) \end{aligned}$$

for $Y_1, Y_2, Y_3 \in \Gamma(M)$.

A geodesic circle is defined as a curve whose first curvature is constant and second curvature is identically zero. A geodesic circle is not in general transformed into a geodesic circle by conformal transformations. For to solve this issue Yano defined a new transformation which is called a concircular transformation. Similar to conformal curvature tensor concircular curvature tensor is invariant under concircular transformations. Also a Riemannian manifold is called concircularly flat if this tensor

vanishes. Concircular curvature tensor on a NMCP manifold is defined as follow:

$$L(Y_1, Y_2)Y_3 = R(Y_1, Y_2)Y_3 - \frac{scal}{(2m+2n+2)(2m+2n+1)} [g(Y_2, Y_3)Y_1 - g(Y_1, Y_3)Y_2]$$

for $Y_1, Y_2, Y_3 \in \Gamma(M)$.

The quasi-conformal curvature was defined by Yano and Sawaski [11] included both concircular and conformal curvature as special cases:

$$\begin{aligned} C(Y_1, Y_2)Y_3 &= aR(Y_1, Y_2)Y_3 + b[Ric(Y_2, Y_3)Y_1 - Ric(Y_1, Y_3)Y_2 \\ &\quad + g(Y_2, Y_3)QY_1 - g(Y_1, Y_3)QY_2] \\ &\quad - \frac{scal}{2m+2n+2} \left[\frac{a}{2m+2n+1} + 2b \right] [g(Y_2, Y_3)Y_1 - g(Y_1, Y_3)Y_2] \end{aligned}$$

for $Y_1, Y_2, Y_3 \in \Gamma(M)$.

Conharmonic transformations are a special type of conformal transformations. They preserve the harmonicity property of smooth functions. A conharmonic curvature tensor is known as the complex version of conformal curvature tensor and it is invariant under conharmonic transformations. Conharmonic curvature tensor on a NMCP manifold M is defined as follow:

$$\begin{aligned} K(Y_1, Y_2)Y_3 &= R(Y_1, Y_2)Y_3 - \frac{1}{4k} [Ric(Y_2, Y_3)Y_1 - Ric(Y_1, Y_3)Y_2 \\ &\quad + g(Y_2, Y_3)QY_1 - g(Y_1, Y_3)QY_2] \end{aligned}$$

for $Y_1, Y_2, Y_3 \in \Gamma(M)$. If $K = 0$, then M is called conharmocially flat NMCP manifold.

Projective curvature tensor on a k -dimensional NMCP manifold is given by

$$P(Y_1, Y_2)Y_3 = R(Y_1, Y_2)Y_3 - \frac{1}{k+2} [Ric(Y_2, Y_3)Y_1 - Ric(Y_1, Y_3)Y_2]$$

for $Y_1, Y_2, Y_3 \in \Gamma(M)$. If $P = 0$, then M is called projectively flat NMCP manifold.

M -projective curvature tensor is on a k -dimensional NMCP manifold is defined as

$$M(Y_1, Y_2)Y_3 = R(Y_1, Y_2)Y_3 - \frac{1}{2(k-1)}[Ric(Y_2, Y_3)Y_1 - Ric(Y_1, Y_3)Y_2 + g(Y_2, Y_3)QY_1 - g(Y_1, Y_3)QY_2]$$

for $Y_1, Y_2, Y_3 \in \Gamma(M)$. If $M = 0$, then M is called M - projectively flat NMCP manifold.

The another special curvature tensor were defined in [14] with the name of generalized quasi-conformal curvature tensor (GQC). A GQC curvature tensor W is defined on a k -dimensional NMCP manifold as following;

$$W(Y_1, Y_2)Y_3 = R(Y_1, Y_2)Y_3 + \alpha[Ric(Y_2, Y_3)Y_1 - Ric(Y_1, Y_3)Y_2] + \beta[g(Y_2, Y_3)QY_1 - g(Y_1, Y_3)QY_2] - \frac{\gamma scal}{2k+1} \left(\frac{1}{2k} + \alpha + \beta \right) [g(Y_2, Y_3)Y_1 - g(Y_1, Y_3)Y_2]$$

for all $Y_1, Y_2, Y_3 \in \Gamma(TM)$. For the special values of α, β, γ we have same special curvature tensors;

Curvature Tensor			
0	0	0	Riemann (R)
$-\frac{1}{2k-1}$	$-\frac{1}{2k-1}$	1	Conformal (C)
$-\frac{1}{2k-1}$	$-\frac{1}{2k-1}$	0	Conharmonic (K)
0	0	1	Concircular (C)
$-\frac{1}{2k}$	0	0	Projective (P)
$-\frac{1}{4k}$	$-\frac{1}{4k}$	0	m-Projective (M)

Table 1. Some curvature tensors derived from GQC curvature tensor

The flatness of GQC curvature tensor also determines the flatness of special curvature tensors mentioned above table. Blair, Bande and Hadjar [7] studied on conformal flatness of NMCP manifolds and they proved following theorem.

3.1. Theorem

A conformally flat NMCP manifold is locally isometric to the Hopf manifold $S^{2q+1}(1) \times S^1$ [24].

In 2020, presented author obtained following results for the flatness of conformal, concircular and quasi-conformal curvature tensors.

3.2. Theorem

A conformal flat NMCP manifold is an Einstein manifold with positive scalar curvature and has positive sectional curvature [7].

3.3. Theorem

A concircular flat normal contact pair manifold is Einstein manifold [7].

3.4. Theorem

A quasi-conformally flat NMCP manifold is an Einstein manifold with a positive scalar curvature and is a space of constant curvature [7].

A NMCP manifold M is called by GQC-flat if $W(Y_1, Y_2)Y_3 = 0$ and also, M is said to be GQC-Z-flat if $W(Y_1, Z)Y_2 = 0$ for all Y_1, Y_2, Y_3 vector fields on M . Some results on the flatness conditions of generalized quasi-conformal curvature tensor were obtained in [8] by Ünal.

3.5. Theorem

A GQC-Z-flat and GQC-flat NMCP manifold is GQE manifold [8].

With the following theorem as we see that a NMCP manifold could an example of space forms.

3.6. Theorem

Let M be an Einstein NMCP manifold. If M is also GQC-flat, then M is a generalized real space form [8].

By the following result we have an example of space of generalized quasi-constant curvature.

3.7. Theorem

Let M be a GQE NMCP manifold. If M is GQC-flat then it is a space of generalized quasi-constant curvature [8].

The sectional curvature of a Riemannian manifold give us significant geometric interpretation. In contact geometry, we have ϕ -

sectional curvature and ξ -sectional curvature. Similarly, we have ϕ -sectional curvature and Z -sectional curvature for NMCP manifolds.

3.8. Theorem

The sectional curvature of a GQC-flat NMCP manifold is given by

$$\begin{aligned} \text{sec}(X, Y) = & -\frac{\alpha + \beta}{1 - \alpha + \beta(k - 2)} \left(-\alpha(\text{scal} - (k - 2)) \right. \\ & \left. + \beta + \gamma \frac{\text{scal}}{2k + 1} \left(\frac{1}{2k} + \alpha + \beta \right) (k - 3) \right) + \gamma \frac{\text{scal}}{2k + 1} \left(\frac{1}{2k} + \alpha + \beta \right) \end{aligned}$$

for unit and mutually orthogonal horizontal vector fields X, Y [9].

3.9. Theorem

Let M be a GQC-flat NMCP manifold. If the scalar curvature is constant, then M has constant sectional curvature [8].

3.10. Theorem

A NMCP manifold is \mathbf{M} -projectively flat if and only if it is of generalized quasi-constant curvature [6].

3.11. Theorem

Let M be \mathbf{M} -projectively flat NMCP manifold. If M is also concircularly flat then it is locally isometric to Hopf manifold $S^{2q+1}(1) \times S^1$ [6].

4. SEMI-SYMMETRY CONDITIONS ON NMCP MANIFOLDS

For a $(1, 3)$ -type curvature tensor T , $R(Y_1, Y_2).T$ is defined by

$$R(Y_1, Y_2).T = \nabla_{Y_1} \nabla_{Y_2} T - \nabla_{Y_2} \nabla_{Y_1} T - \nabla_{[Y_1, Y_2]} T.$$

The operation of " \cdot " acts like as a derivation on curvature tensor and it is defined as follow ;

$$\begin{aligned} (R(Y_1, Y_2).T)(Y_3, Y_4)Y_5 = & R(Y_1, Y_2)T(Y_3, Y_4)Y_5 - T(R(Y_1, Y_2)Y_3, Y_4)Y_5 \\ & - T(Y_3, R(Y_1, Y_2)Y_4)Y_5 - T(Y_3, Y_4)R(Y_1, Y_2)Y_5. \end{aligned}$$

On the other hand for $(0, 2)$ -type tensor field S on M , we have

$$(T(Y_1, Y_2) \cdot S)(Y_3, Y_4) = S(T(Y_1, Y_2)Y_3, Y_4) - S(Y_3, T(Y_1, Y_2)Y_4).$$

The notion of locally symmetry has the important position to study the Riemannian geometry of manifolds. A Riemannian manifold is locally symmetric if $\nabla R = 0$. This type of Riemannian manifolds are a generalization of manifolds of constant curvature. As a generalization of locally symmetry we have semi-symmetric Riemann manifolds. A Riemannian manifold is called semi-symmetric if $R \cdot R = 0$. We also generalized the concept of semi-symmetry as follow; if $R \cdot T = 0$ then the manifold is called T – semi symmetric.

Similar to locally symmetric manifold, A Riemann manifold is called as locally Ricci symmetric if $\nabla Ric = 0$. Also, if $R \cdot Ric = 0$ then the manifold is called Ricci-semi-symmetric. As a generalization of this notion we have T – Ricci-semi-symmetric i.e $T \cdot Ric = 0$.

Locally symmetric NMCP manifolds were studied in [24]. The authors proved following theorem:

4.1. Theorem

Let M be a complete, locally symmetric, normal, metric contact pair. Then either the universal covering space of M is a Calabi-Eckmann manifold, $S^{2m+1}(1) \times S^{2n+1}(1)$, and M is compact, or the universal covering space of M is $S^{2m+1}(1) \times \square$ [24].

Presented author studied on some semi-symmetry conditions with related to concircular curvature tensor and obtained following results:

4.2. Theorem

A Ricci semi-symmetric NMCP manifold is a generalized quasi-Einstein manifold [9].

4.3. Theorem

A concircular Ricci-semi symmetric NMCP manifold is a generalized quasi-Einstein manifold [9].

4.4. Theorem

Let M be an NMCP manifold satisfying $L(Y_1, Z) \cdot R = 0$ for any $Y_1 \in \Gamma(TM)$. Then, the scalar curvature of M is $scal = (2m + 2n + 2)(2m + 2n + 1)$ or the sectional curvature of M is 1 [9].

4.5. Theorem

A normal metric contact pair manifold satisfying $R(Y_1, Z) \cdot L = 0$ for any $Y_1 \in \Gamma(TM)$, is a space of constant curvature [9].

4.6. Theorem

Let M be an NMCP manifold satisfying $R(Y_1, Z).L = 0$ for any $Y_1 \in \Gamma(TM)$. Then, M is a generalized quasi-Einstein manifold [9].

4.7. Theorem

An NMCP manifold M satisfying $L(Y_1, Z).L = 0$ for any $Y_1 \in \Gamma(TM)$, is a space of constant curvature or the scalar curvature is $scal = (2m + 2n + 2)(2m + 2n + 1)$ [9].

4.8. Theorem

Let M be NMCP manifold satisfying $L(Y_1, Z).L = 0$, for any $Y_1 \in \Gamma(TM)$. Then, M is a generalized quasi-Einstein manifold [9].

4.9. Theorem

A NMCP manifold is M –projectively semi-symmetric if and only if M is a generalized quasi-Einstein manifold [6].

4.10. Theorem

A NMCP manifold satisfies $W \cdot Ric = 0$ if and only if M is a generalized quasi-Einstein manifold [6].

5. CONCLUSIONS

Contact geometry, which is an important area of differential geometry, has a major role in theoretical physics as well as its applications in differential geometry. For this reason, both differential geometries and theoretical physicists have been working on the contact geometry. Except for theoretical physics, there are many applications of the contact geometry to medical science, technology, geometric optics, geometric quantization, control theory, thermodynamics, and classical mechanics. The developments of contact geometry applications and the strengthening of the theoretical background depend on the work to be done in the field of differential geometry. In this context, studies on the Riemannian geometry of contact manifolds are very important. On the other hand, solutions of the Einstein fields equations are a major notion in the relativity theory. Einstein manifolds which are arisen from Einstein fields equations, quasi-Einstein manifolds which are also the solution of Einstein fields equations and generalized quasi-Einstein manifolds which are the generalization of Einstein and quasi-Einstein manifolds are significant type of manifolds in the Riemannian geometry. For example, η –Einstein manifolds are a special kind of quasi-Einstein manifolds that come from contact geometry. Also complex η –Einstein manifolds [17] are another kind of GQE

manifolds. With the NMCP manifolds, we obtain another kind of generalized quasi-Einstein manifolds. Thus, we see that this type of manifolds has many applications in the general relativity. All these results show that contact pair manifolds are an important study subject. Thanks to the important benefits obtained by curvature tensors on the differential geometry of manifolds, we have revealed some important properties of this type of manifolds. By bringing together the results of curvature tensors on NMCP manifolds, with this book chapter we have created a resource for important future work. The geometry of contact pairs, where there are many more open problems, awaits the interest of researchers working in the field of contact geometry.

REFERENCES

1. Kholodenko, A. L. 2013. Applications of contact geometry and topology in physics. *World Scientific*.
2. Blair, D. E., 2010. Riemannian geometry of contact and symplectic manifolds, V.203 ,2nd Edition, *Progress in Mathematics, Springer Science Business Media*
3. Blair, D. E., Ludden G. D., and Yano, K. 1974. Geometry of complex manifolds similar to the Calabi-Eckmann manifolds, *Journal of Differential Geometry*, 9(2), 263-274.
4. Bande, G. and Hadjar, A. 2005. Contact pairs , *Tohoku Mathematical Journal, Second Series*, 57(2), 247-260.
5. Bande, G. and Hadjar, A. 2010. On normal contact pairs *International Journal of Mathematics*, 21(06), 737-754.
6. Ünal, İ. 2020. Generalized Quasi-Einstein Manifolds in Contact Geometry. *Mathematics*, 8(9), 1592.
7. Ünal, İ., 2020. Some flatness conditions on normal metric contact Pairs *Communications Faculty of Sciences University of Ankara Series A1 Mathematics and Statistics*. 69(2): 262-271.
8. Ünal, İ., 2020. Generalized Quasi-Conformal Curvature Tensor On Normal Metric Contact Pairs, *International Journal of Pure and Applied Sciences* , accepted.
9. Ünal, İ., 2021. On Metric Contact Pairs with Certain Semi-Symmetry Conditions. *Politeknik Dergisi* , 1-1 DOI: 10.2339/politeknik.769662
10. Yano, K., 1940. Conircular geometry I. Conircular transformations. *Proceedings of the Imperial Academy*, 16(6), 195-200.
11. Yano, K. and Sawaski, S., 1968. Riemannian manifolds admitting a conformal transformation group, *J. Differential Geom.* 2 , 161–184.
12. De, U. C. and Shaikh, A.A., 2009. Complex Manifolds and Contact Manifolds, 1st Edition, *Narosa Publishing House Pvt. Ltd.*, New Delhi, 320 pages.
13. Turgut Vanlı, A., and Ünal, İ., 2017. Conformal, concircular, quasi-conformal and conharmonic flatness on normal complex contact metric manifolds. *International Journal of Geometric Methods in Modern Physics*, 14(05), 1750067.
14. Baishya, K. K. and Chowdhury P.R., 2016. On generalized quasi-conformal $N(\kappa, \mu)$ -manifolds. *Communications of the Korean Mathematical Society* , 31.1 163-176.
15. Ishihara, S. and Konishi, M., 1982. Complex almost contact structures in a complex contact manifold, *Kodai Math. J.* 5 , 30–37.

16. Korkmaz , B., 2000. Normality of complex contact manifolds, *Rocky Mountain Journal of Mathematics*, 30 , 1343–1380.
17. Turgut Vanlı, A. and Ünal, İ., 2017. On complex η -Einstein normal complex contact metric manifolds. *Communications in Mathematics and Applications*. 8, 301–313.
18. Bande, G. and Hadjar, A., 2009. Contact pair structures and associated metrics *In Differential Geometry* , pp. 266-275.
19. Bande, G., Blair, D. E. and Hadjar, A., 2013. On the curvature of metric contact pairs *Mediterranean journal of mathematics*, 10(2), 989-1009.
20. Bande, G., Blair, D. E. and Hadjar, A., 2015. Bochner and conformal flatness of normal metric contact pairs, *Annals of Global Analysis and Geometry*, 48(1), 47-56.
21. De, U.C.; Ghosh, G.C., 2004. On quasi Einstein manifolds. *Periodica Mathematica Hungarica* , 48, 223–231.
22. Chaki, M.C., 2001. On Generalized quasi-Einstein manifold. *Publicationes Mathematicae Debrecen*, 58, 638–691.
23. De, U. C. and Ghosh, G. C., 2004. On generalized quasi–Einstein manifolds, *Kyungpook Mathematical Journal* 44 , 607–615.
24. Bande, G., Blair, D.E. 2013. Symmetry in the geometry of metric contact pairs. *Mathematische Nachrichten* 286, 1701–1709

